

博士論文

Crystal Chemistry and Frustrated Magnetism
of Kagome Minerals

(カゴメ格子無機化合物の結晶化学とフラストレート磁性)

石川 孟
Hajime Ishikawa

Doctoral Thesis

Crystal Chemistry and Frustrated Magnetism
of Kagome Minerals

Hajime Ishikawa

Graduate School of Frontier Sciences
The University of Tokyo

Supervisor: Prof. Zenji Hiroi
March 2016

Contents

Preface	1
Chapter 1. Introduction	3
1.1 Magnetism of atom	3
1.2 Magnetic interaction and magnetic orders	4
1.3 Magnetic frustration.....	7
1.3.1 Geometrical frustration	8
1.3.2 Competing ferromagnetic and antiferromagnetic interactions.....	10
1.4 Crystal chemistry and magnetic interaction of copper oxides	13
1.4.1 CuO ₆ octahedron and magnetic interactions	13
1.4.2 Kagome lattice	16
1.4.3 J_1 - J_2 chain and J_1 - J_2 square lattice	20
1.5 Scope of the thesis	21
Chapter 2. Experiments.....	24
2.1 Synthesis	24
2.2 Powder XRD.....	24
2.3 Single crystal XRD	25
2.4 Magnetization	25
2.5 Heat capacity.....	26
2.6 Magnetocaloric effect	26
2.7 Elemental analysis	26
Chapter 3. Crystal structures and structural phase transitions of volborthite.....	28
3.1 Brief history and outline	28
3.2 Synthesis and elemental analysis	29
3.3 $C2/c$ structure at room temperature.....	30
3.4 $I2/a$ structure at intermediate temperatures.....	31
3.5 $P2_1/a$ structure at low temperatures below 155 K.....	34
3.6 Discussion.....	37
3.6.1 Jahn-Teller distortion of CuO ₆ octahedra and tilting of V ₂ O ₇ pillars.....	37
3.6.2 Relationship between room temperature $C2/c$ and $C2/m$ structures	39
3.6.3 Structural changes around H ₂ O molecules.....	41
3.7 Summary	43

Chapter 4. Physical properties and high-field magnetic phase transitions of volborthite	44
4.1 Brief history and outline	44
4.2 Basic physical properties at low magnetic fields	46
4.3 Magnetic field induced phase transitions	49
4.4 Discussion	53
4.4.1 Spin structure of the 1/3 plateau phase	53
4.4.2 Magnetic phases below the 1/3 plateau and coupled J_1 - J_2 chain model	55
4.4.3 Coupled trimer model proposed by theoretical studies	56
4.5 Summary	58
Chapter 5. Structural and magnetic properties of engelhauptite and their comparison with volborthite	59
5.1 Brief history and outline	59
5.2 Synthesis and elemental analysis	59
5.3 Structural analysis	60
5.4 Magnetic properties	63
5.5 Discussion	66
5.5.1 Absence of structural phase transition in engelhauptite	66
5.5.2 Spin models of engelhauptite and volborthite	67
5.5.3 Origin of large sample dependence in volborthite	69
5.6 Summary	70
Chapter 6. Topochemical pseudomorphosis and magnetic properties of vesignieite	72
6.1 Brief history and outline	72
6.2 Synthesis and elemental analysis	73
6.3 Structural analysis	73
6.4 Magnetic properties	77
6.5 Discussion	79
6.5.1 Magnetic structure and in-plane weak-ferromagnetic moment	79
6.5.2 Magnetization process	81
6.6 Summary	82
Chapter 7. AMoOPO_4Cl ($A = \text{K, Rb}$): new candidates of the $S = 1/2$ J_1 - J_2 square lattice	83
7.1 Brief history and outline	83
7.2 Synthesis	84

7.3 Structural analysis.....	85
7.4 Magnetic properties	88
7.5 Discussion.....	89
7.6 Summary.....	91
Overall summary.....	92
References.....	94
Publication List.....	99
Acknowledgement	100

Preface

Electrons in materials show various electronic phases such as metal, insulator, superconducting state, and magnetically ordered states. Magnetism is one of the fundamental research areas in the material science and is often related to the mechanism of superconductivity and metal-insulator transitions: for example, the mother compounds of the high-temperature cuprate superconductors are antiferromagnetic insulators. Moreover, when magnetic properties are combined to other physical properties like thermal and electric transport properties, useful functions are obtained. Therefore, understanding the magnetic properties of materials and searching for novel magnetic phases are important for both basic science and future applications.

In recent years, searching for exotic quantum phases in materials is a challenging task. Frustrated magnets, where conventional magnetic orders are suppressed owing to the magnetic frustration, have attracted much attention as a playground of realizing novel phases such as spin liquids and spin nematics. A key to realize novel phases is the geometry of atoms in the materials. For example, two-dimensional kagome lattice made of corner-sharing triangles is a representative lattice where novel magnetic phases are predicted.

Target materials of this thesis are inorganic materials; most of them are synthetic copper minerals. One of the advantages of inorganic materials is the rich variety in the lattice made of magnetic ions. The crystal structures of inorganic materials are often described by the polyhedra containing an ion at the center. There are enormous possibilities in the arrangement and the connectivity of polyhedra, which determine the types and the strength of the magnetic interactions between the spins on magnetic ions. This richness in the crystal structures enables the realization of various kinds of spin lattices with magnetic frustration and magnetic phases on them.

In search for novel magnetic phases, I have studied three copper minerals with distorted and regular kagome lattices: volborthite $\text{Cu}_3\text{V}_2\text{O}_7(\text{OH})_2 \cdot 2\text{H}_2\text{O}$, engelhauptite $\text{KCu}_3\text{V}_2\text{O}_7(\text{OH})_2\text{Cl}$, and vesignieite $\text{BaCu}_3\text{V}_2\text{O}_8(\text{OH})_2$, which are closely related to each other in the crystal structures. One problem in the experimental studies of frustrated magnets is the difficulty in obtaining high-quality single crystals with relatively large size, which are required for detailed magnetic characterizations. Another problem is the presence of the disorder in real materials: frustrated magnets are sensitive to small disorder and the true ground state can be masked or replaced by randomly frozen states such as spin glasses. I have successfully synthesized high-quality single crystals or powder samples, characterized their crystal structures, and investigated their magnetic properties in wide temperature and magnetic field ranges. Based on thus obtained data, I have developed the crystal chemistry of the

kagome minerals and clarified their unusual magnetic properties. In addition, some related frustrated magnets are studied.

March 2016 Hajime Ishikawa

Chapter 1. Introduction

In this chapter, theoretical and experimental studies of frustrated magnets are briefly summarized. The crystal chemistry of the copper minerals with magnetic frustration and related compounds are also summarized. Finally, the scope of this thesis is stated. I referred refs [1-3] for general things of magnetism.

1.1 Magnetism of atom

In quantum mechanics, the state of an electron in an atom is specified by four quantum numbers; principal quantum number n , azimuthal quantum number l ($l = 0, 1, \dots, n - 1$), magnetic quantum number m ($m = l, l - 1, \dots, -l + 1, -l$) and spin quantum number s ($s = 1/2$ and $-1/2$). The electron has the orbital angular momentum $\hbar l$, where l is the orbital angular momentum operator, and magnetic moment with the orbital motion. The z -component of the magnetic moment is $\mu = -m\mu_B$ ($\mu_B = 9.2740 \times 10^{-21}$ erg/G). In addition, the electron has spin angular momentum $\hbar s$ and spin magnetic moment $\mu_s = -g\mu_B s$, where s is the spin operator of which components are expressed by the Pauli matrix and $g = 2.0023$.

The d orbitals, where electrons show rich physical properties, have $l = 2$ and $m = 2, 1, 0, -1, -2$. When an atom has some d electrons, the electronic configuration is determined by the rules as follows: the lowest energy state has maximum total spin angular momentum S among the possible electronic configurations, and maximum total orbital angular momentum L for the S . The first rule indicates that the electrons occupy different orbitals to reduce coulomb repulsion and electrons in different orbitals experience ferromagnetic interaction between them. The ferromagnetic interaction, which is caused by the coulomb interaction and the quantum mechanical effect, is called direct exchange interaction. The second rule can be classically understood that the coulomb repulsion is reduced when the electrons rotate in the same direction around the atomic core.

The orbital and spin angular momenta are not independent due to the effect called spin-orbit coupling. The orbital motion of electron around the atomic nucleus can be alternatively considered as an orbital motion of atomic nucleus from the electron's side. The rotating atomic nucleus with electric charge generates the magnetic field on electron, which affect the energies of the electron depending on its spin magnetic moment. With the spin-orbit coupling, we have to consider the total angular momentum $J = L + S$. The quantum number of J takes $J = L + S, L + S - 1, \dots, |L - S|$. When the orbitals are less than and more than half-filled, the ground state has the state with $J = |L - S|$ and $J = L + S$, respectively. The magnetic moment parallel to J is expressed as $\mu_J = -g_J\mu_B J$ with

the Landé's g -factor $g_J = 3/2 + (S(S + 1) - L(L + 1))/2J(J + 1)$. As shown below, the orbital angular momentum of $3d$ electron is often almost quenched in materials and only the spin angular momentum survives.

1.2 Magnetic interaction and magnetic orders

Next, magnetic interactions between electrons in a system made of one unpaired electron on each atom are considered. The energy levels of the each electron are expected to form energy bands. When the coulomb repulsion between the electrons is negligible, the system becomes a metal as the energy band becomes half-filled. On the other hand, when the coulomb interaction between the electrons is strong enough, the system becomes an insulator with an energy gap generated by the coulomb repulsion.

The electronic state of such an insulator is often described by a Hubbard model with the Hamiltonian $H = \sum_{i,j,\sigma} t_{ij} c_{i\sigma}^\dagger c_{j\sigma} + U_0 \sum_i n_{i\uparrow} n_{i\downarrow}$. t_{ij} is a matrix element which express the hopping of electron from site j to site i and U_0 is the on-site coulomb repulsion between electrons. $c_{i\sigma}^\dagger$ and $c_{i\sigma}$ are operators which generate and annihilate the electron with spin σ at site i , and $n_{i\sigma} = c_{i\sigma}^\dagger c_{i\sigma}$, respectively.

To consider the magnetic interaction caused by the hopping of electrons, the second order perturbation process shown in the fig. 1.1 (a) is considered. The effective Hamiltonian for the hopping process is written as $H_{\text{eff}} = \sum_{i,j} 4t_{ij}^2/U_0 s_i \cdot s_j$. This interaction is always antiferromagnetic and called superexchange interaction. The term $4t^2/U_0$ is often written as J and the Hamiltonian $H = \sum_{i,j} J_{i,j} s_i \cdot s_j$ is called Heisenberg Hamiltonian. As there is also ferromagnetic direct exchange interaction, the sign of the magnetic interaction in real materials is determined by the balance of the two interactions. The superexchange interaction is often dominant and many materials are actually antiferromagnets.

The simplest spin system is a spin dimer coupled via antiferromagnetic interaction. The ground state of a spin dimer is a spin singlet state. The state is expressed as $1/\sqrt{2}(|\uparrow_1 \downarrow_2\rangle - |\downarrow_1 \uparrow_2\rangle)$: \uparrow_1 and \downarrow_1 indicate that the z -component of the spin on site-1 is $1/2$ and $-1/2$, respectively. The spin singlet state is made by the quantum mechanical mixing of the states with spin \uparrow on site-1 and spins \downarrow on site-2 and the state with spin \downarrow on site -1 and spin \uparrow on site-2.

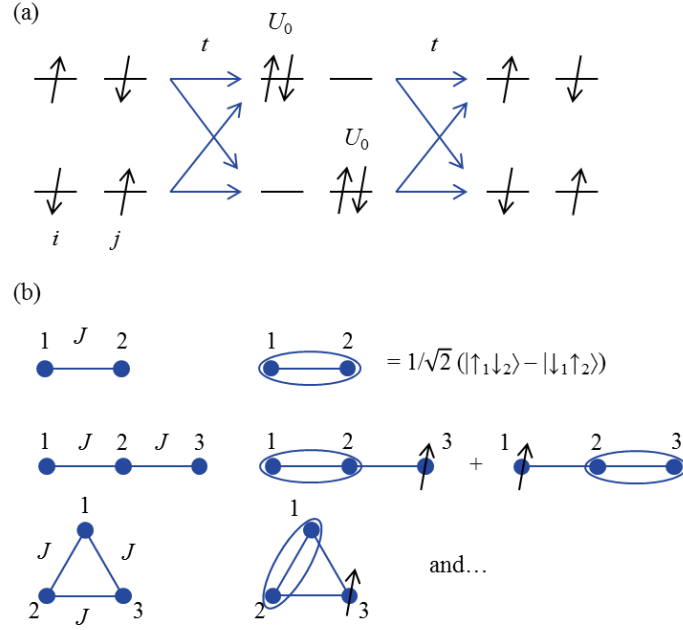


Figure 1.1. (a) Hopping process that cause superexchange interactions. (b) Antiferromagnetic spin dimer (top), antiferromagnetic linear spin trimer (middle), and antiferromagnetic triangular spin trimer (bottom). A ground state of the systems are also depicted.

In the same manner, the ground states of a linear trimer and a triangular spin trimer (fig.1.1 (b)), which are made of three spins, are expressed as follows.

Antiferromagnetic Linear Trimer

$$1/\sqrt{6}(|\uparrow_1 \uparrow_2 \downarrow_3\rangle + |\downarrow_1 \uparrow_2 \uparrow_3\rangle - 2 |\uparrow_1 \downarrow_2 \uparrow_3\rangle) = 1/\sqrt{6} (|\uparrow_1\rangle \times (|\uparrow_2 \downarrow_3\rangle - |\downarrow_2 \uparrow_3\rangle) + (|\uparrow_1 \downarrow_2\rangle - |\downarrow_1 \uparrow_2\rangle) \times |\uparrow_3\rangle)$$

$$1/\sqrt{6}(|\downarrow_1 \downarrow_2 \uparrow_3\rangle + |\uparrow_1 \downarrow_2 \downarrow_3\rangle - 2 |\downarrow_1 \uparrow_2 \downarrow_3\rangle) = 1/\sqrt{6} (|\downarrow_1\rangle \times (|\uparrow_2 \downarrow_3\rangle - |\downarrow_2 \uparrow_3\rangle) + (|\uparrow_1 \downarrow_2\rangle - |\downarrow_1 \uparrow_2\rangle) \times |\downarrow_3\rangle)$$

Antiferromagnetic Triangular Trimer

$$1/\sqrt{2}(|\uparrow_1 \downarrow_2\rangle - |\downarrow_1 \uparrow_2\rangle) \times |\uparrow_3\rangle$$

$$1/\sqrt{2}(|\uparrow_1 \downarrow_2\rangle - |\downarrow_1 \uparrow_2\rangle) \times |\downarrow_3\rangle$$

$$1/\sqrt{6}((|\uparrow_2 \downarrow_3\rangle - |\downarrow_2 \uparrow_3\rangle) \times |\uparrow_1\rangle - (|\uparrow_3 \downarrow_1\rangle - |\downarrow_3 \uparrow_1\rangle) \times |\uparrow_2\rangle)$$

$$1/\sqrt{6}((|\uparrow_2 \downarrow_3\rangle - |\downarrow_2 \uparrow_3\rangle) \times |\downarrow_1\rangle - (|\uparrow_3 \downarrow_1\rangle - |\downarrow_3 \uparrow_1\rangle) \times |\downarrow_2\rangle)$$

As the number of the spins in a system increases, the ground state is expected to become complicated. In the real material, the number of the spins is the order of Avogadro number and it is almost impossible to derive the ground state exactly. To investigate the ground state of the spin system, the classical spin model, where the spins are regarded as classical vectors, is considered. The

Heisenberg Hamiltonian $H = \sum_{i,j} J_{ij} \mathbf{S}_i \cdot \mathbf{S}_j$ is written as $H = 1/2 \sum_{\mathbf{q}} J(\mathbf{q}) \mathbf{S}_{\mathbf{q}} \cdot \mathbf{S}_{-\mathbf{q}}$ by the Fourier transformation, where $\mathbf{S}_{\mathbf{q}} = 1/\sqrt{N} \sum_i e^{-i\mathbf{q} \cdot \mathbf{r}_i} \mathbf{S}_i$, $J(\mathbf{q}) = \sum_i e^{-i\mathbf{q} \cdot (\mathbf{r}_i - \mathbf{r}_j)} J_{ij}$, and the \mathbf{q} is a wave vector within the first Brillouin-zone. Here, the state with a \mathbf{q} which gives the minimum of $J(\mathbf{q})$ is the candidate of the ground state.

For example, in the square lattice antiferromagnet with nearest neighbor (NN) interaction J , the $J(\mathbf{q}) = 2J(\cos q_x + \cos q_y)$, which is minimized by $\mathbf{q} = (\pi, \pi)$. In this state, the NN spins are arranged in the opposite directions. The lattice is split into the two sub-lattices and the antiferromagnetically ordered state is called the Néel state (fig. 1.2 (a)).

In the case of spin 1/2, the Néel state is not a real ground state. When the Hamiltonian is applied to the Néel state, another state is mixed to the Néel state due to the second term in $\mathbf{s}_i \cdot \mathbf{s}_j = s_i^z s_j^z + 1/2 (s_i^+ s_j^- + s_i^- s_j^+)$. This effect is called quantum fluctuation. In the simple case like square lattice antiferromagnet, the ground state is considered to be a Néel state with squeezed spin moment by the effect of quantum fluctuation.

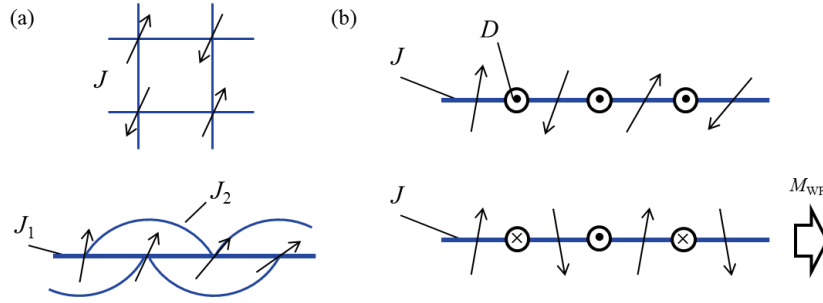


Figure 1.2. (a) Néel state on the square lattice (top) and the spiral spin order in the J_1 - J_2 chain magnet (bottom). (b) Spiral state (top) and the weak-ferromagnetic state with the net magnetic moment M_{WF} (bottom) caused by the DM interaction in the antiferromagnetic chain.

Magnets show various kinds of magnetic orders depending on the arrangement and types of magnetic interactions. For example, a J_1 - J_2 chain model is another typical spin model (fig. 1.2 (a)). In this model, in addition to the NN antiferromagnetic interaction J_1 , next nearest neighbor (NNN) antiferromagnetic interaction J_2 is present. The J_q considered above is written as $J_q = 2J_1 \cos q + 2J_2 \cos 2q$. The q which minimizes J_q depends on the ratio J_2/J_1 . When $J_2/J_1 < 4$, $q = \pi$ minimize the $J(q)$. When $J_2/J_1 > 4$, $q = \pm \cos^{-1}(-J_1/4J_2)$ minimize the $J(q)$; the spin state correspond to the helical spin state with the period of $2\pi/q$.

In addition to the exchange interactions, Dzyaloshinskii-Moriya (DM) interaction can affect the ground state spin structure. Classically, DM interaction between the spins S_i and S_j is written as $\mathbf{D} \cdot [\mathbf{S}_i \times \mathbf{S}_j]$, which acts to make the two spins lie in the same plane perpendicular to the D -vector and mutually tilted by 90° . It gives a different effect depending on the arrangement of the D -vector in the lattice. For a simple example, DM interaction added to the antiferromagnetic chain is considered (fig. 1.2 (b)). When they are arranged in the same direction along a chain, they stabilize a spiral spin structure. On the other hand, when they have the staggered arrangement along the chain, they cause a canting from the antiferromagnetic state. In the latter case, the net magnetic moment is not zero and the state is called weak-ferromagnetic state.

1.3 Magnetic frustration

The magnetic order of the simple magnet can often be understood by considering the classical spin model. In some magnets, all of the magnetic interactions are not satisfied simultaneously and the magnetic order is suppressed; this situation is called magnetic frustration. Magnets which have magnetic frustration (frustrated magnets) are expected to show unconventional magnetic states without conventional magnetic order. Magnetic frustration is mainly caused by the geometry of spins coupled by antiferromagnetic interactions (geometrical frustration) or by competing ferromagnetic and antiferromagnetic interactions (fig. 1.3). An example for the former case is the spin 1/2 Heisenberg antiferromagnet on the two-dimensional kagome lattice made of corner-sharing triangles. Example for the second case is found in magnets with a ferromagnetic NN coupling J_1 and antiferromagnetic NNN coupling J_2 on various kinds of lattices. Theoretically predicted novel phases in the two types of frustrated systems and their representative model compounds are summarized below.

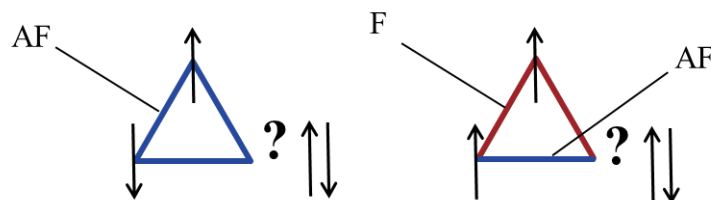


Figure 1.3. Geometrical frustration (left) and a frustration caused by the competing ferromagnetic and antiferromagnetic interactions (right).

1.3.1 Geometrical frustration

The energy of a classical triangular spin trimer is $J(\mathbf{S}_1 \cdot \mathbf{S}_2 + \mathbf{S}_2 \cdot \mathbf{S}_3 + \mathbf{S}_3 \cdot \mathbf{S}_1) = J/2 (\mathbf{S}_1 + \mathbf{S}_2 + \mathbf{S}_3)^2 - 9/8 J$, which is minimized by the condition $\mathbf{S}_1 + \mathbf{S}_2 + \mathbf{S}_3 = 0$. This condition is satisfied by tilting the three spins mutually 120° each other, which is called a 120° structure. In the lattice made of triangles such as triangular and kagome lattices, the classical ground state is made by extending the local 120° structure on the entire lattice. The 120° structure has a degree of freedom called vector chirality. The vector chirality $\boldsymbol{\kappa}$ is defined as $\boldsymbol{\kappa} = \mathbf{S}_1 \times \mathbf{S}_2 + \mathbf{S}_2 \times \mathbf{S}_3 + \mathbf{S}_3 \times \mathbf{S}_1$. For example, the 120° structure shown in the left of fig. 1.4 (a) is defined to have the positive vector chirality.

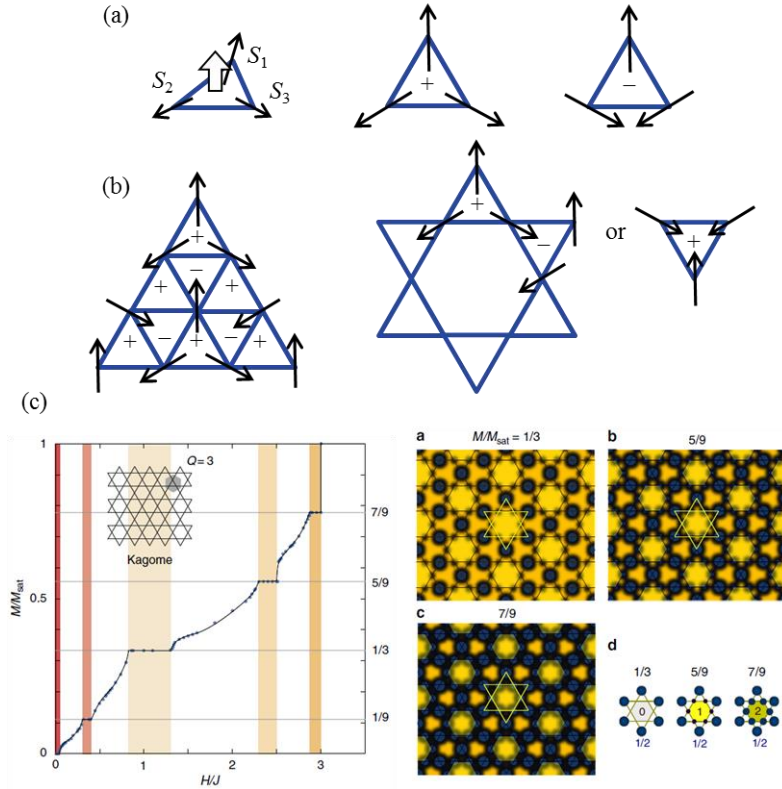


Figure 1.4. (a) Definition of the vector chirality (left). 120° structure on a triangle with positive (+, middle) and negative (-, right). (b) Classical ground states of triangular (left) and kagome (right) lattices. (c) Calculated magnetization curve of the spin 1/2 Heisenberg kagome antiferromagnet ([13], left). The plaquette VBC state where the size of the blue dots indicate the density of the spin at the site (right).

In the triangular lattice, extending the local 120° structure to the next edge-sharing triangles is straightforward and the long range order is formed as in the fig. 1.4 (b). Theoretical studies have

shown that the ground state is magnetically ordered even in the case of spin 1/2 [4-5]. In the case of kagome lattice, there is a degree of freedom of the vector chirality in extending the 120° structure to the next corner-sharing triangles, and arbitrary state can be a classical ground state as long as the local 120° structure is maintained (fig. 1.4 (b)). Therefore, the classical ground state is macroscopically degenerate. In the case of spin 1/2, the true ground state is still an open question, although there is a consensus that there is no conventional magnetic order. The candidates of the ground states are a quantum spin liquid state [6-9] or a valence bond crystal (VBC) state [10] which is made of ordered spin singlet states. The quantum spin liquid states are expected to show novel phenomena such as fractional excitations and superconductivity by making the system conducting [11].

In addition to the ground states without magnetic order, interesting phases are predicted to realize in the spin 1/2 kagome antiferromagnets in magnetic fields. The presence of the 1/3 plateau, where the magnetization curve becomes flat to magnetic field at the height of the 1/3 of the magnetization saturation, have been known [12]. The 1/3 plateau state is suggested to be a quantum superposition of the $\uparrow\uparrow\downarrow$ states on each triangles. Recent theoretical studies have revealed the magnetization plateaus at the 1/9, 1/3, 5/9, and 7/9 of the saturation magnetization [13-15]. Nishimoto et al. suggest that the 1/3, 5/9, and 7/9 plateau states are the new type of VBC state called plaquette VBC state, where spins on the hexagons make a spin singlet-like state. In the 1/3, 5/9, and 7/9 plateaus, the total spin on a hexagon is equal to 0, 1, and 2, respectively (fig. 1.6(c)), and the rest of the spins are polarized along the magnetic field. The 1/9 plateau is suggested to be a spin liquid state, but its nature is not well understood. It should be noted that the spin states in the magnetization plateau phases are still under discussion in the theoretical studies and no experimental realizations are found so far.

Herbertsmithite $\text{Zn}_{1-x}\text{Cu}_{3+x}(\text{OH})_6\text{Cl}_2$ is one of the most intensively studied spin 1/2 kagome antiferromagnets. It has the geometrically perfect kagome lattice with the space group $R\bar{3}m$. There is strongly antiferromagnetic NN interaction of approximately 200 K. In the studies using powder samples, neither long range magnetic order nor spin gap is observed down to 50 mK and the ground state is considered to be a gapless spin liquid state [16-18]. In the inelastic neutron experiments using a single crystal sample, no clear feature such as spin waves is observed and instead a broad continuous band (continuum) is observed in the dynamic structure factor $S_{\text{tot}}(\mathbf{Q}, \omega)$ (fig. 1.5 (a)). This result is considered to be the evidence of the fractionalized excitation from the gapless spin liquid

state [19]. The high-field magnetization measurement on single crystal sample is reported, but no anomaly is found in the magnetization curve up to 55 T (fig. 1.5 (b), [20]).

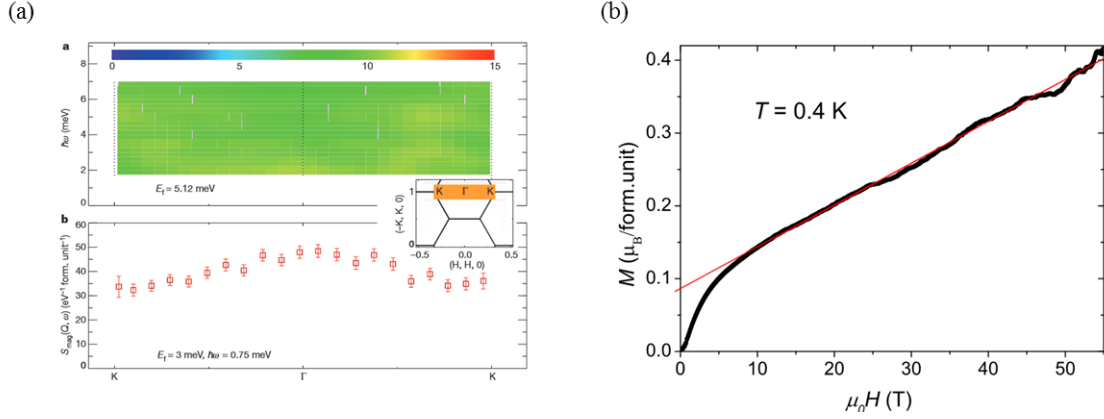


Figure 1.5. (a) Dynamic structure factor $S_{\text{tot}}(Q, \omega)$ of a single crystal sample of herbertsmithite counter plotted as a function of $\hbar\omega$ and Q [19]. A plot of magnetic part of the $S_{\text{tot}}(Q, \omega)$ along the K– Γ –K direction at low energy transfer $\hbar\omega = 0.75$ meV. (b) Magnetization curve of a single crystal sample of herbertsmithite [20].

Although the ground state of herbertsmithite has been claimed to be a gapless spin liquid state, it is not so straightforward because of the presence of disorder caused by Zn/Cu mixing. The effect of disorder in the spin 1/2 Heisenberg kagome antiferromagnet is examined theoretically. Singh et al. analyzed the effect of nonmagnetic defects and suggested that the ground state is a valence bond glass state made of randomly distributed spin singlet states, which shows gapless behavior [21]. Kawamura et al. studied the effect of bond randomness [22]. They also suggest that the ground state can be a valence bond glass state and the experimental results of herbertsmithite are explained in this scenario. On the other hand, recent NMR experiments on the single crystal sample suggest that the true ground state of herbertsmithite is a gapped spin liquid state [23], which is apparently different from the gapless spin liquid state proposed in the previous experimental studies. These results may demonstrate that the ground state of a frustrated magnet is sensitively affected by the disorder and intrinsic properties can easily be masked.

1.3.2 Competing ferromagnetic and antiferromagnetic interactions

When both ferromagnetic and antiferromagnetic interactions are present, they can cause frustration (fig. 1.3). An interesting magnetic phase expected in this type of frustrated magnets is the

spin nematic phase. The spin nematic phase is characterized by the formation of bound magnon pairs and the order of nematic directors.

The spin nematic phase is expected to appear near the ferromagnetic state such as in the frustrated magnet with dominant ferromagnetic interaction or in a strong magnetic field. The spin fluctuation from the ferromagnetic state is normally expressed by a wave called spin wave and its quantized particle is called magnon. Magnon spectrum is usually gapless and has the energy dispersion depending on the system. Shannon et al. found that in the frustrated square lattice with ferromagnetic NN interaction J_1 and NNN interaction J_2 in the diagonal direction (fig. 1.6 (a)), the magnon spectrum has the dispersionless zero energy mode, which indicates that the magnon is almost localized in the lattice due to the frustration caused by J_1 and J_2 [24]. Then, however, by forming a pair made of two magnons (bound magnon pair), the magnon pair can move around the lattice via the hopping process caused by J_2 and gain the kinetic energy. This instability of the ferromagnetic state caused by the formation of bound magnon pairs generates a novel magnetic phase, which is the spin nematic phase, near the ferromagnetic state [25].

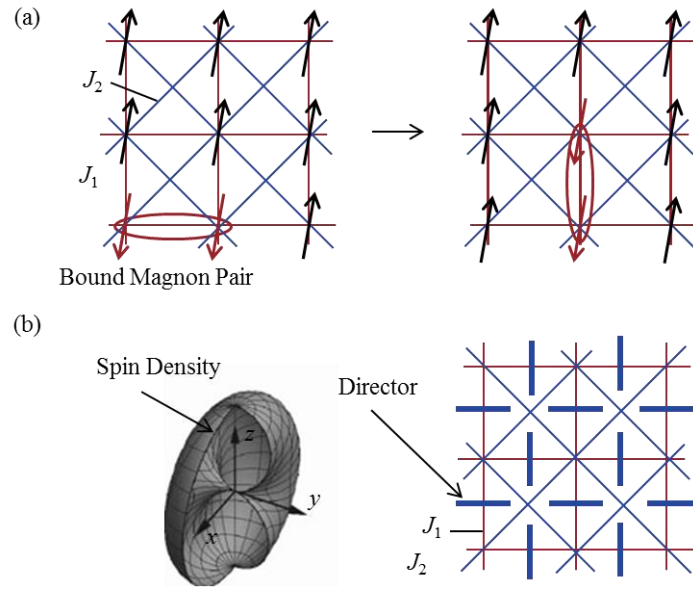


Figure 1.6. (a) Hopping process of a bound magnon pair in the J_1 - J_2 square lattice. (b) The spin density of the spin 1 with the director parallel to the y -axis [3]. The long range order of nematic director in the J_1 - J_2 square lattice (right).

There is no conventional magnetic order in the spin nematic phase, however, there is an order of nematic director. The nematic director is found in a spin 1 system, where state of a spin can be

written as $|x\rangle = i/\sqrt{2} (|1\rangle - |-1\rangle)$, $|y\rangle = 1/\sqrt{2} (|1\rangle + |-1\rangle)$, and $|z\rangle = -i|0\rangle$. The director of $|x\rangle$ is parallel to the x -axis, $|y\rangle$ to the y -axis, and $|z\rangle$ to the z -axis, respectively. The spin density is anisotropic around the director: the director indicates the direction where the spin density becomes small (fig. 1.6 (b)). In the case of spin 1/2, the director is not defined for a spin but for a pair of spins. In a ferromagnetically coupled spin dimer, three ground states can be written as follows and the director is defined as in the case of spin 1: $|x\rangle = i/\sqrt{2} (|\uparrow_1\uparrow_2\rangle - |\downarrow_1\downarrow_2\rangle)$, $|y\rangle = 1/\sqrt{2} (|\uparrow_1\uparrow_2\rangle + |\downarrow_1\downarrow_2\rangle)$, and $|z\rangle = -i/\sqrt{2} (|\uparrow_1\downarrow_2\rangle - |\downarrow_1\uparrow_2\rangle)$.

When the bound magnon pair is generated near the ferromagnetic state, the $\uparrow_i\uparrow_{i+1}$ and $\downarrow_i\downarrow_{i+1}$ states are mixed and the degree of freedom of the nematic director is expected to appear. In the nematic phase on the J_1 - J_2 square lattice, the nematic directors show an order as shown in the fig. 1.6 (b). To summarize, the nematic phase is considered to be a novel multipolar order state where there is no magnetic order but the order of nematic director. The realization of nematic phase is theoretically predicted in some spin system with competing ferromagnetic and antiferromagnetic interactions near the ferromagnetic state not only in the two-dimensional J_1 - J_2 square lattice, but also in one-dimensional J_1 - J_2 chain, three-dimensional J_1 - J_2 body-centered-cubic lattice [26-27]. It is noted that the phase is not observed in real materials thus far.

Several copper oxides have been studied as the model compounds of the spin 1/2 J_1 - J_2 chain. Theoretically, this system is expected to show rich magnetic phases in the magnetic field (fig. 1.7 (a)); helical spin order at low fields, spin density wave (SDW) order in the intermediate fields, and the spin nematic phase at high fields near the saturation of the magnetization (forced ferromagnetic state) [26,28]. LiCuVO_4 is a representative model compound for the system. It shows an incommensurate helical spin order at low fields and a longitudinal SDW order above 7 T, where the moments are aligned parallel to the field with their magnitudes modulated along the chains [29]. Furthermore, the magnetization curve shows an anomaly slightly below the saturation magnetic field; the magnetization changes linearly to the magnetic field with reduced slope between 40.5 and 44.4 T in $H // c$ before the saturation field of 46 T (fig. 1.7 (b), [30]). At the first stage, this anomaly was attributed to the realization of the theoretically predicted spin nematic phase. Later, however, the detailed NMR experiments performed at the corresponding field range revealed that the magnetization anomaly is caused by the certain defects on the chain generated by the Li/Cu site mixing [31]. Thus, the presence of the spin nematic phase in LiCuVO_4 is still unclear. A spin system with little disorder is necessary to study the physics of the spin nematic phase.

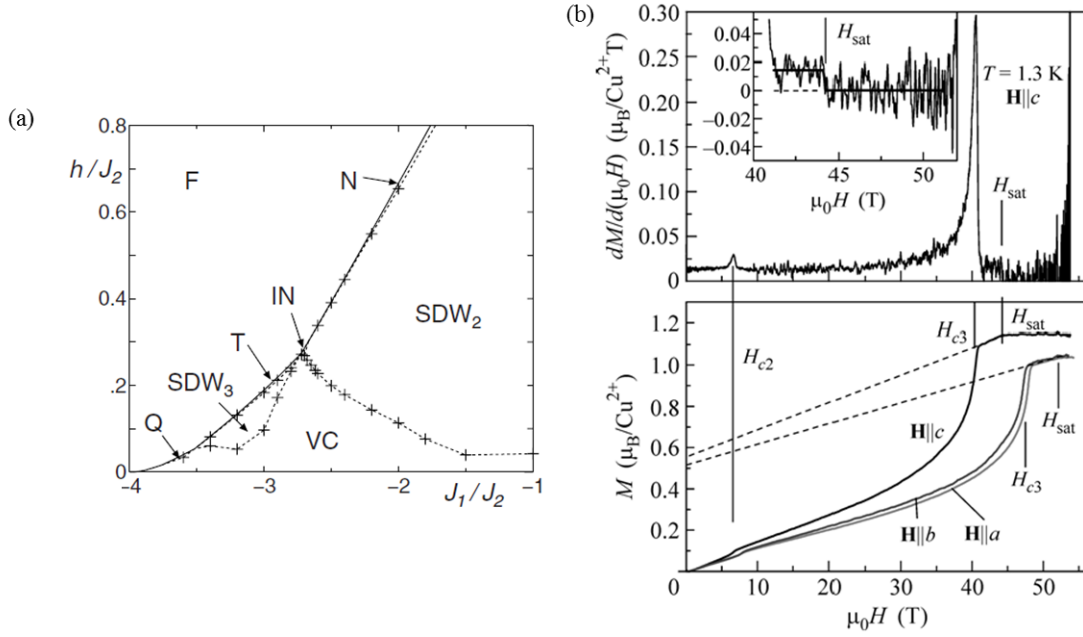


Figure 1.7. (a) Theoretically predicted phase diagram of the J_1 - J_2 chain magnet with ferromagnetic NN interaction J_1 and antiferromagnetic NNN interaction J_2 [26]. VC indicates the vector chiral order, which is expected to become a helical spin order in real materials. F and N indicate the ferromagnetic and nematic phases, respectively. For example, if the J_1/J_2 is -2 , the VC, SDW, N, and F phases are expected to appear as increasing the magnetic field. IN, T, and Q are other multipolar states related to the multi-magnon bound states. (b) Magnetization curves of LiCuVO_4 [30].

1.4 Crystal chemistry and magnetic interaction of copper oxides

1.4.1 CuO_6 octahedron and magnetic interactions

Copper atom often exists as a Cu^{2+} ion in oxides and there are nine electrons in five $3d$ orbitals ($n = 3$, $l = 2$, $m = \pm 2, \pm 1$, and 0). By applying the rules of electronic configuration, the Cu^{2+} ion should have $L = 2$ and $S = 1/2$ without spin-orbit coupling and $J = 5/2$ with spin-orbit coupling. Therefore, the effective magnetic moment defined as $\mu_{\text{eff}} = g_J \sqrt{J(J+1)} \mu_B$ is expected to be $3.55 \mu_B$ for $J = 5/2$. On the other hand, experimentally observed μ_{eff} is approximately $1.95 \mu_B$, which is close to $1.73 \mu_B$ expected for $g = 2.0$, $L = 0$, and $S = 1/2$. The discrepancy between expected value for $J = 5/2$ and experimental value is caused by the electric potential made by the O ions around the Cu ions.

Typically, Cu^{2+} ion is surrounded by six O^{2-} ions (CuO_6 octahedron) in oxides (fig. 1.8 (a)). The degeneracy of the five $3d$ orbitals is lifted by the electric potential made by O^{2-} ions. In the electric potentials made of regular octahedron with cubic symmetry, there are two groups of orbitals with

different energy levels called t_{2g} (d_{xy} , d_{yz} , and d_{zx}) and e_g ($d_{3z^2-r^2}$, and $d_{x^2-y^2}$) orbitals. The energy of the t_{2g} orbitals is lower than that of the e_g orbitals because they extend avoiding the O^{2-} ions and the coulomb repulsion is reduced compared to the e_g orbitals. It is noted that the d_{xy} and $d_{x^2-y^2}$ orbitals are made by the linear combinations of the orbitals with $m = \pm 2$ as $\varphi_{xy} = i/\sqrt{2}(\varphi_{322} - \varphi_{32-2})$ and $\varphi_{x^2-y^2} = 1/\sqrt{2}(\varphi_{322} + \varphi_{32-2})$; φ_{nlm} is the atomic orbital which have quantum numbers n , l , and m . Similarly, the d_{yz} , and d_{zx} orbitals are made of orbitals with $m = \pm 1$ as $\varphi_{yz} = i/\sqrt{2}(\varphi_{321} + \varphi_{32-1})$ and $\varphi_{zx} = -1/\sqrt{2}(\varphi_{321} - \varphi_{32-1})$ and $d_{3z^2-r^2}$ orbital corresponds to the orbital with $m = 0$ as $\varphi_{3z^2-r^2} = \varphi_{320}$. The expected values of the orbital angular momentum of each of the t_{2g} and e_g orbitals are zero. Therefore, when the state of an electron is described by only one of the five orbitals, the orbital angular momentum is lost. This effect is known as quenching of the orbital angular momentum by the crystal field.

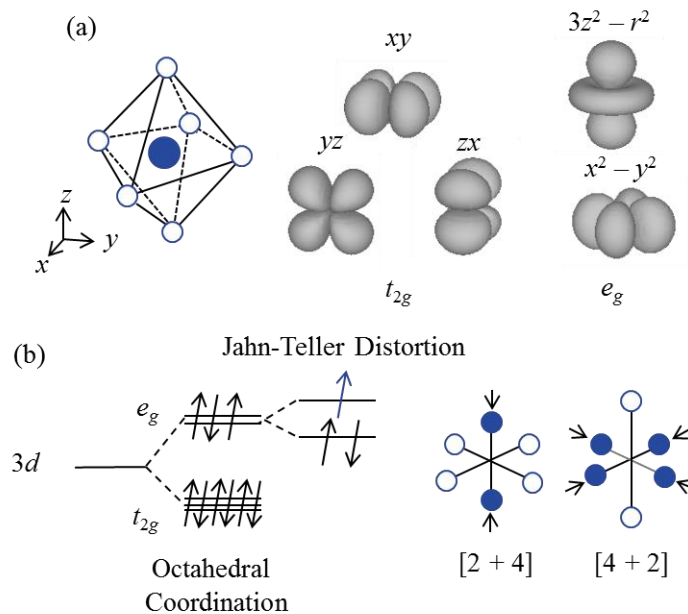


Figure 1.8. (a) Electron density of the d orbitals in the octahedral coordination. (b) Energy levels of the d orbitals in the octahedral coordination before and after Jahn-Teller distortion (left). Two ways of Jahn-Teller distortion in the case of octahedral coordination (right).

As a Cu^{2+} ion has nine $3d$ electrons, t_{2g} and e_g orbitals are fully and partly occupied, respectively. When there are degenerate orbitals that are partly occupied, the energy can be lowered further by the distortion of the octahedron (Jahn-Teller distortion). In the case of Cu^{2+} ion, the total energy of the electrons in the e_g orbitals are lowered compared to the energy with regular octahedron by the Jahn-Teller distortion. There are two ways of distortion; when the octahedron is elongated and

squeezed along the z -axis, the unpaired electron is accommodated in the $d_{x^2-y^2}$ and $d_{3z^2-r^2}$ orbitals, respectively. In copper oxides, Jahn-Teller distortions are easily distinguished by looking at the crystal structure; typical squeezed Cu-O bonds are 1.8-2.0 Å and the elongated Cu-O bonds are 2.2-2.4 Å. The coordinations to select $d_{x^2-y^2}$ and $d_{3z^2-r^2}$ orbitals are called [4 + 2] and [2 + 4] coordinations, respectively.

As a result of quenched orbital angular momentum and the Jahn-Teller distortion, copper oxides can be regarded as a system made of one electron in the $d_{x^2-y^2}$ or $d_{3z^2-r^2}$ orbitals on each Cu site. The superexchange interactions are caused by the hopping process via the $2p$ orbitals ($n = 2, l = 1$) of bridging O^{2-} ions. There is a general rule called Goodenough-Kanamori rule about the sign of superexchange interactions. This rule suggests that when the $M-L-M$ bond angle is close to 180° , the magnetic interaction is antiferromagnetic and when the angle is close to 90° , it is ferromagnetic: M and L are the magnetic ion and ligand ion.

As a typical example, the interactions between spins in Cu $3d_{x^2-y^2}$ and O $2p$ orbitals caused by the hopping process shown in the fig. 1.9 (a) are considered. Step 1: the spin on Cu A site is fixed to \uparrow . The electron with spin \downarrow on O $2p$ orbital can be transferred to Cu A site. Step 2: in the case of 180° bond, O $2p$ orbital with spin \uparrow can hybridize with the $3d$ orbital of the Cu B site and gain the bonding energy if the Cu B site has spin \downarrow . As a result, the energy is lowered if the Cu B site has the \downarrow spin and the net antiferromagnetic interaction arises between spins on Cu A and B sites. On the other hand, in the 90° bond, the O $2p$ orbital and Cu $3d$ orbital of the Cu B experience the direct exchange interaction. Therefore, the overall interaction is ferromagnetic. Step 3: the electron with spin \downarrow on Cu A site returns to the O ion and the system returns to the initial state.

The 180° bond is found when the CuO_6 octahedra share the corners (fig. 1.9 (b)) such as in the perovskite-type oxides, which is related to the cuprate high-temperature superconductors. The 90° bond is found when the CuO_6 octahedra share the edges (fig. 1.9 (b)). This configuration is often found in the quasi one-dimensional chain compounds such as $CuGeO_3$, which is considered to show a spin-Peierls transition. Mizuno et al. have studied the electronic states and the relationship between the bond angles and magnetic interactions in copper oxides containing edge-sharing CuO_2 chains. In their study, they showed that the interaction is ferromagnetic when the bond angle is smaller than approximately 95° and becomes antiferromagnetic when the angle is larger than that (fig. 1.9 (c), [32]).

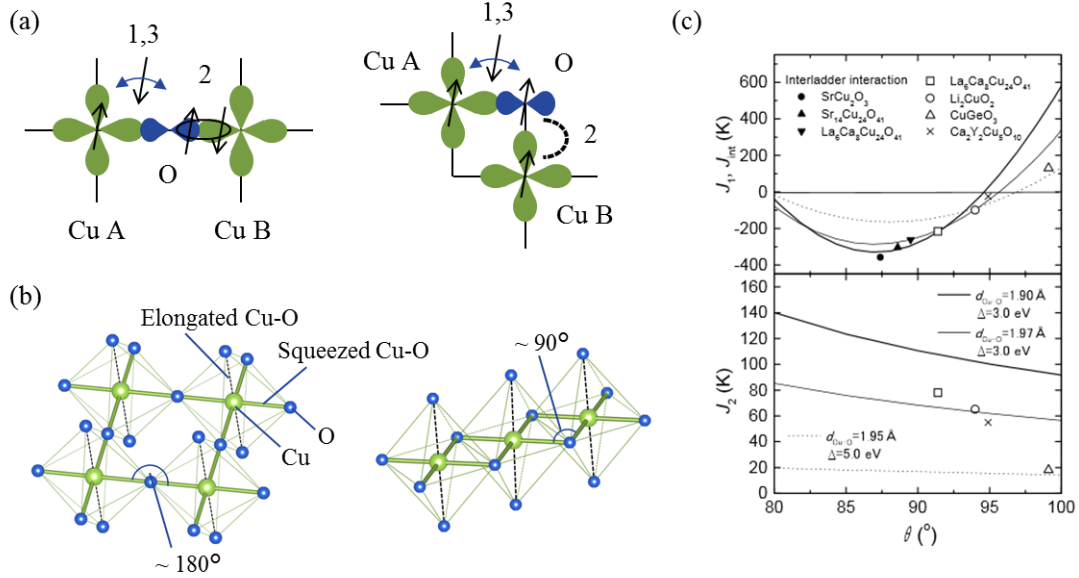


Figure 1.9. (a) The hopping process of Cu $3d_{x^2-y^2}$ and O $2p$ orbitals in the case of 180° bond (left) and 90° bond (right). (b) The 180° bond (left) and 90° bond (right) of CuO₆ octahedra found in the copper oxides. The elongated and squeezed Cu-O bonds are depicted by thick and dashed lines, respectively. (c) Cu-O-Cu angle dependence of magnetic interactions of edge-sharing CuO₆ octahedra [32].

Next, I summarize the materials with frustrated spin lattices focusing on the way of the connectivity of the polyhedra containing transition metal ion at the center. In most of the materials, corner-sharing or edge-sharing octahedra form frustrated lattices. Materials with pyramidal coordination polyhedra also realize unique frustrated spin lattices. The crystal structures of kagome copper minerals are stated in detail.

1.4.2 Kagome lattice

The kagome lattice made of corner-sharing octahedra (fig. 1.10 (a)) is found in the jarosite-type crystal structure with the chemical formula $AM_3(OH)_6(SO_4)_2$ ($A = K^+, Rb^+, Cs^+$ etc., and $M = V^{3+}$ ($S = 1$), Cr^{3+} ($S = 3/2$), Fe^{3+} ($S = 5/2$)) [33]. Strongly antiferromagnetic intralayer interaction is present in Fe- and Cr- jarosites and ferromagnetic intralayer interaction is present in V-jarosites. Similar kagome layer is found in some metal organic framework (MOF) compounds which commonly have layers made from corner-sharing MO_2F_4 octahedra ($M = Mn^{2+}$ ($S = 5/2$), Fe^{2+} ($S = 2$), Co^{2+} ($S = 3/2$),

Ni^{2+} ($S = 1$)) separated by organic molecules [34]. They have moderately strong intralayer antiferromagnetic interactions.

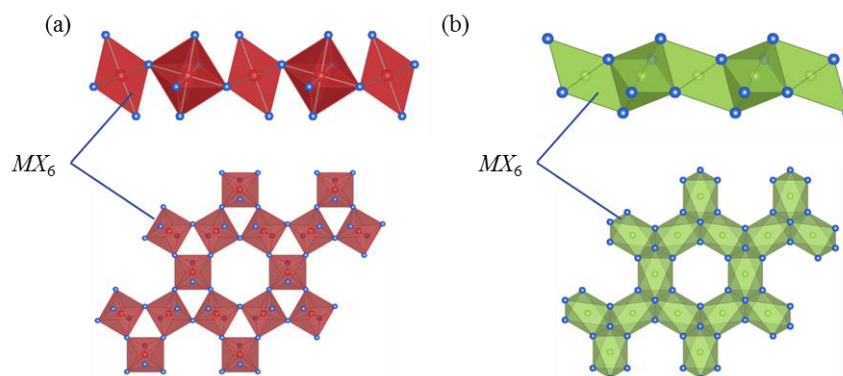


Figure 1.10. Side views and the top views of the kagome layers made of (a) corner-sharing MX_6 octahedra and (b) edge-sharing MX_6 octahedra, where M is the transition metal ions and X is the ligand anion such as O, OH, F, Cl, etc.

Kagome lattice made of edge-sharing octahedra (fig. 1.10 (b)) are found in many copper minerals. The crystal structures of kagome minerals may be classified into four groups: herbertsmithite-type, kapellasite-type, volborthite-type, and vesignieite-type (fig. 1. 11). Herbertsmithite $\text{ZnCu}_3(\text{OH})_6\text{Cl}_2$ has the kagome layer made of edge-sharing $\text{Cu}(\text{OH})_4\text{Cl}_2$ octahedra and the layers are separated by another ZnO_6 octahedra, which are located above and below the triangles of the kagome lattice [16]. A similar layered structure is found in the mineral barlowite $\text{Cu}_4(\text{OH})_6\text{FBr}$ [35] and $\text{CdCu}_3(\text{OH})_6\text{Cl}_2$ [36] although the way of the stacking of the layers are different from herbertsmithite.

Kapellasite $\text{ZnCu}_3(\text{OH})_6\text{Cl}_2$ also has a kagome layer made of $\text{Cu}_4\text{O}_4\text{Cl}_2$ octahedra [37]. The feature of the kagome layer is that there is another cation (Zn in kapellasite) at the center of the hexagons of the kagome lattice of Cu atoms. This type of kagome layer is found in the minerals haydeeite $\text{MgCu}_3(\text{OH})_6\text{Cl}_2$ [38] and centennialite $\text{CaCu}_3(\text{OH})_6\text{Cl}_2 \cdot x\text{H}_2\text{O}$ [39] and $\text{CdCu}_3(\text{OH})_6(\text{NO}_3)_2 \cdot x\text{H}_2\text{O}$ [40]. The layers are coupled via van der Waals interaction or separated by some crystal water molecules. The mineral edwardsite $\text{Cd}_2\text{Cu}_3(\text{OH})_6(\text{SO}_4)_2 \cdot 4\text{H}_2\text{O}$ has related kagome layers which are separated by thick layer made of $\text{CdO}_3(\text{H}_2\text{O})_3$ octahedra and SO_4 tetrahedra [41-42, P5].

Volborthite $\text{Cu}_3\text{V}_2\text{O}_7(\text{OH})_2 \cdot 2\text{H}_2\text{O}$ has a kagome layer made of edge-sharing $\text{CuO}_4(\text{OH})_2$ octahedra [43-44]. The VO_4 tetrahedra are located above and below the hexagons of the kagome lattice. The VO_4 tetrahedra of the adjacent layers share corners to form V_2O_7 pillars. A similar kagome layer is found in the mineral engelshauptite $\text{KCu}_3\text{V}_2\text{O}_7(\text{OH})_2\text{Cl}$ [45]. Vesignieite $\text{BaCu}_3\text{V}_2\text{O}_8(\text{OH})_2$ has a

kagome layer made of $\text{CuO}_4(\text{OH})_2$ octahedra and VO_4 tetrahedra which is similar to volborthite [46-47]. However, the adjacent layers of vesignieite are shifted to accommodate the large Ba^{2+} ions compared with volborthite: the VO_4 tetrahedra in the adjacent layer do not share the corner. The Sr-analogue of vesignieite $\text{SrCu}_3\text{V}_2\text{O}_8(\text{OH})_2$ [48] is also synthesized. Similar layered structures with AsO_4 tetrahedra are found in the minerals bayldonite $\text{PbCu}_3\text{As}_2\text{O}_8(\text{OH})_2$ [49] and $\text{KCu}_3\text{As}_2\text{O}_7(\text{OH})_2$ [50-51].

The octahedra in copper minerals are strongly distorted due to the Jahn-Teller effect, but perfect kagome geometry is maintained in some of the minerals. For example, the Jahn-Teller distortion to squeeze the bonds shown in the fig. 1.12 maintain perfect kagome geometry. In the case of the left figure, the $d_{x^2-y^2}$ -type orbitals carry spin 1/2 and this type of layer is found in the herbertsmithite-type and kapellasite-type minerals. In the case of the right figure, the $d_{3z^2-r^2}$ -type orbitals carry spin 1/2 and this type of layer is found in vesignieite and engelhauptite. In volborthite-type and vesignieite-type minerals, various orbital patterns are realized in distorted kagome lattices. In some compounds like volborthite, $\text{SrCu}_3\text{V}_2\text{O}_8(\text{OH})_2$, balydonite, and $\text{KCu}_3\text{As}_2\text{O}_7(\text{OH})_2$ both of the $d_{x^2-y^2}$ -type and $d_{3z^2-r^2}$ -type orbitals seem to coexist in one kagome layer. Moreover, in volborthite, changes in the orbital types or the orbital orientation take place as a function of temperature, which will be addressed in detail in the present thesis.

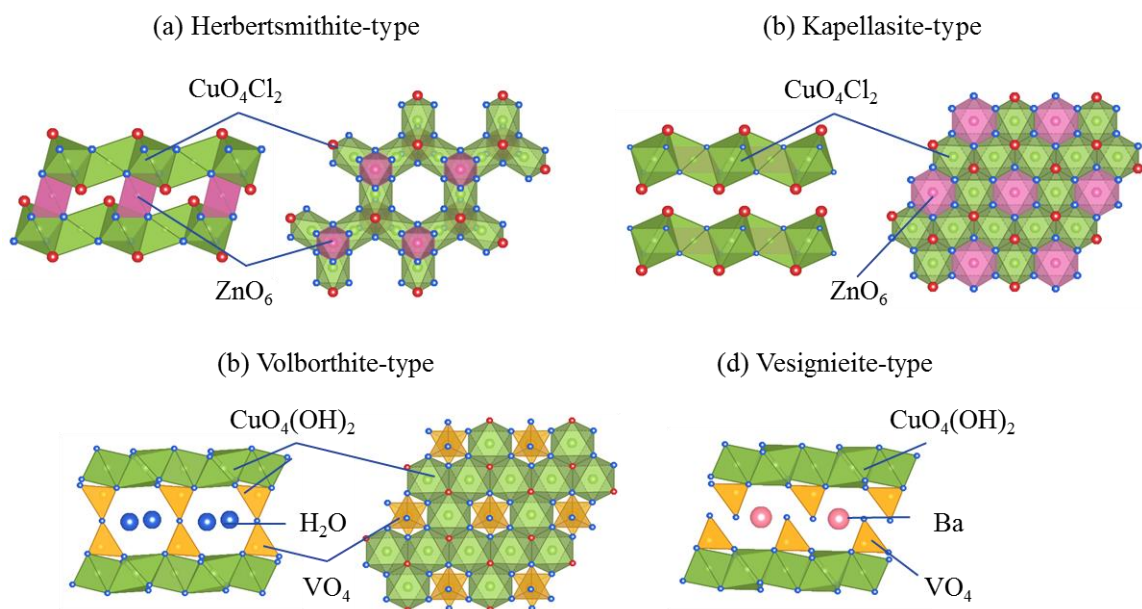


Figure 1.11. Crystal structures of four types of kagome minerals: (a) herbertsmithite (b) kapellasite (c) volborthite, and (d) vesignieite.

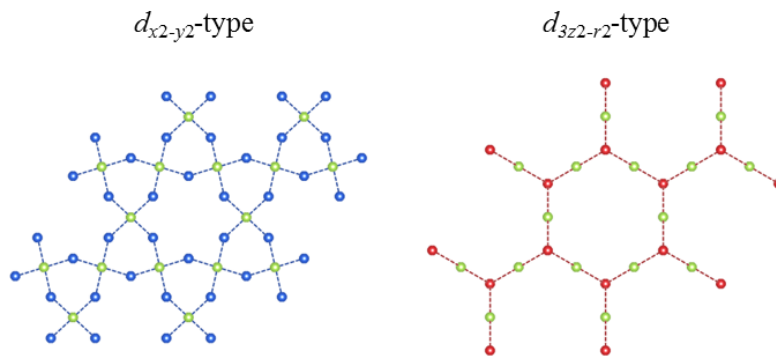


Figure 1.12. The squeezed Cu-O bonds to select the $d_{x^2-y^2}$ -type orbitals in the [4 + 2] coordination (left) and $d_{3z^2-r^2}$ -type orbitals in the [2 + 4] coordination (right) in the kagome layers made of edge-sharing MX_6 octahedra. Note that, in both cases, the three-fold axis remains to keep the perfect kagome lattice.

Some analogues of kagome copper minerals containing other transition metals are reported. For example, the Co-analogues of herbertsmithite and volborthite [52-53] and Co- and Ni- analogues of vesignieite are found in nature or synthesized [54-55]. In addition, kagome layers made of edge-sharing octahedra are found in many compounds such as $Ca_2Pt_3O_8$ (Pt^{4+} , $S = 0$) [56], $Fe_4Si_2Sn_7O_{16}$ (Fe^{2+} , $S = 2$) [57], $Pb_3Mn_5V_2O_{16}$ (Mn^{4+} , $S = 3/2$) [58], $KM_3Ge_2O_9$ ($M = V^{3+}$ ($S = 1$), Mn^{3+} ($S = 2$)) [59-60], and a series of fluorides with the chemical formula $A_2M_3BF_{12}$ ($M = Mn^{2+}$ ($S = 5/2$), Cu^{2+} ($S = 1/2$)) [61-62].

The pyramidal coordination polyhedra also enables the formation of unique kagome-like spin lattices. In a MOF compound $[NH_4]_2[C_7H_{14}N][V_7O_6F_{18}]$, corner sharing VOF_5 octahedra, which may be regarded as square pyramidal VOF_4 units with a short V-O bond, form a layered structure (fig. 1.13 (a), [63]). The V^{4+} ions with $S = 1/2$ form a “breathing” kagome lattice, which is made of large and small triangles. In a fluoride $NaBa_2Mn_3F_{11}$, pentagonal bipyramidal MnF_7 units form a layer, in which Mn^{2+} ions with $S = 5/2$ form a kagome-like lattice [64, P4]. The NN MnF_7 units share edges with each other and the NNN MnF_7 units share corners, where NN interaction J_1 and NNN interaction J_2 are expected to arise (fig. 1.13 (b)). We call this lattice the kagome-triangular lattice as it is regarded as an intermediate lattice topologically connected between kagome ($J_2 = 0$) and triangular ($J_1 = J_2$) lattices; it can also be a set of triangular clusters ($J_1 = 0$). This type of layer is known as α - U_3O_8 -type layer and found in a series of oxides with the formula of $A_xM_{3n+1}O_{8n+3}$ ($M = Nb^{5+}$ ($S = 0$), Ta^{5+} ($S = 0$)) [65].

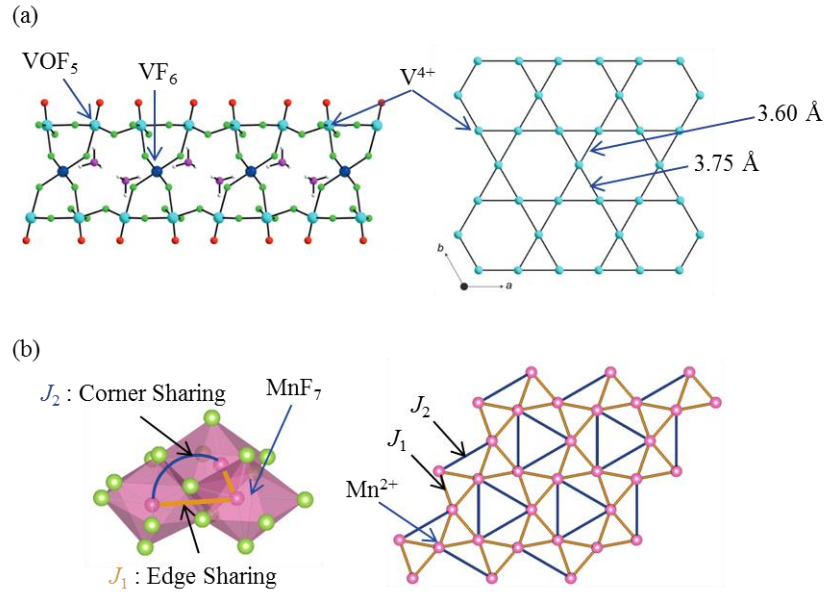


Figure 1.13. (a) $[V_7O_6F_{18}]$ layer made of VOF_5 and VF_6 octahedra (left) and the “breathing” kagome lattice made of V^{4+} ions in $[NH_4]_2[C_7H_{14}N][V_7O_6F_{18}]$ [63]. (b) Connectivity of MnF_7 pentagonal bipyramids (left) and the kagome-triangular lattice made of Mn^{2+} ions in $NaBa_2Mn_3F_{11}$.

1.4.3 J_1 - J_2 chain and J_1 - J_2 square lattice

The crystal structures that generate competing ferromagnetic NN interaction J_1 and antiferromagnetic NNN interaction J_2 are relatively rare in materials. For the J_1 - J_2 chain, most of the candidate materials contain edge-sharing CuO_6 octahedra. The ferromagnetic J_1 arise via the nearly 90° Cu-O-Cu superexchange path and antiferromagnetic J_2 arise via the Cu-O-O-Cu superexchange path (fig. 1.14 (a)). $LiCuVO_4$, $PbCuSO_4(OH)_2$, and $Rb_2Cu_2Mo_3O_{12}$ are well studied as the model compounds of the system [29,66-67].

Some compounds with square pyramidal coordination realize frustrated lattices with competing ferromagnetic and antiferromagnetic interactions. In β - $TeVO_4$ [68], which is studied as a J_1 - J_2 chain magnet, corner-sharing VO_5 square pyramids with V^{4+} ($S = 1/2$) form a chain, where ferromagnetic J_1 via the V-O-V path and antiferromagnetic J_2 via V-O-Te-O-V path are expected (fig. 1.14 (b)). Almost all of the model compounds for the J_1 - J_2 square lattice magnet are layered vanadium oxides, which have layers made of VO_5 square pyramids connected via nonmagnetic MO_4 tetrahedra ($M = Si^{4+}, Ge^{4+}, P^{5+}, Mo^{6+}$) [69]. The J_1 and J_2 couplings are caused via the V-O-O-V paths (fig. 1.14 (c)).

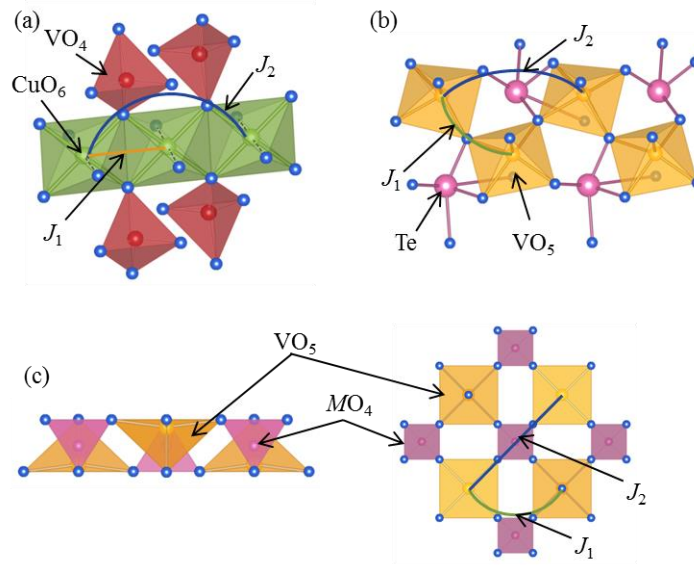


Figure 1.14. J_1 - J_2 chains found in the crystal structures of (a) LiCuVO_4 and (b) $\beta\text{-TeVO}_4$. (c) J_1 - J_2 square lattice found in the layered vanadium oxides made of VO_5 square pyramids and MO_4 tetrahedra.

1.5 Scope of the thesis

The aim of this thesis is to find novel magnetic phases or magnetic orders in frustrated magnets especially in copper minerals with kagome lattice, where magnetic frustration is expected. The previously studied kagome copper minerals and their features are summarized in table 1.1. Most of them have been studied using polycrystalline samples and known to show certain magnetic orders, which are not well understood. Their spin states in the high magnetic field region, where the realization of novel magnetic phases are predicted in recent theoretical studies, are even less understood.

The quality of samples is critical in the experimental study of frustrated magnetism. A large single crystal enables detailed characterization including anisotropy measurements. Moreover, a single crystal XRD experiment is a powerful tool to determine the crystal structure, which is important to consider an appropriate spin model. Furthermore, previous studies on herbertsmithite and LiCuVO_4 have demonstrated the importance of getting rid of even small disorder in the case of frustrated magnets.

Based on these circumstances, I expect a chance of finding novel magnetic phases or magnetic orders by preparing high quality single crystal samples and performing detailed magnetic properties measurements up to high magnetic field regions. In addition, studying new candidates of frustrated

magnets always provide the possibility of finding novel magnetic phases and the perspectives for the further material exploitation.

I have focused on three copper minerals: volborthite $\text{Cu}_3\text{V}_2\text{O}_7(\text{OH})_2 \cdot 2\text{H}_2\text{O}$, engelhauptite $\text{KCu}_3\text{V}_2\text{O}_7(\text{OH})_2\text{Cl}$, and vesignieite $\text{BaCu}_3\text{V}_2\text{O}_8(\text{OH})_2$, which are closely related to each other in the crystal structures. Volborthite and vesignieite have distorted and regular kagome lattices, respectively. In both of the materials, unusual magnetic properties are observed in the previous studies using powder samples, which have not yet clarified possibly due to the lack of single crystal. I have successfully synthesized high quality single crystals of large enough size, characterized their crystal structures and investigated their magnetic properties in wide temperature and magnetic field ranges. Engelhauptite is a new member of kagome copper minerals reported in 2013, which is synthesized and studied in this work for the first time. It has a distorted kagome lattice, and the investigation of the structural and magnetic properties have provided the clues to understand the complicated magnetic properties of volborthite as well as engelhauptite itself. In addition, I have studied the structural and magnetic properties of AMoOPO_4Cl ($A = \text{K}, \text{Rb}$) [70], which is considered to be rare realizations and the new candidates of the J_1 - J_2 square lattice magnets.

Based on thus obtained data, I have developed the crystal chemistry of the kagome minerals and clarified their unusual magnetic properties.

Table 1.1. Experimental studies of kagome copper minerals

Material (Mineral Name)	J or θ	T_N	High Field Measurement	Single Crystal	Comment /References
ZnCu ₃ (OH) ₆ Cl ₂ (Herbertsmithite)	200 K	< 50 mK	No Anomaly up to 55 T (Single Crystal)	○	Zn/Cu Disorder [16-20]
Cu ₄ (OH) ₆ FBr (Barlowite)	180 K	15.4 K	No Anomaly up to 60 T (Single Crystal)	○	Extra Cu ²⁺ Ions [35]
CdCu ₃ (OH) ₆ Cl ₂	150 K	< 2 K	×	×	[36]
ZnCu ₃ (OH) ₆ Cl ₂ (Kapellasite)	-9.5 K	< 20 m K	×	×	Zn/Cu Disorder [37]
MgCu ₃ (OH) ₆ Cl ₂ (Heydeckite)	-28 K	4.2 K	×	×	Mg/Cu Disorder [38]
CaCu ₃ (OH) ₆ Cl ₂ •xH ₂ O (centennialite)	56 K	7 K	×	×	[39]
CdCu ₃ (OH) ₆ (NO ₃) ₂ •xH ₂ O	114 K	2.9 K	×	×	[40]
Cd ₂ Cu ₃ (SO ₄) ₂ (OH) ₆ •4H ₂ O (Edwardsite)	51 K	4.3 K	Saturation toward 1/3 (Polycrystalline)	×	[41-42,P5]
Cu ₃ V ₂ O ₇ (OH) ₂ •2H ₂ O (Volborthite)	115 K	1 K	Steps and 2/5 Plateau (Polycrystalline)	This Study	[43-44]
KCu ₃ V ₂ O ₇ (OH) ₂ Cl (Engelhauptite)	×	×	×	This Study	[45]
BaCu ₃ V ₂ O ₈ (OH) ₂ (Vesignieite)	55 K	9 K	2/5 Plateau (Polycrystalline)	This Study	[46-47]
SrCu ₃ V ₂ O ₈ (OH) ₂	100 K	11 K	×	×	[48]
KCu ₃ As ₂ O ₇ (OH) ₃	-13.4 K	7.2 K	×	×	Ferroelectric below T_N [50-51]
PbCu ₃ As ₂ O ₈ (OH) ₂ (balydonite)	×	×	×	×	[49]

Chapter 2. Experiments

2.1 Synthesis

Samples of kagome minerals were prepared by the hydrothermal technique. Reactions were performed in the Teflon beaker with the volume of 45-790 ml sealed in the stainless autoclave (OM Labotech, fig. 2.1). The details of the synthetic conditions of each material are given in the corresponding chapters.

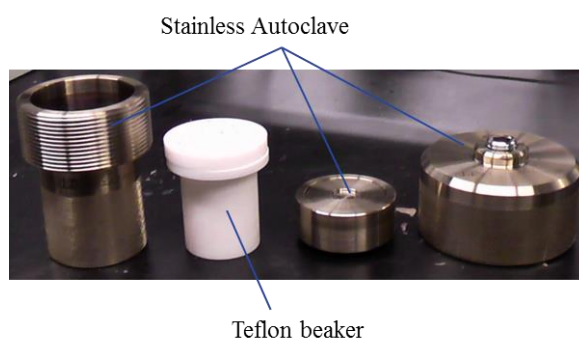


Figure 2.1. Teflon beaker and the parts of stainless autoclave.

2.2 Powder XRD

The powder samples and crashed single crystals were characterized by the Bragg-Brentano-type X-ray diffractometer with Cu-K α radiation (RINT2000, RIGAKU) in the laboratory. The samples were well ground in an agate mortar and put on a sample plate made of single crystal Si or SiO₂ glass. Measurements were performed in the θ -2 θ scan. The refinements of lattice constants and Rietveld analysis of the diffraction data were performed using the RIETAN-FP software [71].

The important criteria of the Rietveld refinements are $R_{wp} = (\sum_i w_i (y_i - y_i(\text{calc}))^2 / \sum_i w_i y_i^2)^{1/2}$ and goodness of fit S . y_i and $y_i(\text{calc})$ are the intensity of the observed and calculated reflections and $w_i = 1/y_i$. $S = (\sum_i w_i (y_i - y_i(\text{calc}))^2 / (N - P))^{1/2}$, where N and P are the number of y_i and refined parameters, respectively. When the refinement is perfect, the S is 1. The refinements were performed until the parameters converge and R_{wp} was minimized. Typically, when the S becomes smaller than 1.3, the refinements are considered satisfactory in the Rietveld method.

2.3 Single crystal XRD

Single crystal XRD experiments at 150-350 K were performed in a three-axis X-ray diffractometer with CCD two-dimensional detector (Bruker) or an imaging plate XRD system (Rapid, Rigaku) with Mo-K α radiation in the X-ray laboratory in ISSP, the University of Tokyo. Low temperature measurements at 50 and 200 K were performed using synchrotron radiation source at BL8A in KEK, Tsukuba. The measurements were performed with the help of Prof. Junichi Yamaura and Dr. Takeshi Yajima. Structural determination by the direct method and data refinements were performed using the SHELX 2013 software [72].

Typical criteria of the refinements are $R1 = \sum_i |F_i - F_i(\text{calc})| / \sum_i |F_i|$, $wR2 = (\sum_i w_i (F_i - F_i(\text{calc}))^2 / \sum_i w_i F_i^2)^{1/2}$, and goodness of fit $S = (\sum_i w_i (F_i - F_i(\text{calc}))^2 / (N - P))^{1/2}$. F_i and $F_i(\text{calc})$ are the intensity of the observed and calculated reflections. w_i is the weight of the reflection calculated from the uncertainty of the measurement, intensity of the reflection, and the parameters determined during the refinement. N and P are the number of F_i and refined parameters, respectively. Refinements were performed until the R -values are minimized. The final $R1$ is typically less than several percent and the S should be close to 1.

2.4 Magnetization

Magnetization measurements at 1.8-350 K and 0-7 T were performed using a commercial SQUID magnetometer (MPMS, Quantum Design) in ISSP. The sample holder made of quartz rod or plastic straws were used for the measurements. The single crystals or powder samples wrapped in the Al foil were fixed by the small amount of varnish to the sample holder. The magnetization of the Al foil was subtracted after the measurement: the magnetization of varnish is very small and negligible compared to that of the sample used in this study.

High-field magnetization measurements were performed by Dr. Atsushi Miyake in the Tokunaga group in the International Mega Gauss Science Laboratory in ISSP. Magnetization was measured by the induction method using a pick-up coil. The pulsed magnetic fields with a duration time of 4 μ s, which were generated by a non-destructive magnet, were used for the measurements. Measurements were performed at 4.2 K and 1.4 K, which are the temperatures of liquid Helium and the gradually pumped liquid Helium by the vacuum pump, respectively. Some measurements were performed at each temperature with changing the maximum value of the pulsed magnetic field up to 74 T. The typical samples for the measurement are shown in fig. 2.2 (a). The powder or single crystal samples were placed in a sample holder made of plastic tube and quartz glass.

2.5 Heat capacity

Heat capacity measurements at 2-300 K in the magnetic field of 0-14 T were performed by the relaxation method in a commercial measurement system (PPMS, Quantum Design) in ISSP. The single crystal or pressed powder sample was used for the measurements.

2.6 Magnetocaloric effect

Magnetocaloric effect measurements of a single crystal of volborthite were performed by Dr. Yoshimitsu Kohama in the Kindo group in the International Mega Gauss Science Laboratory in ISSP. The temperatures of the sample were measured in an adiabatic condition in the pulsed magnetic fields up to 33 T from 2-20 K at zero magnetic field: the sample is shown in the fig. 2.2 (b). To measure the temperature of the sample, the electric resistivity of the Au-Ge alloy sputtered on a surface of the crystal was measured. The resistivity was converted into temperature using the calibration curves of the temperature and magnetic field dependences of the resistivity of the Au-Ge alloy.

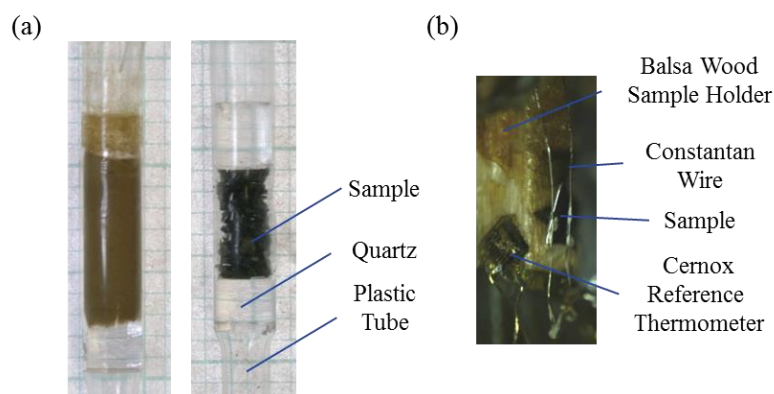


Figure 2.2. (a) Typical samples of high-field magnetization measurements. The powder sample of engelhauptite (left) and the stacked single crystals of volborthite (right). The mesh indicates 1 mm. (b) Sample for the magnetocaloric effect measurement of volborthite.

2.7 Elemental analysis

Elemental analyses were performed by the Inductively Coupled Plasma Atomic Emission Spectroscopy method (ICP-AES, HORIBA JY138KH ULTRACE) in the chemical analysis laboratory in ISSP. The samples were dissolved in the HNO_3 aq. so as to get a solution which contain

approximately 5-15 ppm of each elements. The concentration of the elements in the sample was determined by comparing the intensity of the atomic emission with the calibration curves. Calibration curves were obtained by the measurements of the standard samples with 0, 10, and 20 ppm for the target elements before the sample measurements.

Chapter 3. Crystal structures and structural phase transitions of volborthite

3.1 Brief history and outline

Volborthite $\text{Cu}_3\text{V}_2\text{O}_7(\text{OH})_2 \cdot 2\text{H}_2\text{O}$ is a mineral that has been studied as a frustrated magnet having a distorted kagome lattice [44]. The crystal structure is made of $\text{Cu}_3\text{O}_6(\text{OH})_2$ layers of edge-sharing $\text{CuO}_4(\text{OH})_2$ octahedra, which are separated by V_2O_7 pillars made of VO_4 tetrahedra and H_2O molecules (fig. 3.1(a)). Although these structural features are commonly observed in several studies, different structural models have been proposed at room temperature so far. Basso et al. reported monoclinic structure with the space group $C2/m$ by XRD measurements on a natural single crystal in 1988 [43]. An identical crystal structure was found by Lafontaine et al. by the X-ray and neutron diffraction measurements using a synthetic powder sample [73]. However, Kashaev et al. proposed a different monoclinic structural model with the space group Ia on a natural crystal in 2008 [74]. In 2012, Yoshida et al. synthesized a single crystal of sub-millimeter size (fig. 3.1(b)) and found a first-order structural phase transition at around 310 K from the already known $C2/m$ structure at high temperature to an $I2/a$ structure at low temperature in XRD measurements [75]. The previous discrepancies regarding the crystal structures may be related to the presence of the structural transition near room temperature and the differences in the stoichiometry between natural crystals and synthetic samples.

In order to understand the detailed magnetic properties of volborthite, it is required to get reliable information about the crystal structures and magnetic properties. I have successfully prepared single crystals that appear to have higher quality than crystals used in previous study: the crystals are much larger and highly transparent with crystal faces (fig. 3.1(b)). In the XRD measurement at room temperature, unexpectedly, another crystal structure with the space group $C2/c$ was found. Moreover, a structural transition into $I2/a$ structure was observed below room temperature. Furthermore, another structure with the space group $P2_1/a$ was observed below 150 K. To sum up, the $C2/c$, $I2/a$, $P2_1/a$ structures are observed as lowering the temperature from the room temperature. The details of the crystal structures and phase transitions between them are described and discussed.

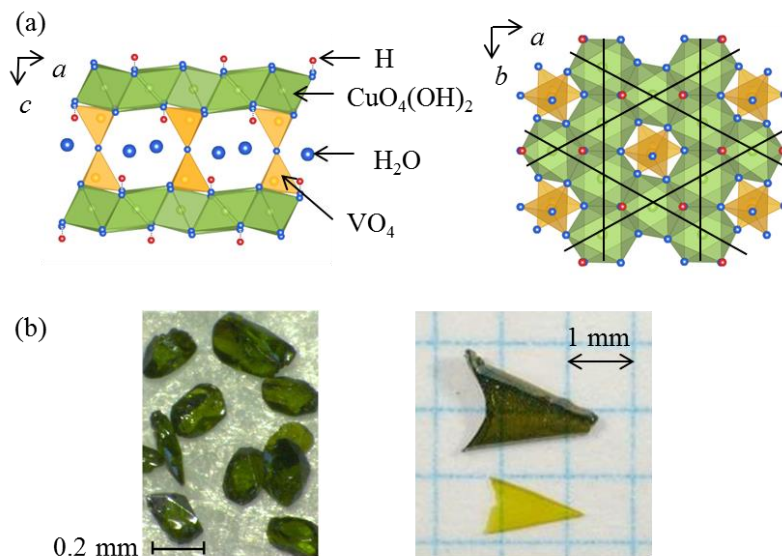


Fig 3.1. (a) Crystal structures of volborthite projected along b (left) and c (right) axis. The layer structure made of CuO_6 octahedra and VO_4 tetrahedra is commonly observed in all of the crystal structures. (b) Crystals of volborthite synthesized in the previous study (left) and this study (right) [75,P1]. The larger green and smaller yellow-green crystals are called thick and thin crystals in this study, respectively. The large triangular plane is the ab -plane and the twin boundary is parallel to the $[110]$ direction.

3.2 Synthesis and elemental analysis

CuO (4N, Raremetallic), V_2O_5 (4N, Raremetallic), $\text{HNO}_3\text{aq.}$ (60wt%, Wako), and pure H_2O were put in a Teflon beaker. 1.3 ml of $\text{HNO}_3\text{aq.}$ was added per 100 ml of H_2O . The typical reaction conditions are summarized in table 2.1. A large reaction vessel was necessary to obtain large crystals probably because the conditions suitable for the crystal growth last longer time in larger beaker. The vessels were heated at $170\text{ }^\circ\text{C}$ for 5-30 days and the crystals of volborthite were found on the solid product composed of polycrystalline volborthite and unreacted starting materials. Large crystals typically have arrowhead shape and become thicker with time duration. The large crystals grown in 15 and 30 days, which were used for the physical properties measurements, are called thin and thick crystals, respectively (fig. 3.1 (b)). As a non-magnetic reference material for the heat capacity measurement of volborthite, powder sample of the $\text{Zn}_3\text{V}_2\text{O}_7(\text{OH})_2 \cdot 2\text{H}_2\text{O}$ [76] was synthesized. ZnO (4N, Kojundo Kagaku) and V_2O_5 (4N, Raremetallic) were mixed in the molar ratio of 3 : 1 with 10

ml of pure H₂O in the Teflon beaker of 45 ml volume and heated at 170°C for 24h. White polycrystalline sample of Zn₃V₂O₇(OH)₂•2H₂O was obtained.

Table 2.1 Typical reaction conditions of the single crystals of volborthite

CuO (g)	V ₂ O ₅ (g)	H ₂ O (ml)	Volume of the Beaker (ml)
0.567	0.432	15	45
4.5	3.0	100	226
6.0	3.0	400	790

The ICP-AES experiment for the bunch of thin crystals indicate that the molar ratio of Cu and V is 3 : 1.99, which is very close to the ideal stoichiometry. Therefore, I performed structural analyses of volborthite assuming an ideal stoichiometry below.

3.3 C2/c structure at room temperature

The crashed thin crystal of the size ~ 0.1 × 0.05 × 0.02 mm is studied by the single crystal x-ray diffractometer in ISSP. The observed reflections at 293 K cannot be indexed in the previously reported C2/m unit cell: the non-integer reflections for the C2/m unit cell are observed. The observed reflections at 293 K are indexed with the monoclinic unit cell with $a = 10.6118(4)$ Å, $b = 5.8708(2)$ Å, $c = 14.4181(6)$ Å, $\beta = 95.029(1)^\circ$ and the extinction rule suggests the space group is C2/c. The C2/c unit cell has a doubled c -axis of the previously reported C2/m structure ($a = 10.657(3)$ Å, $b = 5.887(1)$ Å, $c = 7.228(2)$ Å, and $\beta = 95.035(8)^\circ$ by Yoshida et al. at 323 K) and thus is a 2 c -superstructure (fig. 3.3(a)). The atomic coordination and structural parameters obtained are shown in table 3.1 ($R1 = 0.0271$, $wR2 = 0.0823$, $S = 1.29$).

Table 3.1. Structural parameters of volborthite C2/c structure at 293 K

Atom	x	y	z	U_{iso}	Occ.
Cu1	0	0	0	0.00897(16)	1
Cu21	0.25	0.25	0	0.00880(16)	1
Cu22	0.25	0.25	0.5	0.00950(16)	1
V	0.49666(5)	-0.02378(8)	0.12692(3)	0.00672(15)	1
O1	0	0.4522(6)	0.25	0.0185(7)	1
O2	0.8422(2)	-0.0013(3)	0.05830(16)	0.0085(4)	1
H	0.8395	-0.0091	0.1149	0.01	1
O31	0.0697(2)	0.2435(4)	0.08596(16)	0.0127(5)	1
O32	0.0758(2)	0.2934(4)	0.60120(16)	0.0138(5)	1
O4	0.6584(2)	-0.0054(3)	0.42408(18)	0.0114(5)	1
O5	0.8240(4)	-0.0160(6)	0.2393(2)	0.0439(10)	1

Atom	U_{11}	U_{22}	U_{33}	U_{23}	U_{13}	U_{12}
Cu1	0.0073(3)	0.0089(3)	0.0108(3)	-0.00277(16)	0.0012(2)	-0.00094(16)
Cu21	0.0085(3)	0.0065(3)	0.0109(3)	-0.00039(16)	-0.0023(2)	-0.00074(17)
Cu22	0.0094(3)	0.0065(3)	0.0119(3)	0.00043(17)	-0.0037(2)	-0.00062(17)
V	0.0073(3)	0.0079(2)	0.0049(3)	-0.00033(15)	-0.00041(18)	-0.00035(16)
O1	0.0212(18)	0.0273(17)	0.0071(15)	0	0.0017(13)	0
O2	0.0084(11)	0.0084(10)	0.0085(10)	-0.0001(6)	0.0001(8)	-0.0004(7)
O31	0.0118(11)	0.0134(11)	0.0129(11)	-0.0024(8)	0.0000(9)	0.0006(8)
O32	0.0137(12)	0.0133(10)	0.0138(11)	-0.0011(8)	-0.0013(9)	0.0017(9)
O4	0.0101(11)	0.0107(11)	0.0128(11)	0.0002(7)	-0.0024(9)	-0.0002(7)
O5	0.057(3)	0.060(2)	0.0139(15)	0.0012(12)	-0.0008(15)	0.0010(16)

In the $C2/c$ structure, the similar framework made of CuO_6 octahedra and V_2O_7 pillars are found as in the previously reported $C2/m$ structure. One important difference between the $C2/c$ and $C2/m$ structures is that there are crystallographically three Cu sites (Cu1, Cu21, and Cu22) in the $C2/c$ structure, instead of two (Cu1 and Cu2) in the previously reported $C2/m$ structure. Moreover, the O3 site in the $C2/m$ structure is split into the O31 and O32 sites in the $C2/c$ structure. Details of the structural differences between the $C2/c$ and $C2/m$ structures are discussed later.

3.4 $I2/a$ structure at intermediate temperatures

A structural phase transition is observed around room temperature. Single crystal XRD measurements are performed between 150 and 320 K in the heating process. The reflection data collected at 150 K is indexed with the unit cell of $a = 10.6134(1) \text{ \AA}$, $b = 5.8703(1) \text{ \AA}$, $c = 14.4181(1) \text{ \AA}$, $\beta = 95.022(1)^\circ$, which are similar to those of the $C2/c$ structure. However, reflections with $h + k + l = 2n$ ($n = \text{integer}$) are selectively observed, indicating that the lattice has body center symmetry. The extinction rule suggests that the space group is $I2/a$. It is noted that the $I2/a$ unit cell is another cell setting of the unit cell with the space group $C2/c$ and $a = 17.1387(3) \text{ \AA}$, $b = 5.8703(1) \text{ \AA}$, $c = 10.6134(1) \text{ \AA}$, $\beta = 123.067(2)^\circ$. The $I2/a$ unit cell is chosen to compare it with the room temperature $C2/m$ and $C2/c$ structures. It should also be noted that the space group is unchanged during the phase transition: both structures have the space group $C2/c$. This type of phase transition is known as iso-structural phase transition.

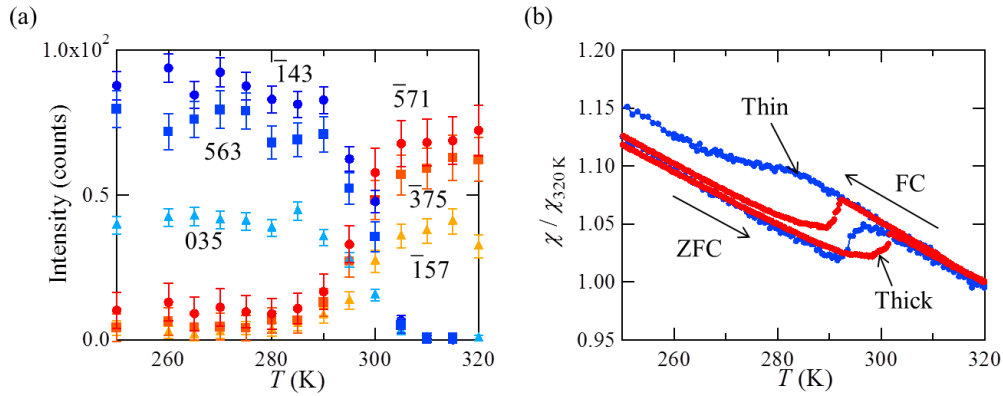


Figure 3.2. (a) Temperature dependence of the intensity of selected reflections at around room temperature. (b) Normalized temperature dependences of the magnetic susceptibility of thin and thick crystals of volborthite at around room temperature.

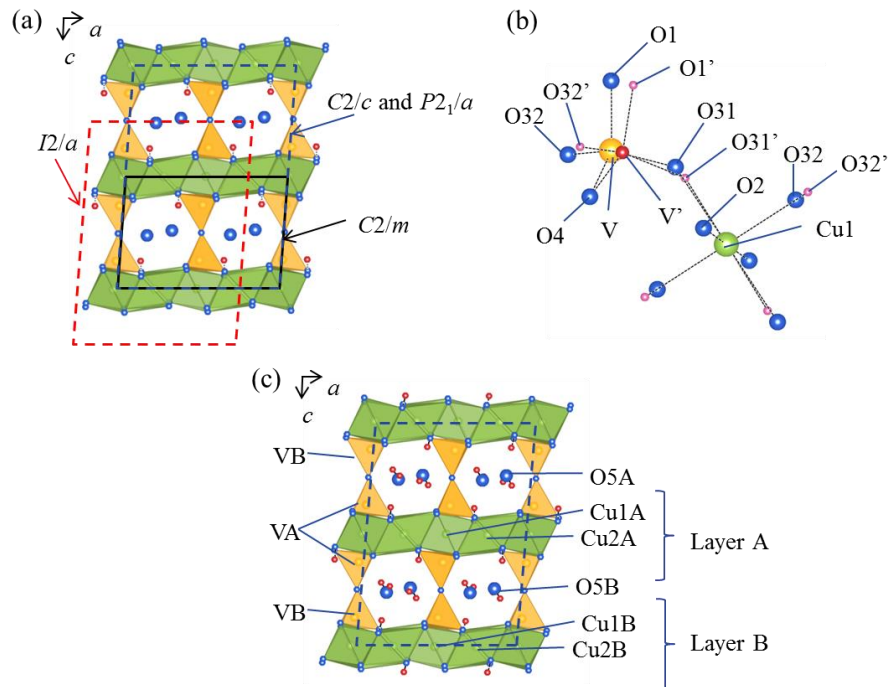


Figure 3.3. (a) The unit cells of the different structures of volborthite. (b) Structural model with the site splitting around the VO_4 tetrahedra for the $I2/a$ structure of the thin crystal of volborthite at 150 K. The site splitting also affects the coordination environment of Cu1 atom. (c) The representative atomic sites of volborthite $P2_1/a$ structure. The layers A and B are identical in the $C2/c$ and $I2/a$ structures.

The intensity of the reflections with $h + k + l = 2n$ ($n = \text{integer}$) decrease upon heating and vanish at around 290 K. Then, some reflections with $h + k = 2n$ appear, which are allowed for the C-centered lattice (fig. 3.2(a)). Thus, a structural transition from the $I2/a$ to $C2/c$ structure occurs. Since the phase-coexistence is observed between 285 and 305 K, the transition is of the first order.

The phase transition is also observed in the magnetic susceptibility measurements; steps are observed at around 290 and 280 K in the heating and cooling processes, respectively (fig. 3.2(b)). This suggests that substantial changes in magnetic interactions are accompanied by the structural transition. The change in the magnetic susceptibility in the cooling process appears broad compared to the heating process.

The structural analysis for the reflection data obtained at 150 K suggests that the crystal structure is identical to the previously reported $I2/a$ structure. In the thin crystal studied in this work, however, structural disorder is found in the V, O31, O32, and O4 sites, which form the VO_4 tetrahedra (fig. 3.3(b)). These atomic sites are refined by splitting them into two sites (for example, V and V') with the total occupancy fixed to 1. The $R1$ is improved from 4.5% to 3.6% by the site splitting model and the occupancies are determined as 0.897(2) and 0.103(2) for the two sites. The result of the refinement is shown in the table 3.2 ($R1 = 0.0355$, $wR2 = 0.0945$, $S = 1.052$). As the disorder in these atomic sites is not found in the room temperature structure, disorder is considered to be caused by the structural phase transition at around room temperature.

The identical $I2/a$ structure is also observed at 200 K in the synchrotron XRD experiments at BL8A in KEK at 200 K for the thick single crystal with the unit cell $a = 10.6237(3) \text{ \AA}$, $b = 5.8468(1) \text{ \AA}$, $c = 14.3892(1) \text{ \AA}$, $\beta = 95.357(1)^\circ$. On the other hand, structural disorder found in the thin crystal is not observed, which may indicate that the sample quality of the thick crystal is better than the thin single crystal. The difference between the crystals is also found in the magnetic susceptibility measurements; the magnetic susceptibility shows more steep kinks in the thick crystal than in the thin crystal (Fig. 3.2 (b)).

Table 3.2. Structural parameters of volborthite $I2/a$ structure at 150 K

Atom	x	y	z	U_{iso}	Occ.
Cu1	0.25	0.25	0.25	0.00446(3)	1
Cu2	-0.00270(2)	0.49585(2)	0.25115(2)	0.00475(3)	1
V	0.24669(2)	0.72633(7)	0.37681(2)	0.00336(4)	0.8969(19)
V'	0.2468(3)	0.7748(5)	0.37726(17)	0.00336(4)	0.1031(19)
O1	0.25	0.7035(3)	0.5	0.0098(2)	0.8969(19)
O1'	0.25	0.800(3)	0.5	0.0098(2)	0.1031(19)
O2	0.09314(9)	0.24746(13)	0.30879(6)	0.00472(11)	1
H1	0.0862	0.2481	0.365	0.006	1
O31	0.32574(12)	-0.0424(2)	0.35109(9)	0.00773(15)	0.8969(19)
O31'	0.3198(11)	0.0076(18)	0.3366(8)	0.00773(15)	0.1031(19)
O32	0.32009(11)	0.49207(18)	0.33662(8)	0.00649(14)	0.8969(19)
O32'	0.3270(10)	0.5389(18)	0.3532(7)	0.00649(14)	0.1031(19)
O4	0.09131(10)	0.74577(14)	0.32509(7)	0.00609(11)	1
O5	0.4280(2)	0.2408(3)	0.51022(11)	0.0270(4)	1

Atom	U_{11}	U_{22}	U_{33}	U_{23}	U_{13}	U_{12}
Cu1	0.00318(7)	0.00441(6)	0.00589(6)	-0.00099(4)	0.00090(6)	-0.00038(4)
Cu2	0.00433(5)	0.00332(5)	0.00630(5)	-0.00026(3)	-0.00125(4)	0.00062(3)
V	0.00320(6)	0.00387(9)	0.00298(5)	-0.00016(6)	0.00009(5)	0.00009(6)
V'	0.00320(6)	0.00387(9)	0.00298(5)	-0.00016(6)	0.00009(5)	0.00009(6)
O1	0.0099(6)	0.0170(6)	0.0025(4)	0	-0.0004(4)	0
O1'	0.0099(6)	0.0170(6)	0.0025(4)	0	-0.0004(4)	0
O2	0.0043(3)	0.0046(2)	0.0052(2)	-0.00023(17)	0.0001(2)	-0.00016(18)
O31	0.0068(3)	0.0069(3)	0.0094(4)	0.0015(3)	0.0002(3)	-0.0017(3)
O31'	0.0068(3)	0.0069(3)	0.0094(4)	0.0015(3)	0.0002(3)	-0.0017(3)
O32	0.0057(3)	0.0066(3)	0.0073(3)	-0.0023(2)	0.0009(3)	0.0002(3)
O32'	0.0057(3)	0.0066(3)	0.0073(3)	-0.0023(2)	0.0009(3)	0.0002(3)
O4	0.0051(3)	0.0058(2)	0.0070(3)	-0.00003(19)	-0.0012(2)	0.0002(2)
O5	0.0308(10)	0.0414(10)	0.0085(4)	0.0007(5)	0.0003(5)	0.0036(7)

3.5 $P2_1/a$ structure at low temperatures below 155 K

The thick crystal is further studied in the laboratory X-ray diffractometer and using synchrotron radiation source at BL8A in KEK at 50-220 K. In the laboratory XRD measurements, the $C2/c$ structure, which is identical to that found in the thin crystal, is observed at room temperature.

Figure 3.4(a) shows the temperature dependence of the selected reflections at around 150 K. Some reflections with $h + k + l = 2n + 1$ appear below 155 K, which indicates that the body center symmetry is lost. In contrast to the phase transition at around room temperature, magnetic susceptibility do not show clear anomaly at around 155 K (fig. 3.4(b)). On the other hand, a peak is observed at 155 K in the heat capacity measurement, which clearly indicates the presence of the phase transition.

The reflection data obtained at 50 K are indexed with the unit cell of $a = 10.6489(1) \text{ \AA}$, $b = 5.8415(1) \text{ \AA}$, $c = 14.4100(1) \text{ \AA}$, $\beta = 95.586(1)^\circ$ (fig. 3.3(c)) and the space group is determined to be $P2_1/a$ from the extinction rule; the unit cell can also be taken as $a = 17.0638(2) \text{ \AA}$, $b = 5.8415(1) \text{ \AA}$, $c = 10.6489(2) \text{ \AA}$, $\beta = 122.811(1)^\circ$ with the normally used space group $P2_1/c$. The result of the structural refinement is shown in the table 3.3 ($R1 = 0.0297$, $wR2 = 0.1002$, $S = 1.117$). The ratio of average intensity of the reflections with $h + k + l = 2n$ to those with $h + k + l = 2n + 1$ is 117 to 1, which indicates the structural change caused by the phase transition is very small. Actually, the test refinements with the $I2/a$ structural model give similar R -values to that with the $P2_1/a$ model. The phase transition is not observed in the measurement of the thin crystal at 150 K partly due to the small structural change and that the measurement temperature is too close to the transition temperature.

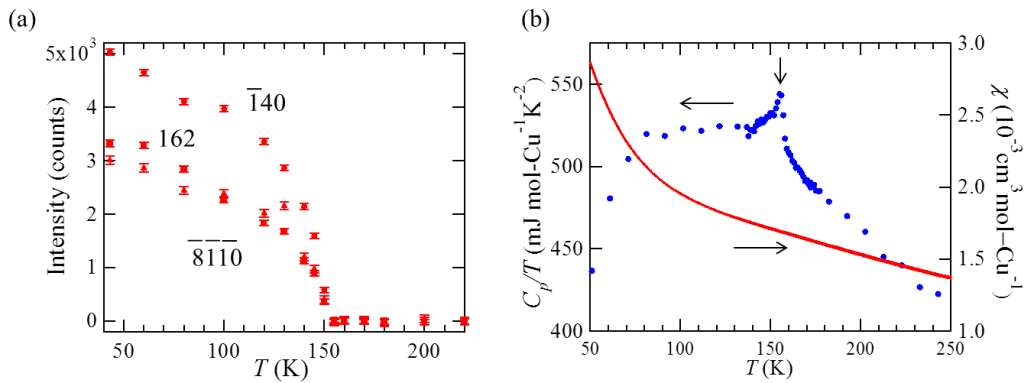


Figure 3.4. (a) Temperature dependences of the selected reflections of the thick single crystals of volborthite. (b) Temperature dependences of the magnetic susceptibility and the heat capacity of the thick crystals of volborthite.

In the $P2_1/a$ structure, there are crystallographically two kinds of kagome layers (layers A and B), VO_4 tetrahedra, and H_2O molecules (fig. 3.3(c)). Atoms attached to the layers A and B are named as “atom A” and “atom B”, respectively: for example, VA is the V atom attached to the layer A and O5A, which is the O atom of the H_2O molecule, is connected to the layer A via hydrogen bonding as discussed below. It is noted that the structural differences between the two layers are very small.

Table 3.3 Structural parameters of volborthite $P2_1/a$ structure at 50 K

Atom	x	y	z	U_{iso}	Occ.
Cu1A	0	0	0.5	0.00221(5)	1
Cu1B	0	0	0	0.00225(5)	1
Cu2A	0.25374(2)	-0.24401(3)	0.49768(2)	0.00236(4)	1
Cu2B	-0.25280(2)	-0.24624(3)	0.00070(2)	0.00256(4)	1
VA	0.00333(2)	-0.47670(4)	0.37340(2)	0.00305(4)	1
VB	-0.00304(2)	-0.47868(4)	0.12703(2)	0.00306(4)	1
O1	-0.00160(11)	-0.4512(2)	0.25006(7)	0.00806(15)	1
O2A	0.15624(10)	0.00431(15)	0.44064(7)	0.00329(15)	1
H1A	0.1499	-0.011	0.3838	0.004	1
O2B	-0.15637(10)	0.00097(15)	0.05898(7)	0.00327(15)	1
H1B	-0.168	0.0069	0.1144	0.004	1
O31A	-0.07520(9)	-0.7060(2)	0.40086(7)	0.00653(15)	1
O31B	0.07587(9)	-0.71304(19)	0.10276(7)	0.00609(14)	1
O32A	-0.07123(9)	-0.23820(18)	0.41152(7)	0.00566(15)	1
O32B	0.07063(9)	-0.24608(18)	0.08562(7)	0.00566(15)	1
O4A	0.15834(10)	-0.49422(16)	0.42560(8)	0.00413(15)	1
O4B	-0.15841(11)	-0.49475(16)	0.07478(8)	0.00432(15)	1
O5A	-0.17875(14)	-0.0023(2)	0.23925(9)	0.0098(2)	1
H2A1	-0.141(3)	-0.070(5)	0.2834(16)	0.012	1
H2A2	-0.194(3)	0.115(4)	0.2664(18)	0.012	1
O5B	0.18062(14)	0.0333(3)	0.25914(8)	0.0130(2)	1
H2B1	0.140(3)	0.101(5)	0.2150(17)	0.016	1
H2B2	0.185(3)	-0.105(3)	0.243(2)	0.016	1

Atom	U_{11}	U_{22}	U_{33}	U_{23}	U_{13}	U_{12}
Cu1A	0.00225(8)	0.00175(10)	0.00264(8)	-0.00057(5)	0.00038(6)	-0.00035(5)
Cu1B	0.00218(8)	0.00195(10)	0.00265(8)	0.00054(5)	0.00039(6)	0.00024(5)
Cu2A	0.00297(6)	0.00095(8)	0.00291(6)	-0.00032(4)	-0.00088(4)	0.00042(4)
Cu2B	0.00305(6)	0.00164(8)	0.00279(6)	-0.00007(4)	-0.00084(4)	-0.00039(4)
VA	0.00255(8)	0.00514(10)	0.00143(7)	0.00001(5)	0.00003(5)	-0.00005(5)
VB	0.00266(8)	0.00505(10)	0.00141(7)	0.00012(5)	-0.00001(5)	-0.00021(5)
O1	0.0095(3)	0.0108(5)	0.0037(3)	-0.0004(3)	0.0003(2)	0.0003(4)
O2A	0.0036(3)	0.0035(4)	0.0027(3)	0.0001(2)	0.0002(3)	0.0000(2)
O2B	0.0032(3)	0.0033(4)	0.0033(3)	0.0001(2)	0.0002(3)	-0.0001(2)
O31A	0.0066(3)	0.0066(4)	0.0064(3)	-0.0005(3)	0.0007(3)	-0.0024(3)
O31B	0.0060(3)	0.0060(4)	0.0062(3)	0.0003(3)	0.0005(2)	0.0005(3)
O32A	0.0057(3)	0.0060(4)	0.0052(3)	0.0002(3)	0.0001(2)	0.0004(3)
O32B	0.0056(3)	0.0055(4)	0.0059(3)	-0.0006(3)	0.0007(2)	-0.0014(3)
O4A	0.0032(3)	0.0043(4)	0.0047(3)	-0.0001(2)	-0.0008(3)	0.0002(2)
O4B	0.0041(3)	0.0043(4)	0.0043(3)	0.0000(2)	-0.0008(3)	-0.0001(2)
O5A	0.0133(5)	0.0105(5)	0.0053(4)	-0.0009(3)	-0.0007(3)	0.0049(3)
O5B	0.0146(5)	0.0195(6)	0.0049(4)	-0.0001(4)	0.0004(3)	0.0024(4)

3.6 Discussion

3.6.1 Jahn-Teller distortion of CuO_6 octahedra and tilting of V_2O_7 pillars

The different crystal structures of volborthite are mainly distinguished by the way of Jahn-Teller distortion of CuO_6 octahedra and tilting of V_2O_7 pillars. First, I focus on the Jahn-Teller distortion of CuO_6 octahedra, which determines the type of orbital occupied by the unpaired electron and its direction in the kagome lattice. All of the CuO_6 octahedra in the $C2/c$, $I2/a$, and $P2_1/a$ structures are elongated along one axis ($[4 + 2]$ coordination). Therefore, the $d_{x^2-y^2}$ -type orbital is selected in all the Cu sites. On the other hand, there are both elongated ($[4 + 2]$ coordination) and squeezed ($[2 + 4]$ coordination) octahedra in the previously reported $C2/m$ structure; there are both $d_{x^2-y^2}$ -type and d_{z^2} -type orbitals. The Cu-O distances in the different structures are summarized in the table 3.4.

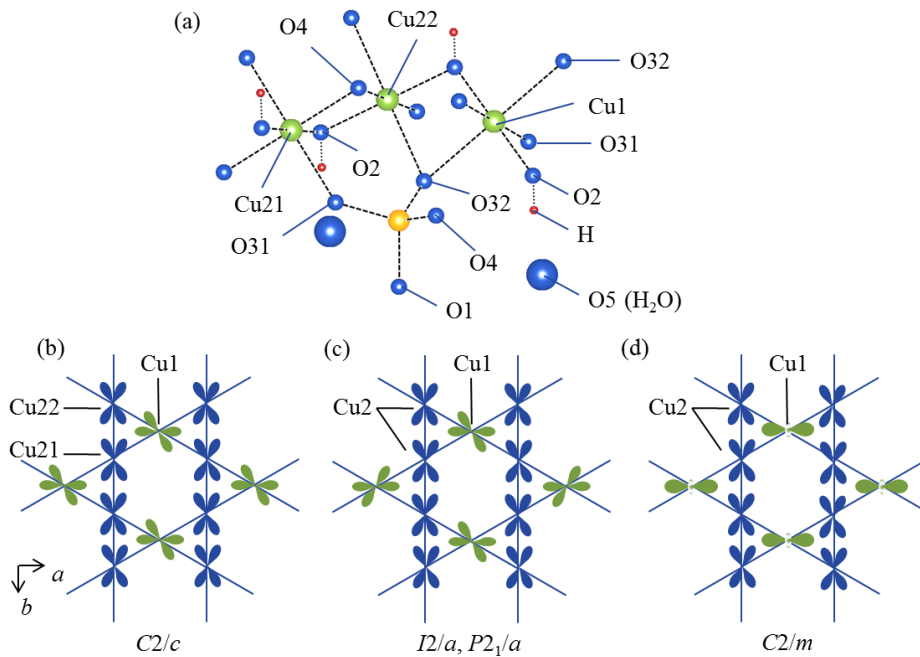


Figure 3.5. (a) Coordination environment of Cu and V atoms of volborthite $C2/c$ structure. The Cu21 and Cu22 sites are crystallographically identical (Cu2) in other crystal structures. The O31 and O32 sites are also crystallographically identical (O3) in the $C2/m$ structure. The orbitals patterns in the kagome lattice of (a) $C2/c$ (b) $I2/a$ and $P2_1/a$ (c) $C2/m$ structures of volborthite projected onto the ab plane.

Table 3.4. The Cu-O distances in different structures of volborthite

<i>C2/c</i> Structure at 293 K (thin crystal)		<i>C2/m</i> Structure at 323 K (Yoshida, 2012)	
Bond	Bond Length (Å)	Bond	Bond Length (Å)
Cu1-O2	1.938(2) ×2	Cu1-O2	1.947(2) ×2
Cu1-O31	1.991(2) ×2	Cu1-O3	2.181(2) ×4
Cu1-O32	2.353(2) ×2	Cu2-O2	1.923(1) ×2
Cu2-O2	1.911(2) ×2	Cu2-O4	2.036(1) ×2
Cu2-O4	2.050(2) ×2	Cu2-O3	2.422(1) ×2
Cu2-O31	2.370(2) ×2		
Cu3-O2	1.923(2) ×2		
Cu3-O4	2.005(2) ×2		
Cu3-O32	2.467(3) ×2		

<i>I2/a</i> Structure at 150 K (thin crystal)		<i>P2₁/a</i> Structure at 50 K (thick crystal)	
Bond	Bond Length (Å)	Bond	Bond Length (Å)
Cu1-O2	1.9332(9) ×2	Cu1A-O2A	1.9435(11) ×2
Cu1-O32	1.992(1) ×2	Cu1A-O32A	1.9871(10) ×2
Cu1-O31	2.348(1) ×2	Cu1A-O31A	2.3260(11) ×2
Cu2-O2	1.9244(9)	Cu1B-O2B	1.9418(11) ×2
Cu2-O2	1.9247(9)	Cu1B-O32B	1.9934(10) ×2
Cu2-O4	2.0116(9)	Cu1B-O31B	2.3287(11) ×2
Cu2-O4	2.024(1)	Cu2A-O2A	1.9213(10)
Cu2-O31	2.338(1)	Cu2A-O2A	1.9248(10)
Cu2-O32	2.502(1)	Cu2A-O4A	2.0066(10)
		Cu2A-O4A	2.0104(10)
		Cu2A-O32A	2.3403(10)
		Cu2A-O31A	2.5256(10)
		Cu2B-O2B	1.9176(10)
		Cu2B-O2B	1.9219(10)
		Cu2B-O4B	2.0088(10)
		Cu2B-O4B	2.0121(10)
		Cu2B-O32B	2.3415(10)
		Cu2B-O31B	2.5251(10)

Comparing the orbital arrangements in the different structures is useful to consider the effect of phase transitions on magnetic properties as they determine the pattern of magnetic interactions. The orbital patterns in different structures of volborthite are shown in figs. 3.5(b-d). They have chains made of $d_{x^2-y^2}$ -type orbital along the b -axis in common and their main difference is the type and arrangement of the orbital which reside between the chains. In the room temperature *C2/c* structure found in this study, the $d_{x^2-y^2}$ -type orbital is selected and arranged with the same direction. In previously reported room temperature *C2/m* structure, $d_{3z^2-r^2}$ -type orbital is selected and arranged in

the same direction. In the low temperature $I2/a$ and $P2_1/a$ structures, $d_{x^2-y^2}$ -type orbital is selected and arranged in the staggered way. The phase transition between $C2/c$ and $I2/a$ structures may be called “orbital flipping” transition to distinguish it from the reported “orbital switching” transition between $C2/m$ and $I2/a$ structures [75]; the orbital change from $d_{3z^2-r^2}$ -type to $d_{x^2-y^2}$ -type in the orbital switching transition, while the type of the orbital is unchanged and only its direction is changed in the orbital flipping transition. In the phase transition at 155 K, the orbital pattern is unchanged.

V_2O_7 pillars, which separate kagome layers, also show unique structural changes at the structural phase transitions as they share some O atoms with the CuO_6 octahedra. They tilt along b -axis in the same direction within a layer in the $C2/c$ structure (fig. 3.6(a)). The angle made by V atoms and the bridging O1 atom ($\angle V-O1-V$) is 171° at 293 K. They tilt in the opposite direction in the next layer. In the $I2/a$ structure, they tilt in the staggered directions along b -axis within a layer with $\angle V-O1-V = 171^\circ$ at 200 K. The tilting is almost unchanged in the $P2_1/a$ structure. On the other hand, the tilting is absent in the $C2/m$ structure: $\angle V-O1-V = 180^\circ$.

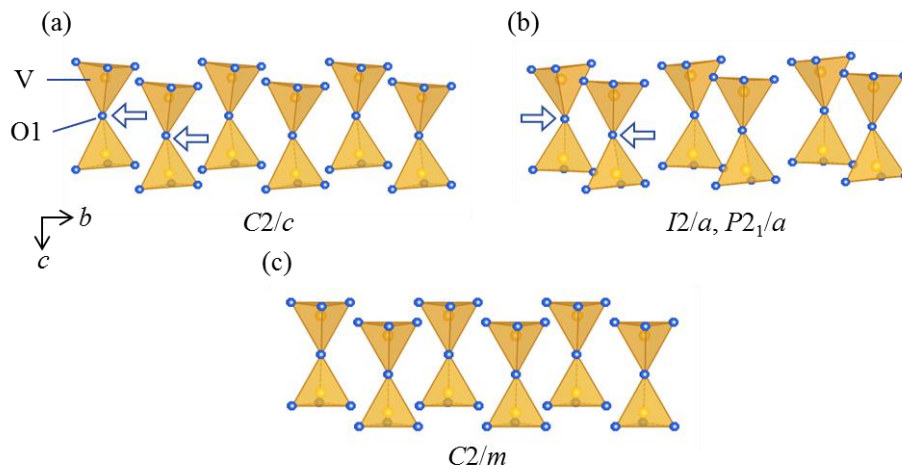


Figure 3.6. The tilting of the V_2O_7 pillars in (a) $C2/c$ (b) $I2/a$ (c) $C2/m$ structures seen from the a -axis.

3.6.2 Relationship between room temperature $C2/c$ and $C2/m$ structures

Here, I consider the relationship between the $C2/c$ and $C2/m$ structures at room temperature. The selection of $d_{3z^2-r^2}$ -type orbital ($[2 + 4]$ coordination), which is found in the $Cu2$ site in the $C2/m$ structure, is relatively rare in copper oxides. One possible interpretation of the $C2/m$ structure is to assume a static or dynamical averaging effect of the Jahn-Teller distortion. The structural changes

between the $C2/c$ and $I2/a$ structures suggest that the two types of $[4 + 2]$ coordination are possible at the Cu2 site. When the two orthogonal $[4 + 2]$ coordination are randomly distributed, the $[2 + 4]$ coordination of the Cu2 site of the $C2/m$ structure must be observed as an average structure (fig. 3.7). Similarly, the absence of the tilting of V_2O_7 pillar in the $C2/m$ structure can be explained by the disorder in the directions of tilting. In fact, the thermal ellipsoids of O1 and O3 atoms, which determine the direction of the Jahn-Teller distortion of Cu_1O_6 octahedra and the tilting of the V_2O_7 pillars, are significantly larger than those of other ions in the $C2/m$ structure, suggesting the presence of structural disorder. Therefore, I consider the $C2/m$ structure is a disordered structure of with randomness in the O1 and O3 sites.

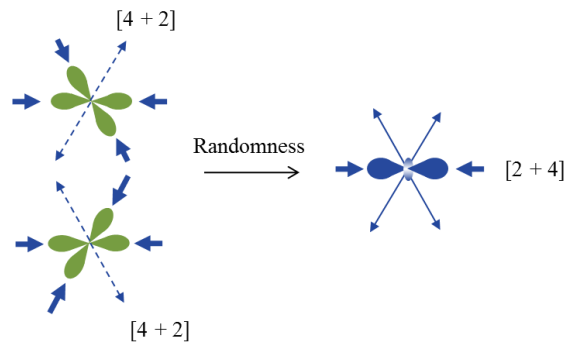


Figure 3.7. Schematic picture of the origin of the apparent $[2 + 4]$ coordination of the CuO_6 octahedra in the $C2/m$ structure of volborthite.

Possible origin to produce the two room-temperature structures is the difference in synthetic condition. The powder and single crystal samples with the $C2/m$ structure are synthesized by the precipitation method from the aqueous solution at $90\text{ }^\circ\text{C}$ and slow-cooling method from $180\text{ }^\circ\text{C}$ to $130\text{ }^\circ\text{C}$ in the hydrothermal condition, respectively. In these synthetic conditions, chemical reaction or crystal growth may occur in relatively short time when the pH and temperature of the solution pass through the appropriate conditions. On the other hand, the single crystal with $C2/c$ structure is grown at constant temperature of $170\text{ }^\circ\text{C}$ and in much longer reaction time. In this synthetic condition, the crystals with the most thermodynamically stable structure at the temperature must be generated with smaller disorder.

The disorder of approximately 10% for the O1, O31, O32 and V sites is also found in the low temperature $I2/a$ structure of the thin crystal but not in the thick crystal. Note that structural disorder was not observed in the thin crystals at room temperature before the orbital flipping transition. Thus,

the disorder is generated during the orbital flipping transition only in the thin crystal. The two types of crystals are synthesized in the same condition except for reaction time: 15 and 30 days for the thin and thick crystals, respectively. There is no distinguishable structural difference between them at room temperature. There might be a small difference that cannot be detected in present XRD experiments such as the disorder of the position of hydrogen atoms. Such a weak disorder may be reduced in the thick crystal during long crystal growth time. Even though the disorder is weak, it can affect the orbital flipping transition, resulting in the disorder of the thin crystal at low temperatures. In fact, the magnetic susceptibilities of fig. 3.2(b) show a smaller and more extended decrease upon cooling at the transition for the thin crystals compared with the thick crystals.

3.6.3 Structural changes around H₂O molecules

Finally, I discuss the role of H₂O molecule between the kagome layers in the phase transitions. In the previously reported *C2/m* structure determined by the powder neutron diffraction experiments, the hydrogen atoms of H₂O molecule are located in the direction of O3 atoms coordinated to the Cu1 atom. Figures 3.8(a) and (b) show the coordination environment of a Cu1O₆ octahedra in the *C2/c* and *I2/a* structures before and after the orbital flipping transition. The axial and equatorial O atoms in the elongated CuO₆ octahedra are shown as the red and blue spheres, respectively. For these structures, the positions of the H atom have not yet been determined by the XRD analysis. Thus, we estimate the presence of the hydrogen bonding from the O-O distances. The distances between O5 atoms of H₂O molecules and O3 atoms are approximately 3 Å: there should be a hydrogen bonding between them. In both of the structures, the distance between O5 and axial O atom is shorter than that for the equatorial O atom; it seems that the axial O atoms are attracted by H₂O molecules via hydrogen bonding. This may indicate that the H₂O molecule change their orientation cooperatively with the orbital flipping transition. In the *C2/m* structure, the two equatorial O atoms appear to be equally attracted.

Although the scattering factor of H atom is smaller than those of Cu, V, and O atoms, a small residual electron density is found around the O5 atom in the refinement of the data obtained in synchrotron XRD experiment at 50 K in the *P2₁/a* structure. The hydrogen atoms, which are refined using the constraint on the O5-H distances, are located in the direction of O31 and O32 atoms (fig. 3.9). There are crystallographically two kinds of kagome layers and H₂O molecules in the *P2₁/a* structure, which are identical in the *I2/a* structure. In the layer B, the axial O31B atom of Cu1 octahedra is closer to the O5B atom (O5B-O31B: 2.834(2) Å) than equatorial O32B atom

(O32B-O5B: 3.117(2) Å) as observed in the $I2/a$ structure (fig. 3.9). In the layer A, however, the relationship is reversed; the equatorial O32A atom is slightly closer to the O5A atom (O32A-O5A = 2.970(2) Å) than the axial O31A atom (O5A-O31A = 3.022(2) Å). It is again noted that the way of the Jahn-Teller distortion of Cu1O_6 octahedra and the tilting of V_2O_7 pillars are almost identical between the two layers. It appears that only the arrangement of the H_2O molecules around the layer A has changed in the structural phase transition at 155 K without affecting the crystal structure around them. To discuss about the origin of peculiar structural phase transitions at 155 K, precise hydrogen position must be determined in different temperatures by other experiments such as neutron diffraction experiments on deuterated single crystal samples.

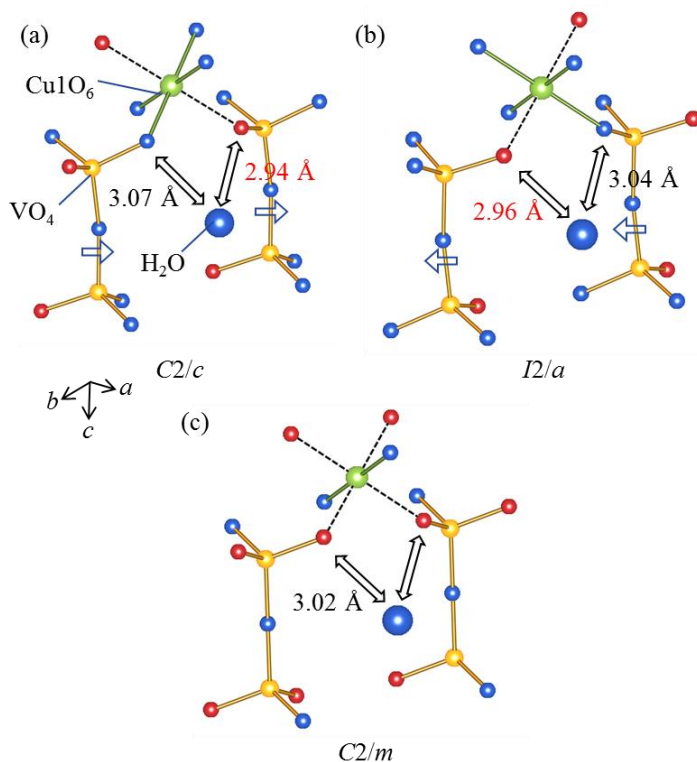


Figure 3.8. The coordination environment around the Cu1 atoms in the (a) $C2/c$ (b) $I2/a$ (c) $C2/m$ structures. The distance between O5 atoms of H_2O molecule and some O atoms coordinated to the Cu1 atoms are shown. The axial and equatorial O atoms in the octahedra are shown as red and blue spheres, respectively.

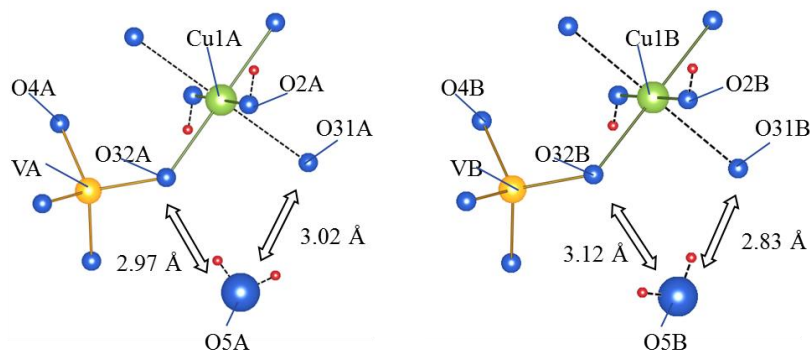


Figure 3.9. Coordination environments around the Cu1 and V atoms and H₂O molecule in the $P2_1/a$ structure of volborthite at 50 K. The bond length between O5 atoms, which are the O atom of the H₂O molecules, and O31 and O32 atoms are shown. The position of hydrogen atoms refined using the constraints on the O5-H distances are shown as the small red spheres.

3.7 Summary

- The large and high-quality single crystals of volborthite are successfully obtained.
- Novel crystal structures of the volborthite with the space group $C2/c$ at room temperature and $P2_1/a$ below 155 K are found in the single crystal XRD measurements. The reported $I2/a$ structure is observed in the intermediate temperature.
- The first order transition where the directions of the $d_{x^2-y^2}$ -type orbital change (orbital flipping transition) is found at around room temperature.
- The $C2/m$ structure is likely a disordered structure, where the directions of $d_{x^2-y^2}$ -type orbitals of Cu1 site and the tilting of the V₂O₇ pillar are randomly distributed.
- The H₂O molecule may play an important role via hydrogen bonding in the structural phase transitions of volborthite. Determining of the position of the hydrogen atoms at different temperatures is necessary to clarify the origin of the structural phase transition.

Chapter 4. Physical properties and high-field magnetic phase transitions of volborthite

4.1 Brief history and outline

Previous studies have shown that volborthite is a strongly frustrated magnet with peculiar magnetic properties, while they are little understood. Magnetic transitions are observed at around 1 K in the heat capacity and NMR measurements on powder samples, which is much lower than the antiferromagnetic Weiss temperature of -115 K (fig. 4.1 (a), [44]). Unusually slow spin fluctuations and low energy excitations, of which origins are still unclear, are observed in the NMR experiments below 1 K in the low field phase called phase I [77].

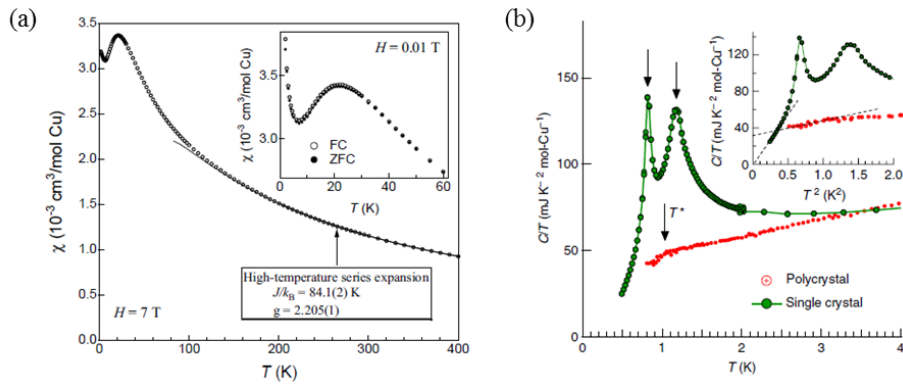


Figure 4.1. (a) Temperature dependence of the magnetic susceptibility of the powder sample of volborthite [44]. (b) Temperature dependence of the heat capacity of powder and single crystal samples of volborthite [75].

Moreover, successive magnetic field induced phase transitions are observed (fig. 4.2). Stepwise increases in magnetization curve called “magnetization steps” are observed at 4.5, 26 and 45 T, above which phases II, III, and IV appear, respectively [78]. The magnetic transitions at the first and second magnetization steps are also detected by NMR measurements [79-80]. At higher magnetic fields above 60 T, a magnetization plateau-like saturation behavior is observed at around $2/5$ of the full magnetization [81] instead of the $1/3$ plateau expected for a kagome lattice. An appropriate spin model which can explain the complex magnetization curve is still unclear.

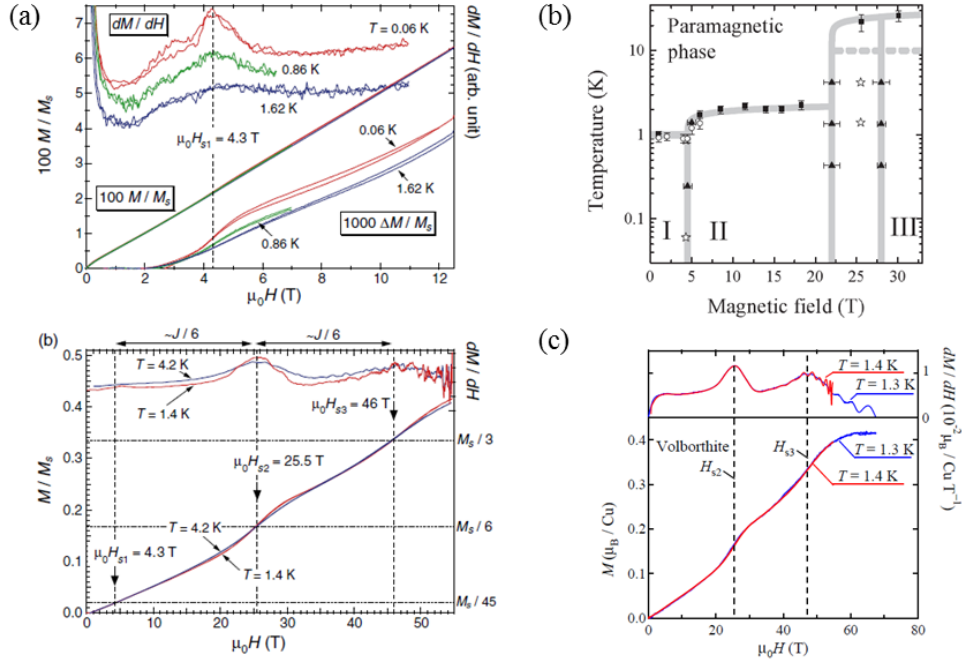


Figure 4.2. (a) Magnetization curves of the powder sample of volborthite up to 55 T [78]. (b) H - T phase diagram of volborthite determined by the magnetization and NMR experiments. The phases II and III are considered to coexist at around 25 T at low temperatures [77]. (c) High-field magnetization curves of volborthite powder sample up to 68 T [81].

It should be noted that the intrinsic magnetic properties of volborthite have been clarified as the sample quality is improved. First, a magnetic order of an inhomogeneous character was found below 1 K in the NMR measurements using low-quality powder samples [82]. Later, a magnetic order at 1 K was evidenced in high-quality powder samples in the NMR measurements [77], which turned out to be a double transition at 0.8 and 1.2 K in the heat capacity measurements of small single crystal sample [75]. This may demonstrate how the frustrated magnet is susceptible to a certain disorder in the sample.

In order to clarify the high-field magnetic phases of volborthite, magnetization measurements up to 74 T were performed using the single crystal samples. Surprisingly, the magnetization curves of the single crystal samples are quite different from that of the powder sample. We have observed the large $1/3$ plateau above 30 T and the novel magnetic phase between 23 and 26 T, which are demonstrated in the magnetocaloric effect and NMR measurements. The origin of the phase transitions and spin models are discussed. Moreover, the realization of the spin nematic phase at

23-26 T is proposed. Before the result of high-field experiments, basic magnetic properties studied at low fields by magnetization and heat capacity measurements are stated.

4.2 Basic physical properties at low magnetic fields

Figure 4.3(a) shows the temperature dependence of the magnetic susceptibility measured in the three different magnetic field directions: $H // a$, $H // b$, and $H \perp ab$. They show similar temperature dependences, indicating that volborthite is an isotropic spin system. The Curie-Weiss fitting with $\chi = \chi_0 + C/(T + \Theta)$ using the common χ_0 and Θ for the high-temperature $C2/c$ phase at 320-300 K results $\Theta = 90(9)$ K, $\chi_0 = 6(3) \times 10^{-5} \text{ cm}^3 \text{ mol-Cu}^{-1}$, and $C = 0.475(20)$, $0.428(20)$, and $0.474(20) \text{ cm}^3 \text{ K mol-Cu}^{-1}$ in $H // a$, $H // b$, and $H \perp ab$, respectively. Assuming $S = 1/2$, g -values are estimated as 2.25(5), 2.14(5), and 2.25(5) in $H // a$, $H // b$, and $H \perp ab$, respectively. Similar fitting for the intermediate $I2/a$ phase at 290-270 K results the $\Theta = 139(9)$ K, $\chi_0 = 1.6(3) \times 10^{-4} \text{ cm}^3 \text{ mol-Cu}^{-1}$ and $C = 0.475(20)$, $0.418(20)$, and $0.469(20) \text{ cm}^3 \text{ K mol-Cu}^{-1}$ in $H // a$, $H // b$, and $H \perp ab$, respectively. Similarly, g -values are estimates as 2.25(5), 2.11(5), and 2.24(5) in the $H // a$, $H // b$, and $H \perp ab$, respectively. The large Weiss temperatures indicate that the antiferromagnetic interaction is dominant for both of the crystal structures. The relatively large uncertainties in the results of the fittings are caused by the narrow fitting ranges. However, an enlarged fitting range for the low temperature $I2/a$ phase gives poor fitting probably because the temperature range is not sufficiently high compared to the magnitude of magnetic interactions.

The g -values can roughly be estimated from the crystal structure by taking into account the orbital arrangements. The electron spin resonance experiments on a polycrystalline sample of volborthite suggest axially symmetric g -values with $g_{//} = 2.40$ and $g_{\perp} = 2.04$ [83]. Assuming these values and taking into account that the $d_{x^2-y^2}$ orbitals tilt approximately 50° from the ab plane, the g -value for $H \perp ab$ is estimated to be 2.20. Similarly, the g -values are estimated to be 2.21 and 2.13 for $H // a$ and b , respectively. These values are consistent with the values obtained from the Curie-Weiss fitting.

A broad peak at around 18 K, which indicates the development of the short range antiferromagnetic correlation, is observed in all the field directions. At lower temperature, small anisotropy is observed in the low magnetic field region. The magnetic susceptibility shows small upturn below 5 K in $H // b$, which is not observed in $H // a$ and $H \perp ab$ (fig. 4.3(b-d)). Above 5 T, the anisotropy vanishes and the upturn is observed in all of the field direction. This anisotropy at low fields may be caused by the DM interaction.

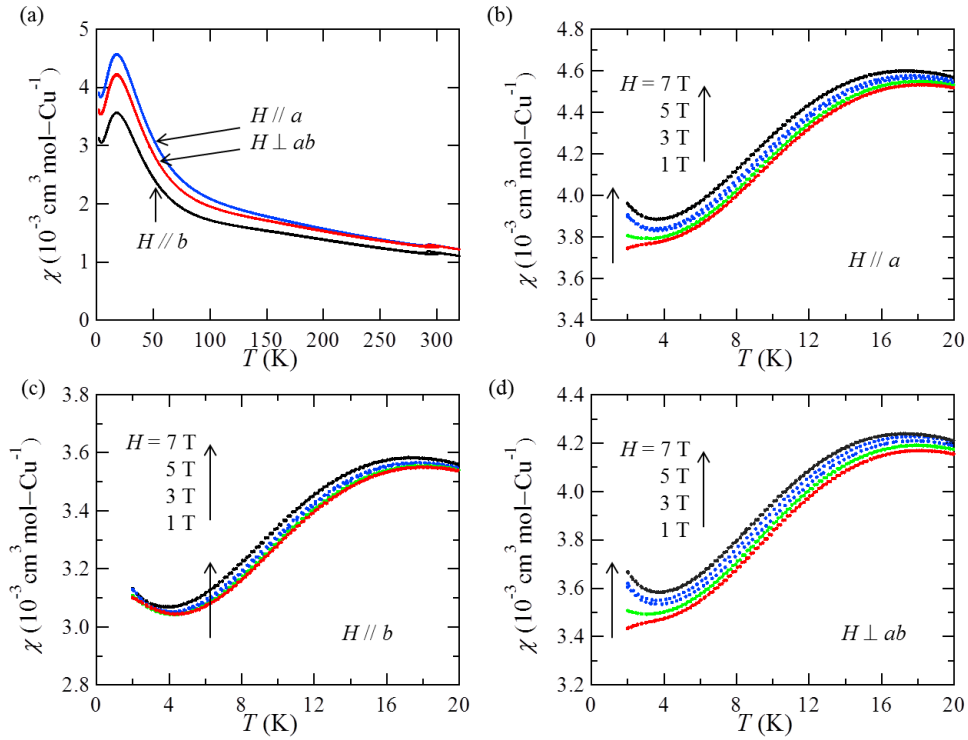


Figure 4.3. (a) Temperature dependences of the magnetic susceptibility of volborthite thick single crystals between 1.8 and 320 K in the field of $H = 5$ T. Magnetic susceptibility between 1.8 and 20 K in different magnetic fields in (b) $H // a$, (c) $H // b$, and (d) $H \perp ab$.

The heat capacity measured for the single crystals of volborthite and the powder sample of $\text{Zn}_3\text{V}_2\text{O}_7(\text{OH})_2 \cdot 2\text{H}_2\text{O}$ are shown in fig. 4.4(a) and (b). The broad shoulder below 20 K, which is absent in the nonmagnetic Zn-compound should be attributed to the release of magnetic entropy with antiferromagnetic short range correlation. The heat capacity of the nonmagnetic Zn-compound is larger than that of volborthite around 20-50 K, therefore, it is not directly used to estimate the lattice heat capacity of volborthite. Tentatively, the temperature axis of the Zn-compound is enlarged by the factor of 1.08 assuming the difference of the Debye- and Einstein- temperatures and used to estimate the lattice heat capacity (blue line in the fig. 4.4(b)). Thus estimated magnetic entropy below 30 K is $0.94 \text{ J mol-Cu}^{-1} \text{ K}^{-1}$, which is approximately 1/6 of the $R \ln 2 = 5.76 \text{ J mol}^{-1} \text{ K}^{-1}$ ($R = 8.31 \text{ J mol}^{-1} \text{ K}^{-1}$) expected for the spin 1/2 system. This indicates that large part of the magnetic entropy is already released at higher temperatures as often observed in the frustrated magnets.

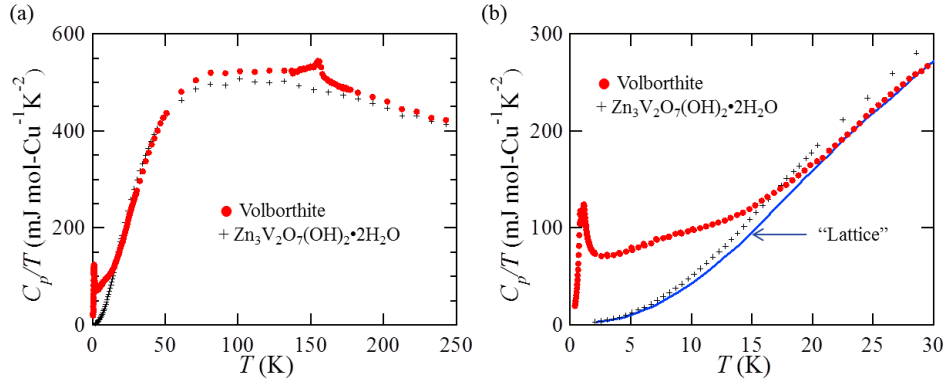


Figure 4.4. Temperature dependences of the heat capacity of volborthite single crystal and the powder sample of $\text{Zn}_3\text{V}_2\text{O}_7(\text{OH})_2 \cdot 2\text{H}_2\text{O}$ at (a) 0.5-250 K and (b) 0.5-30 K.

Heat capacity measurements in magnetic fields are performed below 2 K in the magnetic field $H // [110]$, which is parallel to the twin boundary of the crystal, and $H \perp ab$ (fig. 4.5). At zero field, double peaks at 1.2 and 0.8 K, which indicate the phase transition, are observed. This is consistent with the previous single crystal results and the magnetic order around 1 K observed in the powder sample. In the unpublished NMR measurement for the single crystal sample performed by Yoshida, an increase of the width of the spectra occur around 1 K and a shoulder and a peak are observed in the nuclear spin-lattice relaxation rate $1/T_1$ at 1.2 and 0.8 K, respectively. I call the phase below 0.8 K as phase I and the phase between the peaks as phase I'.

The magnetic field dependences of the heat capacity are similar in the two magnetic field directions. As the magnetic field increases, the two peaks appear to merge, indicating the temperature region of phase I' is decreased. Another broad peak, which must be attributed to the magnetic transition into the phase II, is observed at higher fields above 4 T in $H // [110]$ and 4.5 T in $H \perp ab$. At 3 T in $H // [110]$ and 4 T in $H \perp ab$, both of the merged peak and the broad peak are observed, which may indicate the phase boundaries between phases I and II exist near the magnetic fields. At higher fields, the broad peaks shift to higher temperature; the peak temperature is enhanced up to 1.8 K at 9 T in $H // [110]$ and 1.9 K at 9 T in $H \perp ab$.

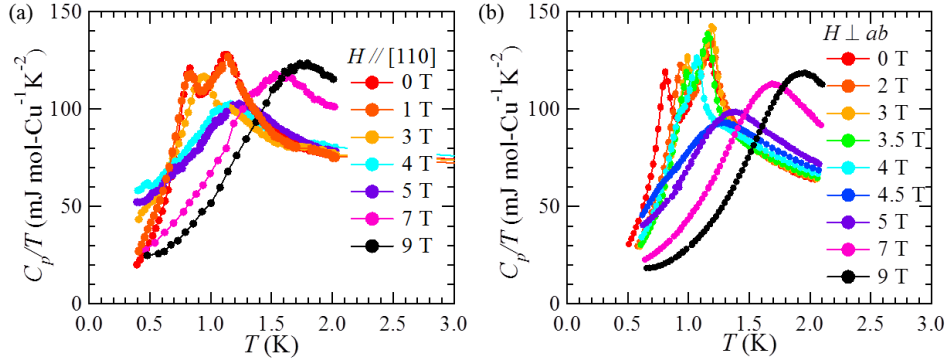


Figure 4.5. Magnetic field dependences of the heat capacity of volborthite in (a) $H // [110]$ and (b) $H \perp ab$.

4.3 Magnetic field induced phase transitions

To observe the magnetization step around 4.5 T found in the powder sample below 1 K, the magnetization of the single crystal sample is measured by Kohno by the Faraday force method in the Sakakibara group in ISSP [84]. A clear jump of the magnetization is observed; the field derivatives of the magnetization dM/dH show peaks at 4.5 T in $H \perp ab$ and 3.9 T in $H // [110]$, respectively (fig. 4.6), which are similar to that observed in the powder sample. Therefore, the magnetization step at around 4 T is a common property of the powder sample and the single crystal of volborthite.

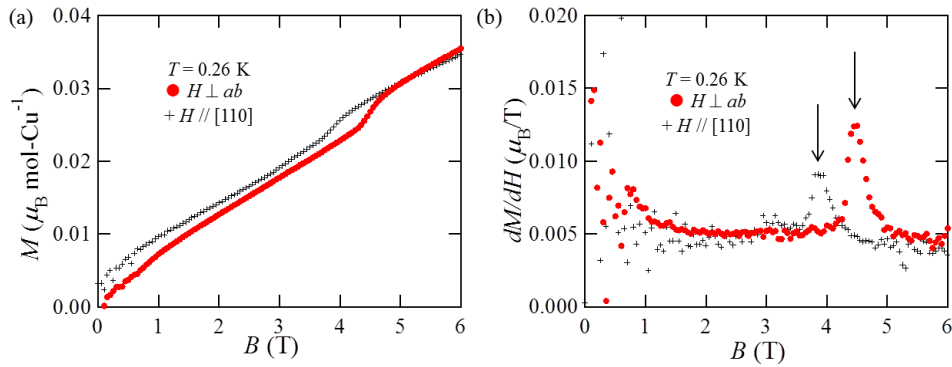


Figure 4.6. (a) Magnetization curves of volborthite at 0.26 K in $H \perp ab$ and $H // [110]$ and (b) their field derivative.

At higher fields, on the other hand, the magnetization curves of the single crystals are very different from that of the powder sample. Magnetization measurements are performed on two piles

of thick crystal in $H \perp ab$ and $H // ab$: the in-plane orientations are not aligned. Both in the magnetic fields $H // ab$ and $H \perp ab$, the magnetization increases steeply at around 20 T and then saturate at around the 1/3 of full magnetization (fig. 4.7(a)). The flat magnetization above 30 T should be a magnetization plateau, which continues up to at least 74 T. While the increase of magnetization occurs at almost the same magnetic field of the second magnetization step in the powder sample, its size is much larger in single crystals. The third magnetization step at 46 T observed in the powder sample is not present in the single crystals. Furthermore, the magnetization in the plateau phase is almost the 1/3 of the total magnetization in contrast to the 2/5 of the polycrystalline sample. The small anisotropy of the magnetization curve of the single crystal sample clearly indicates that the difference between polycrystalline and single crystal samples is not due to the powder averaging. The large increase of the magnetization and the entrance of the plateau is also observed at 4.2 K.

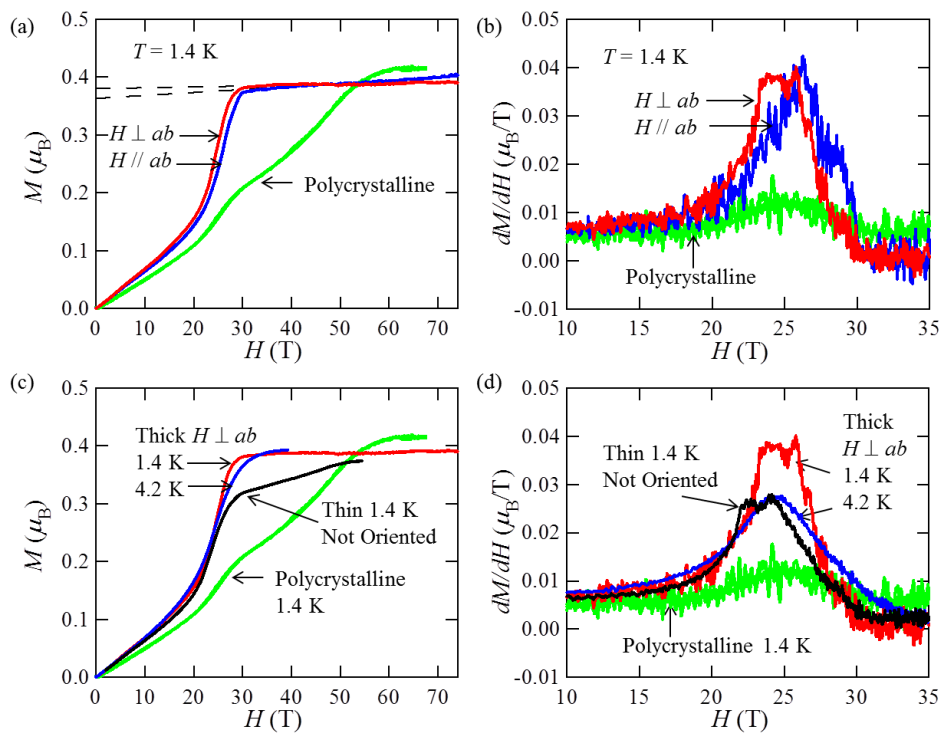


Figure 4.7. (a) Magnetization curves of volborthite thick single crystals in $H \perp ab$ and $H // ab$ and the polycrystalline sample measured at 1.4 K and (b) their field derivatives. (c) Magnetization curves of volborthite thick single crystals at 1.4 and 4.2 K in $H \perp ab$ and those of unaligned thin crystals and polycrystalline samples at 1.4 K and (d) their field derivatives.

The dashed lines in the fig.4.7(a) are the linear fittings of the magnetization curves in the plateau region, which intercept the magnetization axis at $0.38 \mu_B$ and $0.36 \mu_B$ in $H \perp ab$ and in $H // ab$, respectively. The small slope in the plateau region, which may be attributed to the Van Vleck paramagnetism, is $1.5 \times 10^{-4} \mu_B \text{ T}^{-1} \text{ mol-Cu}^{-1}$ in $H \perp ab$ and is larger in $H // ab$ as $5.1 \times 10^{-4} \mu_B \text{ T}^{-1} \text{ mol-Cu}^{-1}$. The difference of the saturation magnetization value in the plateau region should be attributed to the anisotropy of g -value. The g -values are estimated to be 2.28 and 2.16 in $H \perp ab$ and in $H // ab$, respectively, assuming that the magnetization in the plateau phase is the 1/3 of the full magnetization. These values are reasonable for the spin system made of Cu^{2+} ions and consistent with those estimated from the Curie-Weiss fittings above. Therefore, we conclude the high-field phase of volborthite is the 1/3 magnetization plateau.

The thin crystals, where the disorder of the orbital direction in approximately 10% of the Cu1 site is observed, show an intermediate magnetization curve between the thick crystals and the powder sample. The magnetization steeply increases around 20 T but the size of increase is smaller compared to the thick crystals. It continues to increase above 30 T with the slope of $2.5 \times 10^{-3} \mu_B \text{ T}^{-1} \text{ mol-Cu}^{-1}$, where the thick crystals show the 1/3 plateau, and then show a saturation behavior above 50 T. Note that the sample dependence observed in the magnetization curve of volborthite is unusually large, of which origin will be discussed in the next chapter.

The magnetic field derivative of the magnetization, dM/dH , are shown in fig. 4.7(b) and (d). An anomaly is found in the magnetic field range slightly below the 1/3 plateau region; it shows two kinks at 23.2 and 26.0 T in $H \perp ab$ and remains constant in between, indicating that the magnetization changes linearly and the most steeply there. Generally, a peak is observed in dM/dH at the entrance of magnetization plateau. The flat maximum may indicate the presence of another magnetic phase, which I call phase N, below the 1/3 plateau phase. This anomaly in dM/dH is broadened and the flat maximum is absent at 4.2 K. In $H // ab$, the anomaly seems to be distributed between 23-29 T due to the anisotropy of the g -value within the ab plane. In the thin single crystals, the similar flat maximum in the dM/dH is observed between 22 and 24 T, which is found in slightly lower field range compared to the thick crystals.

Figure 4.8(a) shows the H - T curves of the thick crystal of volborthite in the preliminary magnetocaloric effect measurements in the pulsed magnetic fields: the data of the down-field process is shown. In the measurements, the temperature of the sample is measured in the adiabatic conditions. Therefore, the obtained H - T curves indicate the isoentropic curve. The general feature is that the temperature of the sample decreases around 24 T and then increase rapidly at higher fields. These

results indicate that the entropy is large around 24 T and small at higher fields in the 1/3 plateau region. At around 24 T (fig. 4.8(b)), two kinks are observed in the isoentropic curves below 2 K and the temperature is almost constant in between. The field range coincides with the phase N observed in the magnetization curve. Therefore, the presence of phase N is demonstrated by the magnetocaloric effect measurements.

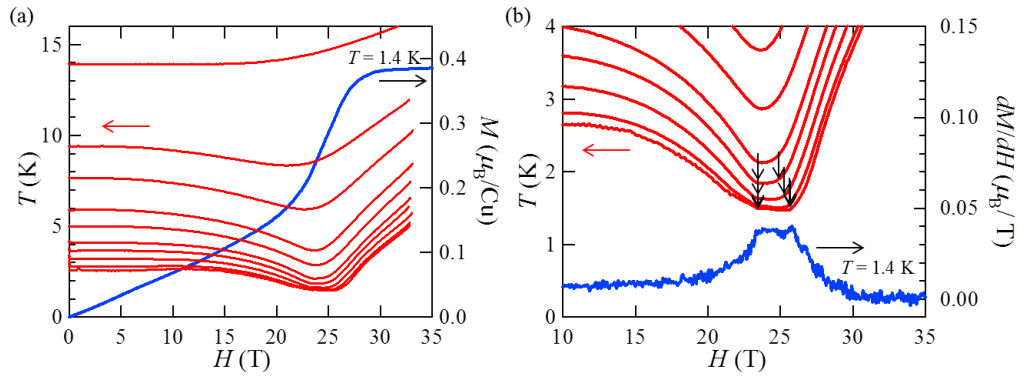


Figure 4.8. (a) The isoentropic curves obtained in the magnetocaloric effect measurements of the thick single crystal of volborthite below 15 K and up to 33 T. The magnetization curve is also plotted. (b) Enlarged graph at around 2 K and 24 T. The arrows indicate the kinks in the isoentropic curves. The field derivative of the magnetization curve is also plotted.

The magnetic entropy is estimated from the heat capacity data obtained at 14 T (fig. 4.9(a)): the difference between the up-field and down-field processes in the magnetocaloric effect measurements were small at around 15 T and better estimation of the entropy is expected around the region. The heat capacity of the $\text{Zn}_3\text{V}_2\text{O}_7(\text{OH})_2 \cdot 2\text{H}_2\text{O}$ at 0 T is used as the lattice heat capacity. The counter plot of magnetic entropy obtained from the linear interpolation of the data of the heat capacity and magnetocaloric effect measurements is shown in the fig. 4.9(b). The phase N has larger magnetic entropy compared to the phase II: the entropy of phase N at 1.5 K is comparable with that of the paramagnetic state at 2.5 K and 0 T. The large magnetic entropy may indicate that the phase N has large number of degenerate excitations in the low energy range. On the other hand, the entropy of the plateau region is much smaller than other magnetic phases.

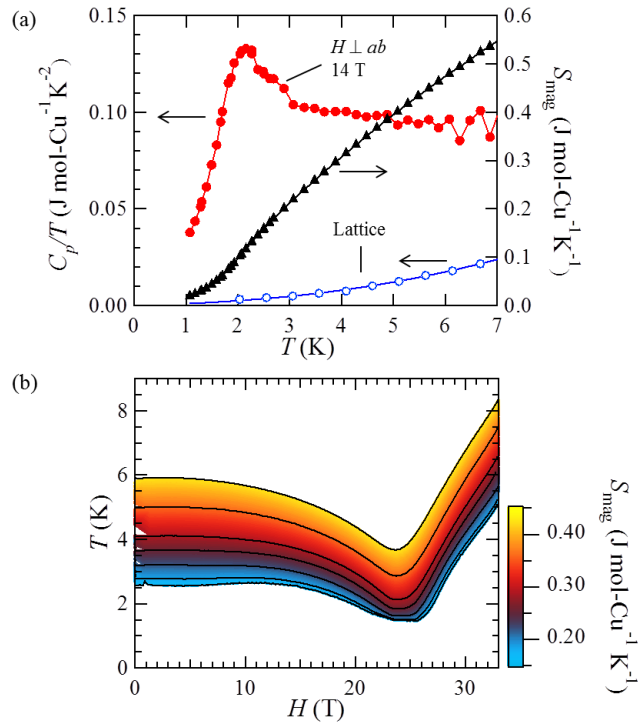


Fig.4.9. (a) Heat capacity of volborthite measured in the magnetic field of 14 T applied perpendicular to the kagome plane and estimated magnetic entropy. (b) The counter plot of magnetic entropy obtained from the linear interpolation of the data of the heat capacity and magnetocaloric effect measurements (black lines).

4.4 Discussion

4.4.1 Spin structure of the 1/3 plateau phase

Based on the data obtained from the magnetization, heat capacity, magnetocaloric effect measurements, and the NMR spectra shown below on the single crystal samples, the H - T phase diagram of volborthite are obtained (fig 4.10). There are five magnetic phases, I, I', II, N, and the 1/3 plateau. It is noted that the phase I', which precedes the phase I as lowering temperature, is not a ground state.

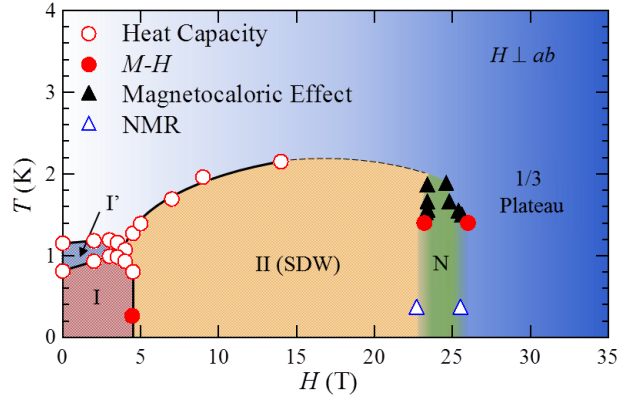


Figure 4.10. The H - T phase diagrams of volborthite single crystal in $H \perp ab$. The phase boundaries expressed as the dashed line and around phase N are not well determined at the present stage due to the limited data points.

First, I discuss the spin structure in the $1/3$ plateau phase from the crystal structure. The spin models expected from the orbital arrangements are shown in fig. 4.11(a). The sign and the size of superexchange interactions in copper oxides are known to depend on the angle made by Cu ions and bridging oxide ion; the coupling is usually ferromagnetic if the angle is smaller than 95° and changes to be strongly antiferromagnetic as the angle approach to 180° [32]. In the $P2_1/a$ structure of volborthite at 50 K, the angles for the NN Cu2 ions (J_1) are $93.37(9)^\circ$ and $98.92(9)^\circ$ ($93.20(9)^\circ$ and $99.09(9)^\circ$), which suggest the J_1 is ferromagnetic or weakly antiferromagnetic: the angles in the parentheses are those in one of the two crystallographically different kagome layers, which are almost the same with the first ones. Moreover, the chain-like arrangement of the $d_{x^2-y^2}$ -type orbitals of Cu2 sites usually gives rise to the antiferromagnetic coupling between NNN Cu2 ions (J_2). Actually, compounds possessing similar chain made of $d_{x^2-y^2}$ -type orbitals such as LiCuVO_4 are studied as the model compound of frustrated J_1 - J_2 chain magnet with ferromagnetic J_1 and antiferromagnetic J_2 .

On the other hand, the angles at the NN Cu1 and Cu2 ions (J' and J'') are $102.47(9)^\circ$ ($102.83(9)^\circ$) for J' and $104.60(9)^\circ$ ($104.57(9)^\circ$) for J'' , respectively. Therefore, antiferromagnetic J' and J'' is expected. It is noted that two and three lobes of the $d_{x^2-y^2}$ -type orbitals are involved in J' and J'' , respectively. The extra lobe in J' , which is absent in J'' , may add small ferromagnetic direct exchange interaction to J' . Because the ferromagnetic J_1 is expected along the spin chain of Cu2 site and the spin chains are antiferromagnetically coupled with the interchain Cu1 spins, the ferrimagnetic state (fig. 4.11(b)), where the chain is polarized and the interstitial spin is

anti-polarized along the magnetic field, is the candidate for the spin structure of 1/3 plateau phase. The ferrimagnetic state is compatible with the robustness of 1/3 plateau phase; there is no frustration in the NN interactions in the spin structure and the state should be stable until the magnetic field of the magnitude comparable to the J' or J'' is applied. Inversely, the frustration observed in volborthite is considered to be caused by the competition between ferromagnetic J_1 and antiferromagnetic J_2 .

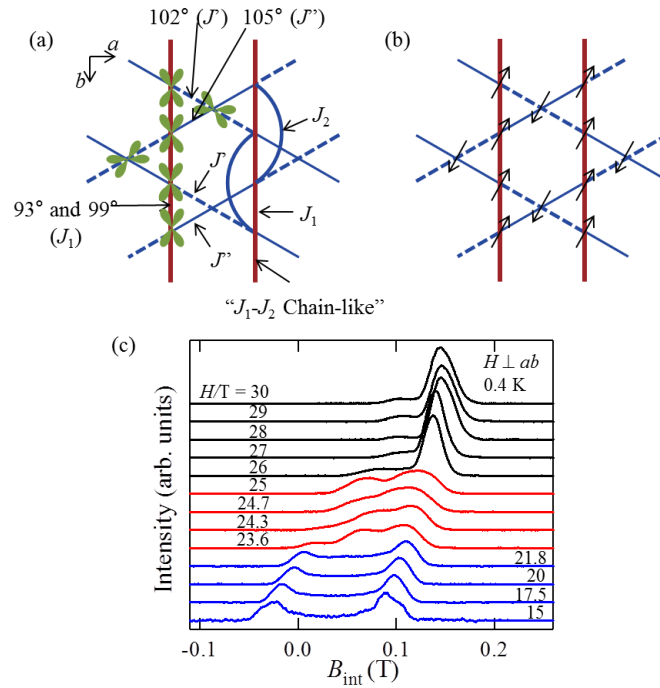


Figure 4.11. (a) The orbital pattern and the spin model of volborthite expected from the in the lowest temperature $P2_1/c$ structure. (b) Ferrimagnetic state in the kagome lattice of volborthite. (c) ^{51}V NMR spectra in the thick single crystal of volborthite in $H \perp ab$ [P1].

4.4.2 Magnetic phases below the 1/3 plateau and coupled J_1 - J_2 chain model

The ^{51}V -NMR experiments performed by Yoshida using the thick single crystal sample have provided the information of the spin structures (fig. 4. 11(c), [P1]). The spectra above 26 T are almost a single peak, which indicates the simple spin structure. This result is compatible with the ferrimagnetic state expected from the crystal structure considered above. Between 26 and 28 T, the spectra are almost a single peak but the shift increases. Below 22 T in phase II, double-horn type spectra, which are characteristic for incommensurate spin structures, are observed. Further NMR experiments have revealed that the collinear SDW, where spins are polarized to the field and have

the modulated magnitude of magnetic moments, is the most likely. Between 23 and 25 T, where the phase N is observed in the magnetization and the magnetocaloric effect measurements, the spectra comprising two Gaussian-like peaks are observed. The spectra between 23 and 25 T cannot be reproduced by the superposition of the spectra found in phase II and the 1/3 plateau, therefore, the NMR spectra also demonstrate the presence of phase N. The spectra in phase N suggest the inhomogeneous distribution of the internal field rather than the conventional magnetic order.

The ferrimagnetic state of volborthite can be regarded as magnetization saturation of the J_1 - J_2 chain embedded in the kagome lattice. Moreover, the phases found in volborthite in the magnetic fields, which are phases I, II (SDW), N and the 1/3 plateau (saturated J_1 - J_2 chain), reminds us the phases expected in the quasi-1D J_1 - J_2 chain system in magnetic fields: helical, SDW, nematic, and ferromagnetic (magnetic saturation) phases occurs as increasing the magnetic field. There is an analogy in the crystal structure and the magnetic phases between volborthite and the J_1 - J_2 chain. From this analogy, I proposed the possibility of the realization of spin nematic phase in the phase N of volborthite [P1]. It is noted that similar “coupled J_1 - J_2 chain model” and the possibility of the wide 1/3 plateau was theoretically proposed in 2008 by Janson et al. for the $C2/m$ structure of volborthite [85], however, the model did not predict the rich magnetic phase transitions and the expected magnetization curve for the model was not consistent with the complex magnetization curve observed in the powder sample.

4.4.3 Coupled trimer model proposed by theoretical studies

Stimulated by our experiments, Janson et al. have performed theoretical study based on the first principle calculation and the fittings of the magnetization data to estimate the values of J s and construct a spin model of volborthite [86]. They proposed another spin model with large $J'' = 252$ K and $J' : J : J_1 : J_2 = 1 : -0.2 : -0.5 : 0.2$ (fig.4. 12(b)). The calculation is roughly consistent with the structural consideration except for the sign of J' , which is weakly ferromagnetic in the calculation although strongly antiferromagnetic interaction is expected from the bond angles. They suggest that quite large J'' is caused by the long range super exchange path through Cu-O-V-O-Cu, which is absent for the superexchange path of J' (fig. 4.12(c)).

Assuming J'' is much larger than others, volborthite can be regarded as a spin system made from linear trimers coupled by J'' , which have spin 1/2 in the ground state. Based on the trimers, effective J_1 - J_2 - J_2' square lattice model is proposed (fig.4. 12(d)). The model is similar to the J_1 - J_2 square lattice model where spin nematic state is expected near the ferromagnetic state. In this effective

J_1 - J_2 - J_2' square lattice model, the formation of bound magnon pair, which may lead to the spin nematic phase, is predicted below the magnetization saturation of the spin 1/2 on the trimer (1/3 plateau state) [86].

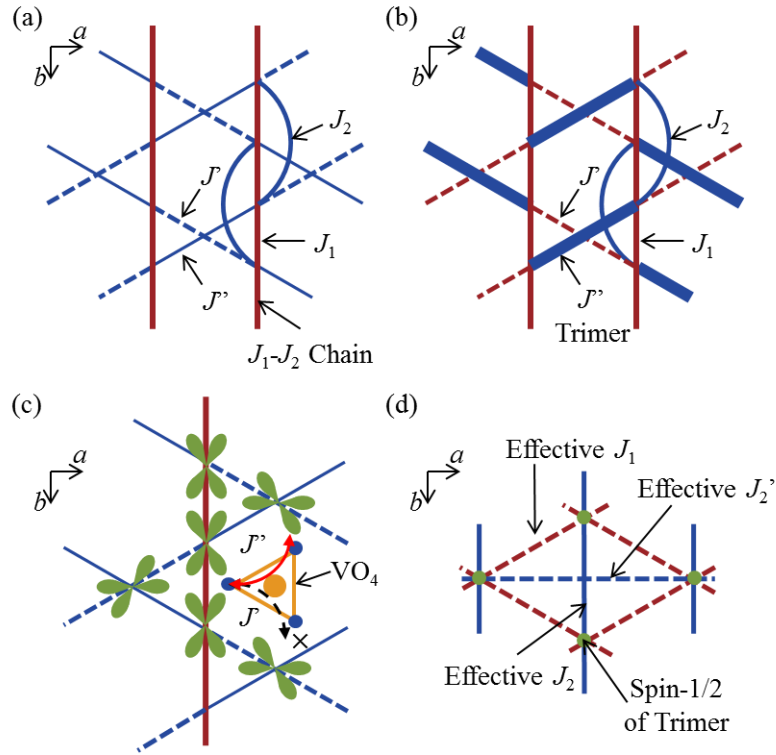


Figure 4.12. The spin models proposed for volborthite. The red and blue lines indicate the ferromagnetic and antiferromagnetic interactions, respectively. (a) J_1 - J_2 chain based model expected from the bond angles. (b) Trimer based model proposed by the first principle calculation. (c) Cu-O-V-O-Cu superexchange path proposed in the theoretical study. (d) Effective J_1 - J_2 - J_2' square lattice model made from the trimer model.

The relationship between the “coupled J_1 - J_2 chain model” and the “coupled trimer model” are considered. The difference is the sign and magnitude of J and J' . Antiferromagnetic J with the similar magnitude with J' is supposed in the former model ($J \sim J'$), on the other hand, J is weakly ferromagnetic and J' is strongly antiferromagnetic ($|J| < J'$) in the latter model. In the former model, there is no frustration in the NN interactions and the frustration is caused by J_2 . In the latter model, there is already a frustration in the NN interactions in addition to the frustration caused by J_2 .

In the former model, if the spin nematic phase is present, the magnon pair is expected to be formed on a J_1 - J_2 chain in the kagome lattice; the origin to stabilize the magnon pair is ferromagnetic J_1 and the hopping process of magnon pair caused by antiferromagnetic J_2 . In the latter model, the magnon pair is defined for two trimers and the origin to stabilize it is ferromagnetic effective J_1 , which is mainly caused by J_1 and J' in the original lattice. The hopping process of the magnon pair is caused by effective J_2 (caused mainly by J_2 in the original lattice) and effective J_2' (caused mainly by the second order perturbation process of J_1 and J' in the original lattice). The order of nematic director is expected along the b -axis if the nematic phase is present in both of the models.

4.5 Summary

- The magnetic phase diagram of volborthite is obtained by the heat capacity, magnetization, magnetocaloric effect, and NMR measurements; phase N and the 1/3 plateau are found in the single crystal experiments. The phase N has steep change of magnetization linearly to the magnetic field and large magnetic entropy.
- Candidate spin states in the 1/3 plateau is the ferrimagnetic state which is the effective magnetization saturation of the J_1 - J_2 chains on the kagome lattice and the magnetization saturation of the linear trimers which carry the effective spin 1/2.
- I propose the possibility of the realization of spin nematic state in phase N caused by the competing ferromagnetic and antiferromagnetic interactions.
- Studying the magnetic excitation in phase N would give the information on the nature of the phase. Inelastic neutron scattering experiments and measuring the temperature dependences of heat capacity would be effective for the purpose.
- Unusually large sample dependence is found in the magnetization curve.

Chapter 5. Structural and magnetic properties of engelhauptite and their comparison with volborthite

5.1 Brief history and outline

A new mineral engelhauptite $\text{KCu}_3\text{V}_2\text{O}_7(\text{OH})_2\text{Cl}$, which has similar chemical composition and crystal structure to volborthite $\text{Cu}_3\text{V}_2\text{O}_7(\text{OH})_2 \cdot 2\text{H}_2\text{O}$, is reported in 2013 [45]. The similarity becomes clearer by writing the chemical formula as $\text{Cu}_3\text{V}_2\text{O}_7(\text{OH})_2 \cdot \text{KCl}$. From the analogy to volborthite and the hexagonal space group $P6_3/mmc$, engelhauptite is expected to be a candidate of the spin 1/2 perfect kagome antiferromagnet. I have synthesized the powder sample of engelhauptite for the first time and studied its structural and magnetic properties. As a result of the structural analysis based on the powder XRD experiments, I found that synthetic engelhauptite has the monoclinic structure with the space group $P2_1/m$, which is different from the natural mineral. Although the kagome lattice is heavily distorted contrary to the expectation, I found interesting similarities in the orbital arrangement on the kagome lattice between engelhauptite and volborthite; there are J_1 - J_2 chains made of $d_{x^2-y^2}$ -type orbitals and another $d_{x^2-y^2}$ -type orbital in between. The structural and magnetic properties of engelhauptite and volborthite are compared and their appropriate spin models are discussed.

5.2 Synthesis and elemental analysis

CuO (4N, Raremetallic) and V_2O_5 (4N, Raremetallic) are mixed in the molar ratio of 3 : 1 with 1.0 g of KCl (2N, Wako) and 10 ml of pure H_2O in the Teflon beaker of 45 ml volume. The V_2O_5 powder is well ground in an agate mortar before the synthesis to increase the reactivity. The vessel is heated at 200°C for 24 h and the solid product containing polycrystalline engelhauptite and volborthite and the residual starting materials is obtained. They are filtered, well ground in the agate mortar, and reacted again with the KCl and H_2O in the same condition. As a result, pure orange-yellow powder of engelhauptite is obtained (fig. 5.1(a)). It is noted that the Rb-, Cs-, and NH_4 - analogues of engelhauptite are successfully obtained in the similar synthetic conditions. I focused on the K-compound (engelhauptite) as all the compounds showed the similar magnetic properties in the preliminary magnetic properties measurements.

The single crystal of engelhauptite is topochemically obtained using the single crystals of volborthite as a starting material. Several single crystals of volborthite are reacted with 1.0 g of KCl (2N, Wako) at 170°C in 10 ml of pure H_2O . The reaction speed seems to be very slow and the

reaction occurred inhomogeneously even after 7 days of reaction (fig. 5.1(b)). The orange region, where engelhauptite is expected to be formed, is cut from the crystal and used for the single crystal XRD experiments.

The elemental analysis by the ICP-AES experiment on the powder sample showed that the molar ratio of $K : Cu : V = 1 : 2.93 : 2.02$, suggesting there is $\sim 2\%$ of Cu deficiency from the ideal composition: the Cl ion cannot be analyzed in this ICP experiments.

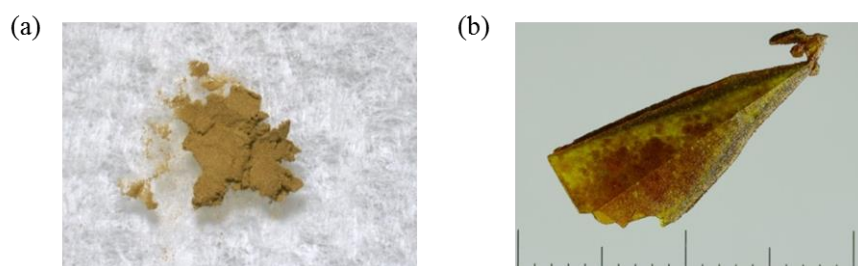


Figure 5.1. (a) Powder sample of engelhauptite. (b) A single crystal of volborthite which is partly transformed into engelhauptite after the topochemical reaction in KCl_{aq} .

5.3 Structural analysis

Figure 5.2 shows the powder XRD pattern obtained from the powder sample of engelhauptite. The peaks can be indexed by the monoclinic unit cell $a = 5.8653(2) \text{ \AA}$, $b = 14.5747(3) \text{ \AA}$, $c = 6.0794(2) \text{ \AA}$, $\beta = 119.049(2)^\circ$. The space group is determined to be $P2_1/m$ or $P2_1$ from the extinction rule; the $(0k0)$ reflections with $k = 2n + 1$ are absent selectively.

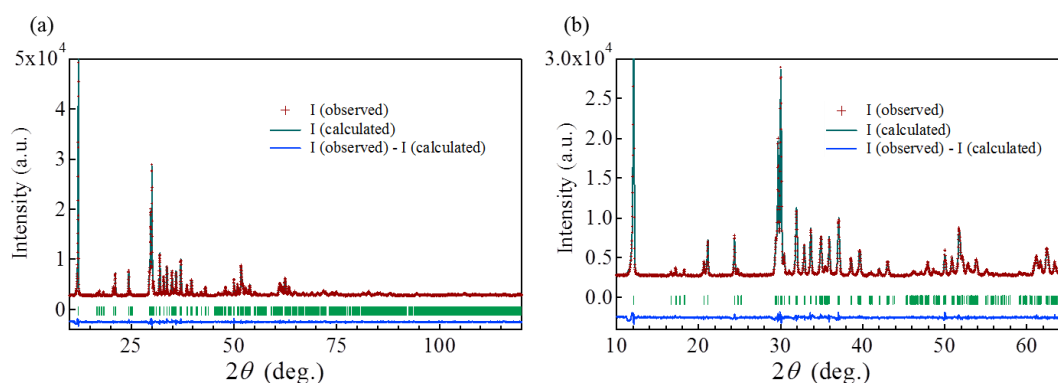


Figure 5.2. (a) Powder XRD pattern and its Rietveld fitting of engelhauptite. (b) Enlarged graph of the powder pattern and the fitting.

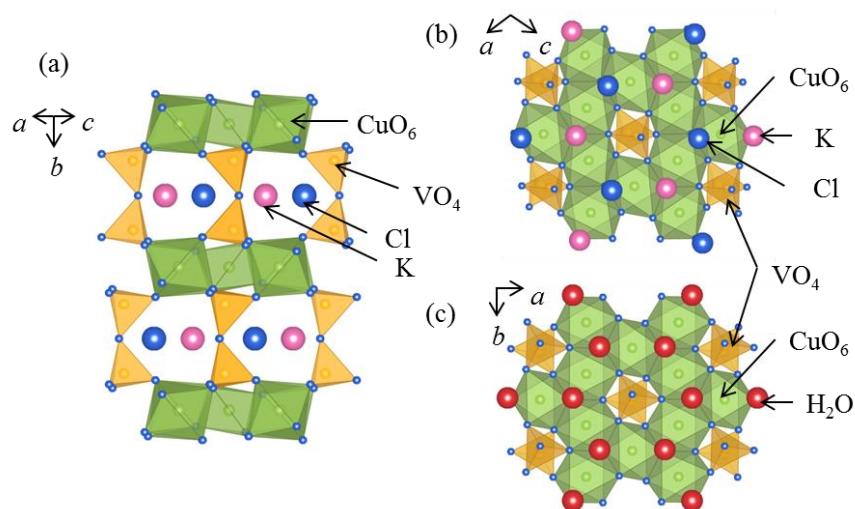


Figure 5.3. (a) The structural model of the synthetic engelhauptite. Crystals Structures of (b) synthetic engelhauptite and (c) volborthite seen perpendicular to the kagome layer.

To determine the atomic positions, refinements of the powder pattern by the Rietveld method are performed. Initial structural model is made to reproduce the volborthite-like kagome layers and V_2O_7 pillars in the space group $P2_1/m$. Two H_2O molecules are replaced by K and Cl ions in an ordered manner (fig. 5.3(b)). As shown in the fig. 5.2, the powder pattern is well reproduced in the atomic positions shown in the table 5.1 ($R_{wp} = 2.34$, $S = 1.34$). The occupancies of Cu sites are fixed to 0.98 based on the ICP experiments and the occupancy of Cl site is refined as a free parameter. 2% of defect in the Cl site is found. Considering the charge balance, the amount of the defect of the Cl site may be larger than the estimated value in the Rietveld refinement.

Table 5.1. Structural parameters of engelhauptite at 293 K

Atom	x	y	z	U_{iso}	Occ.
K	0.334(1)	0.25	0.6974(9)	0.032(2)	1
Cl	0.666(1)	0.25	0.4125(9)	0.034(3)	0.980(7)
Cu1	0.5	0	0	0.0139(8)	0.98
Cu2	0	0	0.5	0.007(1)	0.98
Cu3	0.5	0	0.5	0.019(2)	0.98
V	0.9964(7)	0.1286(1)	0.0394(6)	0.0090(8)	1
O1	0.980(2)	0.25	0.077(2)	0.010(4)	1
O2	0.662(2)	0.4444(4)	0.325(1)	0.023(2)	1
O3	0.171(2)	0.4223(4)	0.337(2)	0.015(3)	1
O4	0.703(2)	0.4111(6)	0.898(2)	0.011(4)	1
O5	0.132(2)	0.3947(7)	0.865(2)	0.005(3)	1

The topochemically obtained crystals of engelhauptite are studied by single crystal XRD experiments in ISSP. Almost the same crystal structure obtained from the powder XRD experiments with the unit cell of $a = 5.8782(8) \text{ \AA}$, $b = 14.551(2) \text{ \AA}$, $c = 6.0521(8) \text{ \AA}$, $\beta = 118.986(2)^\circ$ and the space group $P2_1/m$ is observed. However, the final $R1$ is 11.2%, which may indicate the sample quality is not good enough. The reason is considered to be the inhomogeneity of the crystal caused by the slow reaction speed.

The crystal structure of engelhauptite is made of $\text{Cu}_3\text{O}_6(\text{OH})_2$ layers, where Cu^{2+} ions form distorted kagome lattice, and V_2O_7 pillars as found in volborthite. There are K^+ and Cl^- ions in engelhauptite between the kagome layers instead of two H_2O molecules in volborthite. There are crystallographically three Cu sites in a kagome layer and all the CuO_6 octahedra are elongated along one axis ([4 + 2] coordination), therefore, the $d_{x^2-y^2}$ -type orbitals carry the spin 1/2 in all of the Cu sites (table 5.2, fig. 5.4(a,b)). It is noted that the natural mineral has one kind of squeezed octahedra ([2 + 4] coordination), where the $d_{3z^2-r^2}$ -type orbitals appear to carry the spin 1/2 (fig. 5.4(c)).

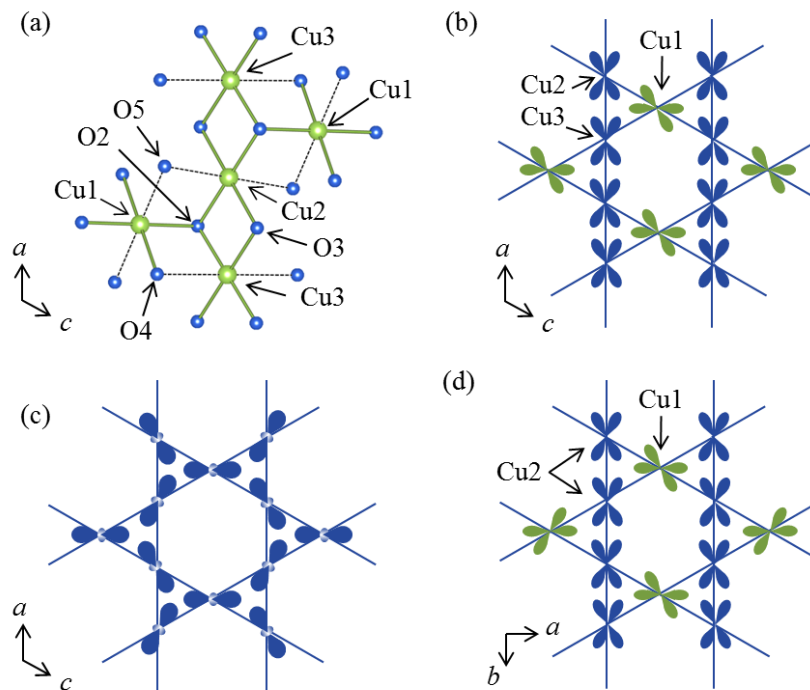


Figure 5.4. (a) Coordination environment around the Cu atoms in the synthetic engelhauptite. The solid and dashed lines indicate the squeezed and elongated Cu-O bond, respectively. Orbital arrangements in the kagome lattice of (b) synthetic engelhauptite, (c) natural engelhauptite, and (d) low temperature phase of volborthite.

Table 5.2. Cu-O distances in synthetic (left) and natural (right) engelhauptite.

Synthetic Powder	Bond Length (Å)	Natural Mineral	Bond Length (Å)
Cu1-O2	1.908(8) ×2	Cu-OH	1.92(1) ×2
Cu1-O4	2.049(10) ×2	Cu-O	2.23(2) ×4
Cu1-O5	2.443(10) ×2		
Cu2-O2	1.916(7) ×2		
Cu2-O3	2.058(7) ×2		
Cu2-O5	2.492(12) ×2		
Cu3-O2	1.917(7) ×2		
Cu3-O3	2.033(7) ×2		
Cu3-O4	2.481(13) ×2		

The situation that the $d_{3z^2-r^2}$ -type orbital is found in natural mineral but the $d_{x^2-y^2}$ -type orbital is found in the synthetic sample is similar to the case of volborthite: the $d_{3z^2-r^2}$ -type orbital is selected in the Cu1 site of the natural crystal of volborthite but the $d_{x^2-y^2}$ -type orbital is found in the single crystals in this study. As discussed in the chapter 3, the $d_{3z^2-r^2}$ -type orbital in volborthite is likely the average structure of the randomly distributed orthogonal $d_{x^2-y^2}$ -type orbitals. The hexagonal unit cell $a = 5.922(2)$ Å, $c = 14.513(5)$ Å, $\alpha = \beta = 90^\circ$, $\gamma = 120^\circ$ of natural engelhauptite may be observed as an average structure of the monoclinic unit cell found in the synthetic sample when there are disorder such as stacking fault and contamination of other elements. Moreover, the $R1$ reported for the natural single crystal is 11.2%, suggesting the refinement is not perfect. Therefore, the $P6_3/mmc$ structure reported in the natural crystal of engelhauptite is likely an average structure of the disordered monoclinic $P2_1/m$ structure found in the synthetic sample.

The orbital pattern found in the synthetic engelhauptite is shown in fig. 5.4(b). There are chains made of edge sharing $d_{x^2-y^2}$ -type orbitals and another $d_{x^2-y^2}$ -type orbitals are aligned in the same direction in between. Interestingly, this orbital pattern is identical to the room temperature $C2/c$ structure of volborthite. It is noted that this high-temperature orbital pattern cannot be quenched in the low temperature in volborthite as it shows the structural phase transition (orbital flipping transition) around room temperature into the $I2/a$ structure, where the interchain orbitals are aligned in the staggered arrangement (fig. 5.4(d)).

5.4 Magnetic properties

Magnetic susceptibility of the powder sample of engelhauptite measured at 2-350 K in the magnetic field of 1 T is shown in the fig. 5.5(a). The Curie-Weiss fitting above 200 K results $C = 0.433(20)$ cm³ K mol-Cu⁻¹, $\Theta = 90(8)$ K, $\chi_0 = 8(3) \times 10^{-5}$ cm³ mol-Cu⁻¹. Assuming $S = 1/2$, g -value is

estimated to be 2.15(5), which is slightly larger than 2 and a typical value for Cu^{2+} oxides. The large Weiss temperature indicates the antiferromagnetic interaction is dominant. The Weiss temperature is similar to the 90(9) K estimated for the high temperature $C2/c$ phase of volborthite, which has the same orbital pattern with synthetic engelhauptite.

The magnetic susceptibility shows a broad peak at around 18 K, which indicates the development of the short range antiferromagnetic correlation. The broad peak is observed at almost the same temperature with volborthite (fig. 5.5(a)). This coincidence may indicate the magnitude of the dominant antiferromagnetic interaction is similar in these two compounds. A small downturn of the susceptibility is observed at 6 K, which may indicate an antiferromagnetic order. Except for the broad peak at 18 K and the anomaly at 6 K, no other anomalies are observed in engelhauptite, indicating the absence of the structural phase transitions observed in volborthite (T_{S1} and T_{S2} in fig. 5.5(b)).

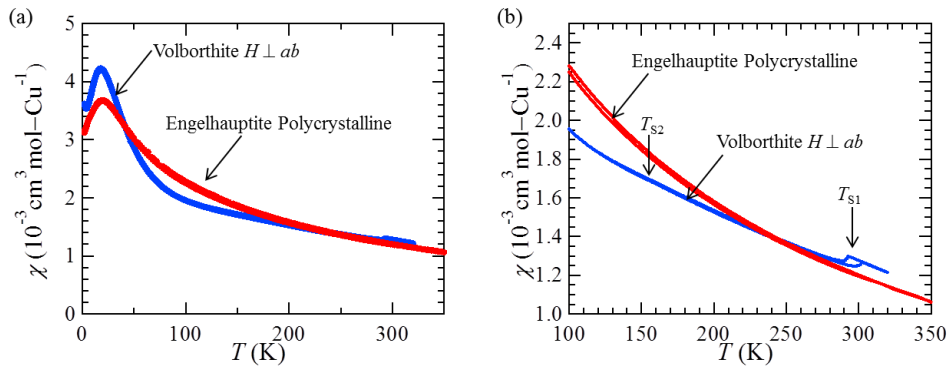


Figure 5.5. Temperature dependences of the magnetic susceptibility of the powder sample of engelhauptite and the thick single crystal of volborthite at (a) 2-350 K and (b) 100-350 K. The T_{S1} and T_{S2} in (b) indicate the temperature of structural phase transitions in volborthite.

To investigate the anomaly observed at 6 K, the magnetic susceptibilities are measured in different magnetic fields at 0.01-7 T at low temperatures (fig. 5.6(a)). In the measurement at 0.01 T, a peak is observed at 6 K in the ZFC measurement and a steep increase is observed as lowering the temperature in the FC measurements. The hysteresis found at high temperature above 6 K should be an experimental error caused by the small raw magnetization. The anomaly is suppressed as increasing the magnetic field and the hysteresis disappeared completely at 1 T. These results suggest that engelhauptite shows an antiferromagnetic magnetic order at around 6 K which accompanies tiny weak-ferromagnetic moment.

Heat capacity measurements are performed at 2-25 K to get information on the possible magnetic order at 6 K. At zero field, the C_p/T shows a shoulder at 6 K, where an anomaly is observed in the magnetic susceptibility measurements (fig. 5.6(b)). Therefore, I conclude that the magnetic anomaly at 6 K observed in the magnetic susceptibility is a bulk property. The relatively small anomaly is a typical behavior of the frustrated magnets, which gradually emit the entropy from higher temperatures. The shoulder in the heat capacity is almost insensitive to the magnetic fields, suggesting the ground state is unchanged up to at least 9 T.

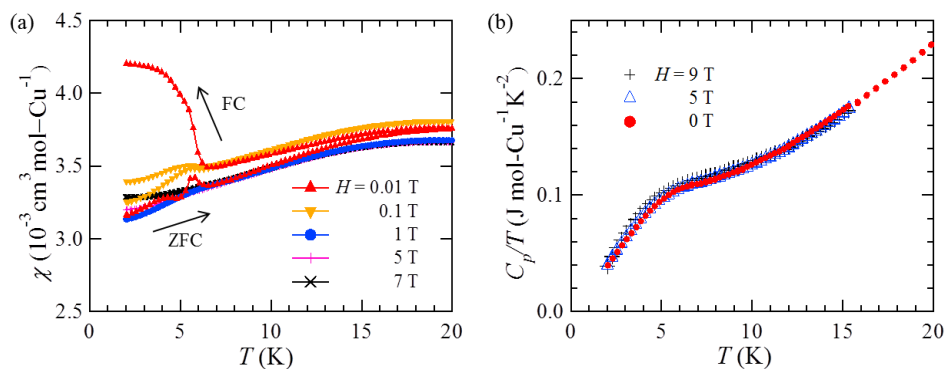


Figure 5.6. (a) Temperature dependences of magnetic susceptibility of the powder sample of engelhauptite and the thick single crystal of volborthite at 2-20 K. (b) Temperature dependences of the heat capacity of the powder sample of engelhauptite in the magnetic field of 0, 5, and 9 T.

High-field magnetization measurements are performed on the powder sample of engelhauptite at 1.4 and 4.2 K (fig. 5.7(a)). In both of the temperature, magnetization increases monotonously up to 50 T, above which the slope becomes smaller. The magnetization exceeds the 1/3 of the full magnetic moment at around 50 T and continues to increase up to 72 T. The 1/3 magnetization plateau found in the volborthite, which has the similar crystal structure to engelhauptite, is not observed. The field derivative of the magnetization shown in the fig. 5.7(b) shows a broad maximum at around 42 T at 1.4 K, which may indicate the change of the spin structure. The anomaly is slightly broadened at 4.2 K.

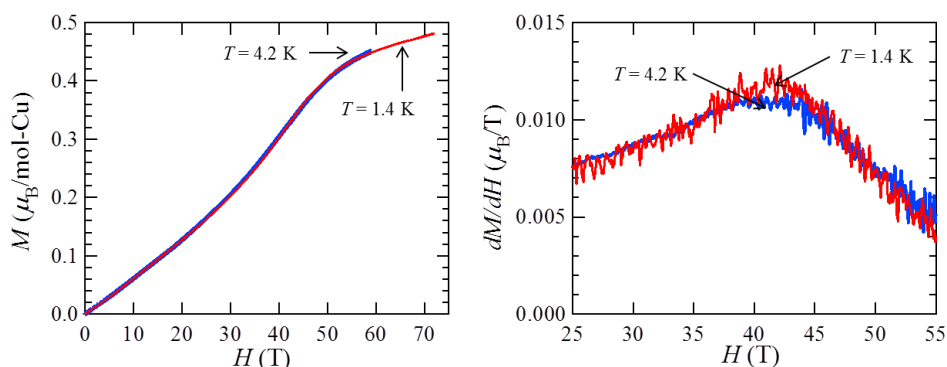


Figure 5.7. (a) High-field magnetization curves of the powder sample of engelhauptite at 1.4 and 4.2 K up to 72 K and (b) their magnetic field derivative.

5.5 Discussion

5.5.1 Absence of structural phase transition in engelhauptite

Structural phase transition is not observed in engelhauptite, although volborthite, which has similar crystal structure at high temperatures, shows two structural phase transitions at around room temperature and 155 K. As they have similar framework made of CuO_6 octahedra and V_2O_7 pillars in common, the difference should be attributed to the ions or molecules between the frameworks: K^+ and Cl^- ions in engelhauptite and H_2O molecules in volborthite. As discussed in the chapter 3, the structural analyses of volborthite suggest that the CuO_6 octahedra and V_2O_7 pillars change their structures cooperatively with the H_2O molecules coupled with the framework via hydrogen bonding. On the other hand, the framework is coupled with K^+ and Cl^- ions via coulomb interaction in engelhauptite. This is seen from the difference in the way of the twist of the V_2O_7 pillars; two VO_4 tetrahedra are arranged so as to decrease the coulomb repulsion between O and Cl^- ions in engelhauptite (fig. 5.8). Moreover, V-O1-V angle is smaller (162° at 293 K) in engelhauptite than in volborthite (171° at 293 K); V_2O_7 pillars appear to interact more strongly with K^+ and Cl^- ions in engelhauptite than in volborthite. These structural differences suggest that the framework is locked by the ions and the structural transition is impossible in engelhauptite, while it is possible because the arrangement of H_2O molecule are easily changed cooperatively with the framework in volborthite.

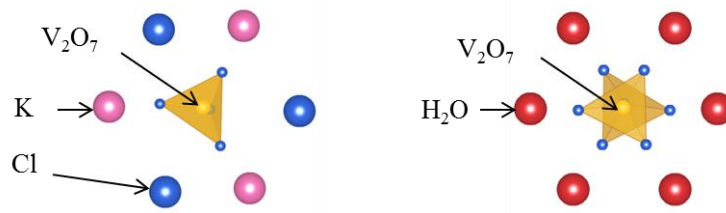


Figure 5.8. Crystal structures around V_2O_7 pillars in engelhauptite (left) and volborthite (right).

5.5.2 Spin models of engelhauptite and volborthite

I consider the spin model of engelhauptite based on the crystal structure and the high-field magnetization measurements by comparing them with those of volborthite. The bond lengths and the bond angles which are important for the magnetic interactions are shown in the table 5.3. The bond angles at the NN Cu ions along the chain made of edge sharing $d_{x^2-y^2}$ -type orbitals, J_1 in the fig. 5.9, is approximately 92° and 100° , which are close to 93° and 99° found in volborthite. As in the J_1 - J_2 chain compounds, ferromagnetic NN interaction J_1 and antiferromagnetic NNN interaction J_2 are expected along the chain. There are two kinds of NN interactions between the spins on the chain and spins between the chain, J' and J'' , which have the bond angles of 105° and 104° , respectively, in engelhauptite and 103° and 105° , respectively, in volborthite. The similarities in the local structure between engelhauptite and volborthite suggest that the corresponding interactions between them have similar magnitude.

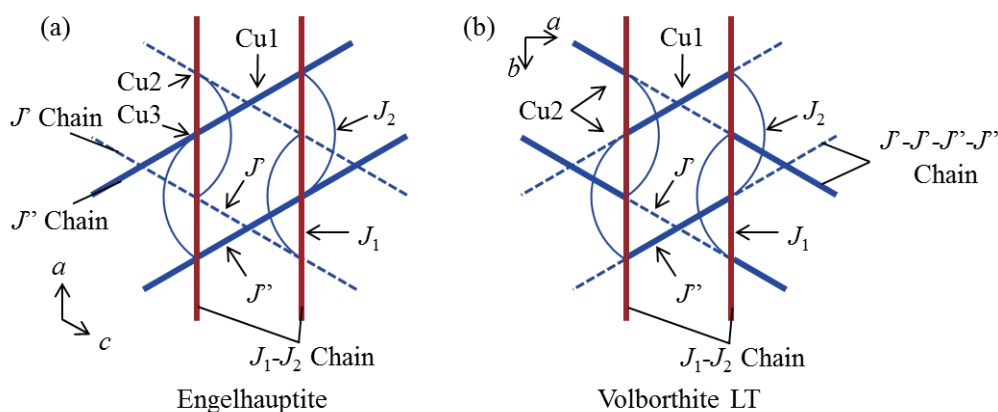


Figure 5.9. Spin models of (a) synthetic engelhauptite and (b) low temperature structure of volborthite expected from their crystal structures and the orbital arrangements.

Table 5.3. Selected bond lengths and bond angles in the powder sample of engelhauptite at 293 K and the single crystal sample of volborthite at 50 K.

Engelhauptite at 293 K	Cu-Cu (Å)	Cu-O-Cu (°)	Volborthite at 50 K	Cu-Cu (Å)	Cu-O-Cu (°)
Powder			Single, Layer A		
J_1	2.9326(1)	91.6(3) 99.9(2)	J_1	2.9228(3)	93.37(9) 98.92(9)
J_2	5.8652(3)		J_2	5.8415(3)	
J'	3.0397(1)	105.3(3)	J'	3.0616(3)	102.47(9)
J''	3.0304(1)	104.8(3)	J''	3.0580(3)	104.60(9)
			Single, Layer B		
			J_1	2.9215(3)	93.20(9)
			J_2	5.8415(3)	
			J'	3.0202(3)	102.83(9)
			J''	3.0531(3)	104.57(9)

Assuming that corresponding interactions have similar values in engelhauptite and volborthite, the two possible spin models are examined. One is the case with ferromagnetic J_1 , antiferromagnetic J_2 and strongly antiferromagnetic J' and J'' with similar magnitude expected from the crystal structure ($J' \sim J'' > |J_1|$ and J_2). The second case is the interactions proposed in the first principle calculation for volborthite, which are ferromagnetic J_1 , antiferromagnetic J_2 , ferromagnetic J' , and strongly antiferromagnetic J'' ($J'' > |J_1|, J_2$, and $|J'|$). It should be noted that the Cu-O-V-O-Cu superexchange path, which may cause strongly antiferromagnetic J'' in volborthite, is also present in engelhauptite.

In the former case, the spin model for the two compounds are identical to the coupled J_1 - J_2 chain model [85] and both of the materials are expected to show the 1/3 magnetization plateau with the ferrimagnetic spin structure. Therefore, the former case fails to explain the experimental results.

In the latter case, spin models of engelhauptite and volborthite are largely different due to the different arrangement of J' and J'' (fig. 5.9). Engelhauptite can be regarded as a spin system made of antiferromagnetic chains with strong intrachain interaction J'' between Cu1 and Cu3 and the coupled interchain spin on Cu2 (fig. 5.10(a)). On the other hand, volborthite can be regarded as the coupled antiferromagnetic linear trimers (fig. 5.10(b)). The saturation behavior of the magnetization curve in engelhauptite at slightly above the 1/3 of the full magnetization around 50 T can be understood as the magnetization saturation of the spins on Cu2 site prior to the Cu1-Cu3 chains. Moreover, there is no reason that the 1/3 plateau state with $\uparrow\uparrow\downarrow$ spin structure is stabilized. On the other hand, the 1/3 plateau of volborthite can be understood as the magnetization saturation of the spin 1/2 on the linear spin trimer made of J'' . Therefore, the experimental results are consistent with the case of strongly antiferromagnetic J'' and ferromagnetic J' , which produce antiferromagnetic chains and linear

trimers in engelhauptite and volborthite, respectively. Schnyder et al. studied the magnetic properties of the anisotropic kagome lattice spin system in the one-dimensional limit ($J \gg J'$ in the fig. 5. 10(c)) and found that the system shows a spiral order along the chain direction [87]. The magnetic order realized in engelhauptite might be a similar spiral magnetic order.

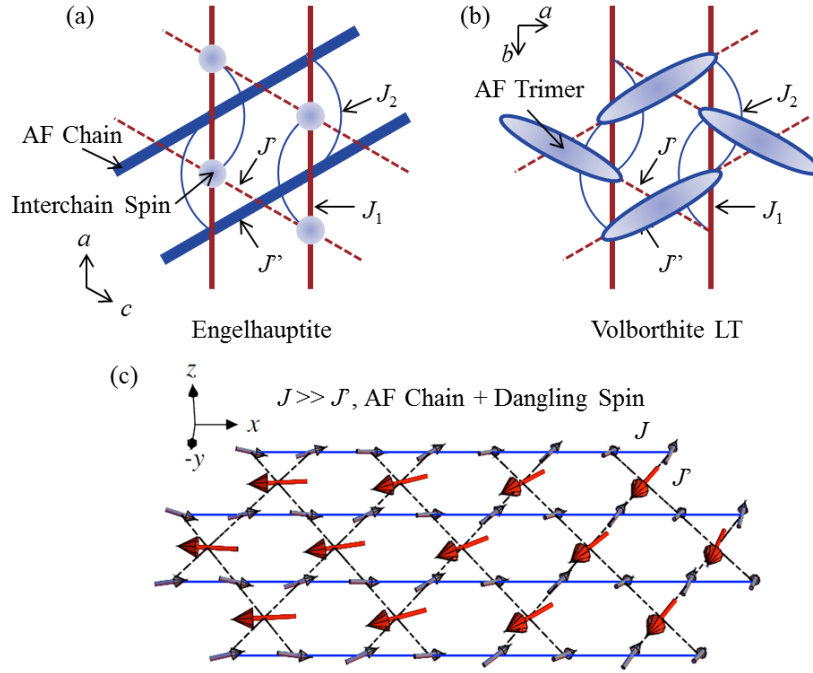


Figure 5.10. Spin models of (a) engelhauptite and (b) volborthite assuming $J' > |J_1|, J_2,$ and $|J'|$. (c) The spiral magnetic order expected in the anisotropic kagome lattice model with $J \gg J'$ [90].

5.5.3 Origin of large sample dependence in volborthite

Finally, I discuss the unusually large sample dependence of volborthite by considering the experimental results of engelhauptite together. As shown in the fig. 5.11(a), thick crystals of volborthite and engelhauptite shows the 1/3 plateaus above 30 T and the saturation behavior above 50 T, respectively. In the powder sample of volborthite, both of the characters, which correspond to the second and the third magnetization steps, are observed. The thin crystals also show the both characters although the magnetization curve is rather similar to that of the thick crystals. These magnetization curves appear that there are two magnetic components, volborthite-type and engelhauptite-type components, and the ratio of the two components change; volborthite thick crystals and the engelhauptite have only one of the two components and the thin crystals and the powder sample have both components in different ratio (fig. 5. 11(b)).

The structural analysis of volborthite suggests that there is a disorder in the direction of the interchain Cu1 orbital in the thin crystals and the powder sample. The orbital with different direction at Cu1 site should generate the engelhauptite-type component as the spin models of the two compounds are only distinguished by the orbital pattern of Cu1 site. Therefore, the large sample dependence found in volborthite would be attributed to the difference in the amount of the orbital disorder in the Cu1 site.

Note that if the orbitals with different directions are randomly distributed in the crystal structure, they should generate only one disordered component rather than the two components. The orbital disorder found in volborthite may not be randomly distributed but form a domain, where engelhauptite-type orbital order is formed. As a possible example, the layered order of the engelhauptite-type domain is depicted in the fig. 5.11(b).

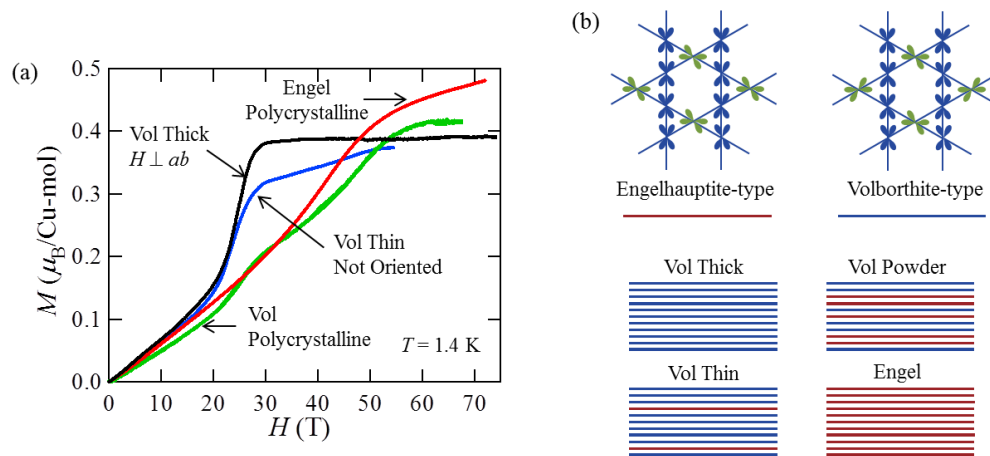


Figure 5.11. (a) The Magnetization curves of the powder sample of engelhauptite (engel) and different samples of volborthite (vol). (b) An example of the model to explain the large sample dependence found in the magnetization curves of volborthite.

5.6 Summary

- I have successfully synthesized powder and single crystal samples of engelhauptite. Synthetic engelhauptite has the monoclinic structure with the space group $P2_1/m$, which is different from the hexagonal structure of natural mineral. The orbital pattern is the same with the high temperature $C2/c$ structure of volborthite.
- Engelhauptite shows the magnetic order at 6 K and its magnetization curve shows saturation behavior around the 1/3 of the full magnetization above 50 T without the plateau region.

- The comparison of the structural and magnetic properties between engelhauptite and volborthite has provided the clues to understand their spin models. Engelhauptite is likely a frustrated spin system made of one-dimensional antiferromagnetic chain with strong intrachain interaction and coupled spins in between. The appropriate spin model for volborthite is considered to be the coupled trimer model rather than the coupled J_1 - J_2 chain model.
- The unusually large sample dependence of the magnetization curve observed in volborthite can be explained by the difference in the amount of orbital disorder.

Chapter 6. Topochemical pseudomorphosis and magnetic properties of vesignieite

6.1 Brief history and outline

Vesignieite $\text{BaCu}_3\text{V}_2\text{O}_8(\text{OH})_2$ is considered to be a rare realization of the spin 1/2 regular kagome antiferromagnet [47]. Two structural models with the monoclinic space group $C2/m$ and the trigonal space group $R-3m$ are proposed so far [46,88]. They are basically identical; there are kagome layers made of edge-sharing CuO_6 octahedra and they are separated by the VO_4 tetrahedra and the Ba^{2+} ions (fig. 6.1(a)). The kagome lattice is made of slightly distorted and undistorted triangles in the $C2/m$ and $R-3m$ models, respectively. It should be noted that the distortion of the kagome lattice found in the $C2/m$ model is less than 0.1% of the Cu-Cu bond lengths and whether the two structures are really different is questioned.

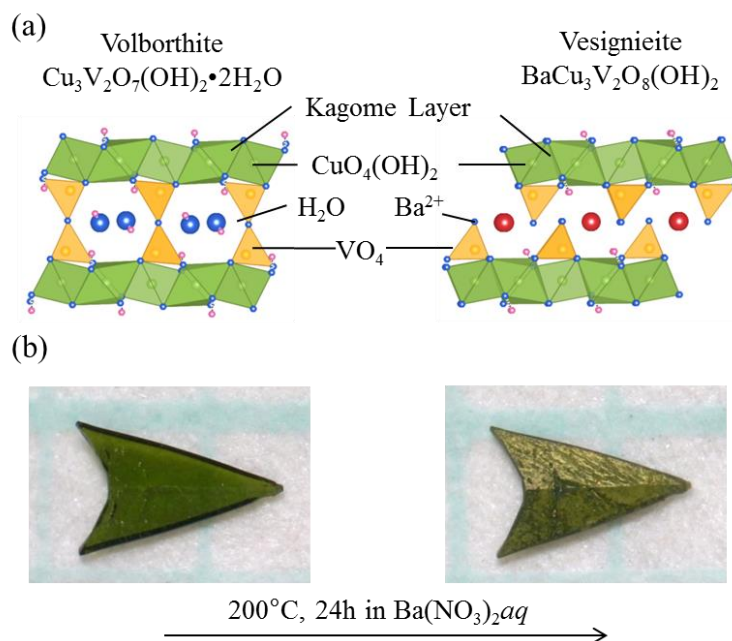


Figure 6.1. Schematic picture of the topochemical reaction from volborthite into vesignieite. (a) Crystal structure of volborthite (left) and vesignieite (right). (b) Crystals of volborthite before the reaction (left) and vesignieite after the reaction (right).

The antiferromagnetic long range order at $T_N = 9$ K is observed, which is approximately the 1/6 of the magnetic interaction of $J = 54$ K [47]. The ground state is suggested to be a 120° order with $q = 0$

instead of a spin liquid state expected for the spin 1/2 kagome antiferromagnet possibly due to the effect of DM interaction [89-90]. Although the basic magnetic properties are already known in previous studies using powder samples, there are some unusual features in vesignieite. One is the two-step nature of the magnetic order observed in the NMR measurements [89]; spatially inhomogeneous static moment appears below 13 K above T_N , which might be an unconventional order related to the geometrical frustration. Another is the 2/5 magnetization plateau-like behavior above 50 T reported in the powder sample [81]: the similar plateau-like behavior was also observed in the powder sample of another kagome compound volborthite, although it turned out to be the 1/3 plateau in the single crystal study of volborthite in this thesis. To clarify the magnetic properties of vesignieite, detailed study using high quality single crystal samples may be necessary.

I have successfully synthesized large quasi single crystals of vesignieite using the topochemical pseudomorphosis reaction of volborthite, which have similar layered structure to vesignieite (fig.6.1 (a) left). Using the thus obtained crystals, magnetic susceptibility measurements and the high-field magnetization measurements up to 72 T are performed and the spin structures are discussed.

6.2 Synthesis and elemental analysis

The crystal of vesignieite was topochemically obtained using the single crystal of volborthite as a starting material (fig. 6.1(b)). Several single crystals of volborthite were reacted with 0.5 g of $\text{Ba}(\text{NO}_3)_2$ (Raremetallic, 3N) at 200°C in 10 ml of pure H_2O . The reaction occurred in the entire crystal in 24 h. The crystals were further annealed at 550°C and 150 MPa in the H_2O sealed in an Au tubes to improve the crystallinity.

The crystals were examined by the ICP-AES experiment, which suggests the molar ratio Ba: Cu : V = 1 : 2.87 : 1.99. The result indicates that the amount of Ba ions inserted in the crystal is close to the ideal chemical formula of vesignieite. Moreover, there is likely a small amount of defect ~ 4% in the Cu site. As the elemental analysis data in the previous studies are not available, whether the defect is present or absent in the previous samples of vesignieite is unclear.

6.3 Structural analysis

The triangular plane of the crystal of volborthite before the reaction corresponds to the kagome plane. A crystal after the reaction is horizontally put on the sample plate and examined by the powder XRD experiments. The (00*l*) reflections ($l = n$ and $3n$ in the $C2/m$ and $R-3m$ models, respectively: $n = \text{integer}$) are selectively observed, indicating that the orientation of the kagome

plane is maintained during the reaction. Moreover, the powder pattern of the crashed crystals is quite similar to that expected for vesignieite. All of the peaks are indexed by the monoclinic unit cell with $a = 10.287(1) \text{ \AA}$, $b = 5.9373(4) \text{ \AA}$, $c = 7.7340(7) \text{ \AA}$, $\beta = 116.199(8)^\circ$ or trigonal unit cell with $a = 5.9387(3) \text{ \AA}$, $c = 20.8297(8) \text{ \AA}$; the differences between the powder pattern of the $C2/m$ and $R-3m$ models are very small and could not be distinguished in the measurement. Neither extra peaks nor the peaks of residual volborthite are observed, therefore, the crystal of volborthite is completely transformed into the crystal of vesignieite keeping the orientation of the kagome plane. The crystal can be called “vesignieite pseudomorph after volborthite” using the term of mineralogy.

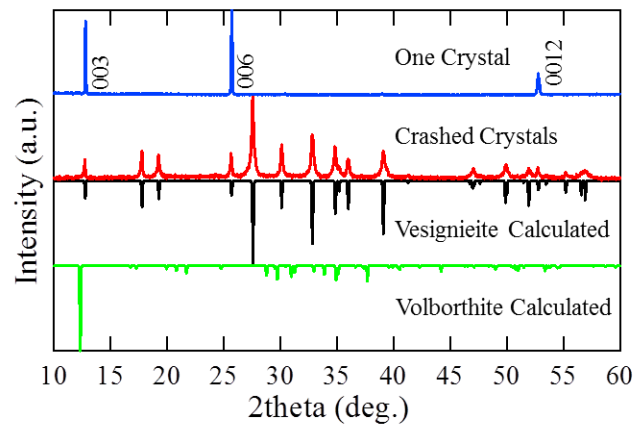


Figure 6.2. The powder XRD pattern of a crystal and crashed crystals of vesignieite obtained by the topochemical reaction (first and second row). The calculated powder pattern of vesignieite and volborthite are shown in the third and fourth row, respectively.

The crashed crystals of the size $\sim 0.1 \times 0.05 \times 0.02 \text{ mm}^3$ were studied using the single crystal X-ray diffractometer in ISSP at 293 K. The data can be analyzed either in the $C2/m$ model with $a = 10.2790(11) \text{ \AA}$, $b = 5.9380(5) \text{ \AA}$, $c = 7.7407(8) \text{ \AA}$, $\beta = 116.339(3)^\circ$ ($R1 = 0.0350$, $wR2 = 0.0664$, $S = 1.165$) or in the $R-3m$ model with $a = 5.9415(5) \text{ \AA}$, $c = 20.829(2) \text{ \AA}$ ($R1 = 0.0288$, $wR2 = 0.0565$, $S = 1.343$) (fig. 6.3(a)). The results are shown in the tables 6.1 and 6.2. To check the possible defects in the Cu sites, the occupancies of the Cu sites are refined as free parameters. The obtained Cu occupancies are 0.980 and 0.985 in the $C2/m$ and $R-3m$ models, respectively, suggesting the presence of $\sim 2\%$ of defect in the Cu site; the amount is smaller than that estimated from the ICP-AES experiment. The R values are slightly smaller in the refinements in the $R-3m$ model.

The Cu-Cu distances in the kagome lattice are 2.9677(2) and 2.9690(3) for Cu1-Cu2 and Cu2-Cu2 bonds, respectively; the difference is only 0.04% of the bond length. In the $R-3m$ model, Cu-Cu length is 2.9707(2). In both of the structural models, all of the Cu octahedra have the [2 + 4] coordination as shown in the table 6.3, indicating the $d_{3z^2-r^2}$ -type orbitals carry the spin 1/2. In the $R-3m$ model, the arrangement of the VO_4 group is disordered (fig. 6.3(b)), while they are ordered in the $C2/m$ model. However, the thermal ellipsoid of the O4 atom is unusually large, pointing to the structural disorder (fig. 6.3(a)). Therefore, the positional disorder of the VO_4 group is considered to be intrinsic to vesignieite. There is no particular reason to choose the $C2/m$ model and the $R-3m$ model appears to be reasonable.

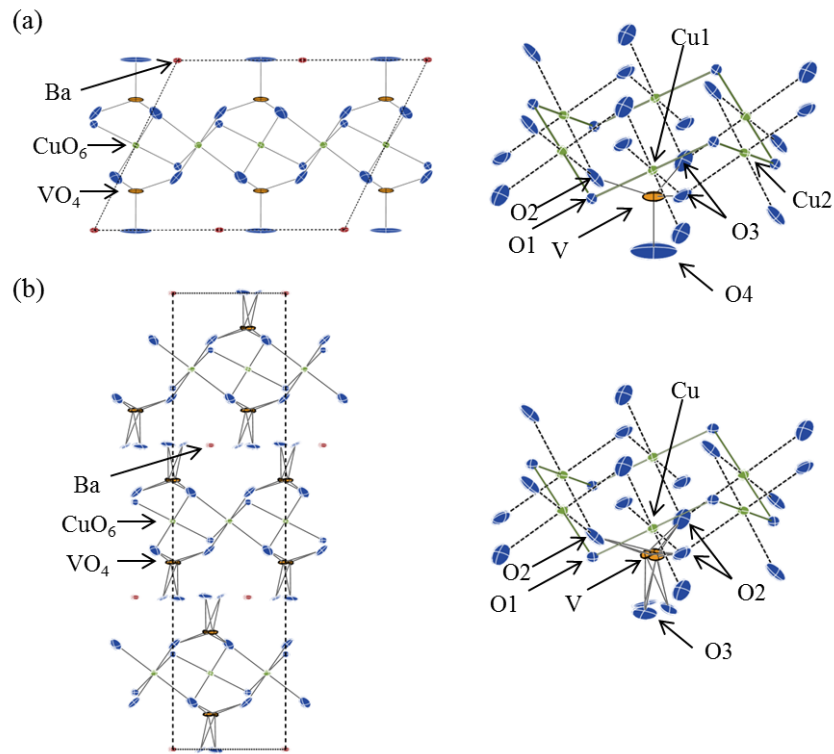


Figure 6.3. Crystal structures of vesignieite in (a) $C2/m$ and (b) $R-3m$ models depicted by the thermal ellipsoid, which describes the volume taken by 50% of the electrons of the atom. The V and O3 atoms are split into three sites assuming the disorder.

Table 6.1. Structural parameters of vesignieite at 293 K in the $C2/m$ model

Atom	x	y	z	U_{iso}	Occ.
Ba	0	0	0	0.0145(2)	1
Cu1	0	0	-0.5	0.0128(5)	0.980(8)
Cu2	-0.25	-0.25	-0.5	0.0127(4)	0.980(6)
V	0.4102(2)	0	0.2303(2)	0.0312(5)	1
O1	-0.2912(7)	-0.5	-0.3753(9)	0.0148(12)	1
O2	0.2753(8)	0	0.3092(12)	0.0336(18)	1
O3	0.5168(6)	-0.2409(9)	0.3096(8)	0.0337(14)	1
O4	0.3323(18)	0	-0.0051(14)	0.130(7)	1

Atom	U_{11}	U_{22}	U_{33}	U_{23}	U_{13}	U_{12}
Ba	0.0155(4)	0.0188(4)	0.0069(3)	0	0.0028(3)	0
Cu1	0.0125(8)	0.0170(8)	0.0096(8)	0	0.0056(6)	0
Cu2	0.0130(6)	0.0140(6)	0.0099(5)	-0.0012(4)	0.0041(4)	-0.0018(4)
V	0.0367(11)	0.0459(12)	0.0041(7)	0	0.0027(7)	0
O1	0.014(3)	0.016(3)	0.014(3)	0	0.006(2)	0
O2	0.014(3)	0.031(4)	0.037(4)	0	-0.005(3)	0
O3	0.041(3)	0.036(3)	0.032(3)	-0.021(2)	0.024(3)	-0.011(2)
O4	0.162(16)	0.185(18)	0.006(5)	0	0.004(7)	0

Table 6.2. Structural parameters of vesignieite at 293 K in the $R-3m$ model

Atom	x	y	z	U_{iso}	Occ.
Ba	0	0	0	0.0146(3)	1
Cu	-0.1667	0.1667	0.1667	0.0128(4)	0.985(7)
V	0.3129(14)	0.626(3)	0.07667(13)	0.014(3)	0.3333
O1	-0.3333	0.3333	0.1249(4)	0.0148(16)	1
O2	0.6543(12)	-0.1728(6)	0.1030(3)	0.0331(15)	1
O3	0.3774(14)	-0.245(3)	-0.0022(6)	0.035(5)	0.3333

Atom	U_{11}	U_{22}	U_{33}	U_{23}	U_{13}	U_{12}
Ba	0.0185(4)	0.0185(4)	0.0068(4)	0	0	0.00926(19)
Cu	0.0155(5)	0.0155(5)	0.0094(6)	-0.0007(2)	0.0007(2)	0.0091(5)
V	0.023(4)	0.009(5)	0.0044(9)	0.0016(14)	0.0008(7)	0.004(3)
O1	0.016(2)	0.016(2)	0.012(4)	0	0	0.0080(12)
O2	0.036(3)	0.033(2)	0.031(3)	0.0116(12)	0.023(2)	0.0179(17)
O3	0.059(9)	0.029(10)	0.008(6)	-0.011(5)	-0.006(3)	0.014(5)

Table 6.3 Cu-O bond lengths in vesignieite

<i>C2/m</i> model	Bond Length (Å)	<i>R-3m</i> model	Bond Length (Å)
Cu1-O1	1.924(6) × 2	Cu-O1	1.923(3) × 2
Cu1-O3	2.190(6) × 4	Cu-O2	2.194(5) × 4
Cu2-O1	1.917(4) × 2		
Cu2-O3	2.188(6) × 4		

6.4 Magnetic properties

The temperature dependence of the magnetic susceptibility is measured in the magnetic field of 1 T parallel and perpendicular to the kagome plane at 2-300 K (fig. 6.4(a)). The Curie-Weiss fitting at 150-300 K results $C = 0.483(16)$ and $0.513(17)$ cm³ K mol-Cu⁻¹ in $H // ab$ and $\perp ab$, respectively, $\theta = 71(5)$ K, and $\chi_0 = -3(3) \times 10^{-5}$ cm³ mol-Cu⁻¹. The fitting at 100-300 K by using the high-temperature series expansion for the $S = 1/2$ kagome antiferromagnet [91] results $J = 53.8(2)$ K, $g = 2.29(1)$ and $2.23(1)$, in $H \perp ab$ and $// ab$, respectively, and $\chi_0 = -3.3(4) \times 10^{-5}$ cm³ mol-Cu⁻¹. These values are consistent with the values reported in the previous studies.

Figures 6.4(c) and (d) show the magnetic susceptibility at low temperatures measured in $H // ab$ and $H \perp ab$ and 0.1-7 T. A kink is observed at 9 K in the field of 0.1 T, which suggests the magnetic order as already reported. At low temperature below 20 K, clear anisotropies are observed (fig. 6.4(b)). In $H \perp ab$, the magnetic susceptibility shows a broad peak, while it shows a steep increase in $H // ab$. It should be noted that this anisotropy is observed in the paramagnetic region above the magnetic order at 9 K, suggesting the development of the short-range antiferromagnetic correlation and the long range magnetic order is suppressed by the geometrical frustration.

Magnetization curves are measured at 1.8 and 20 K in the magnetic field of 0-7 T (figs. 6.5 (a) and (b)). In $H \perp ab$, the magnetizations curve shows an upturn at around 5 T. In $H // ab$, the magnetization shows a rapid increase at around 0.2 T and then increase linearly to the field at higher fields. There is a hysteresis in $H // ab$ at low fields, which is characteristic for the ferromagnetic moment. The linear fit at 5-7 T intercepts the magnetization axis at $1.8 \times 10^{-2} \mu_B$ mol-Cu⁻¹, which corresponds to the 1.6% of the full magnetic moment assuming $g = 2.23$. These results indicate that there is a weak-ferromagnetic moment only within the kagome plane with the magnetic order of vesignieite.

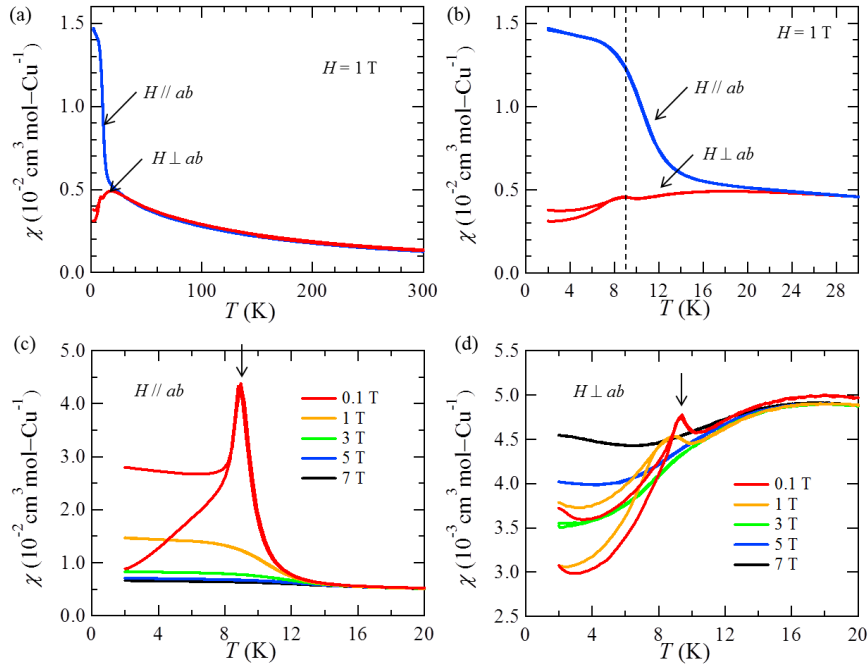


Figure 6.4. The magnetic susceptibility of vesignieite crystals in the magnetic field of 1 T at (a) 2-300 K and (b) 2-30 K and in various magnetic fields of 0.1-7 T in (b) $H // ab$ and (c) $H \perp ab$.

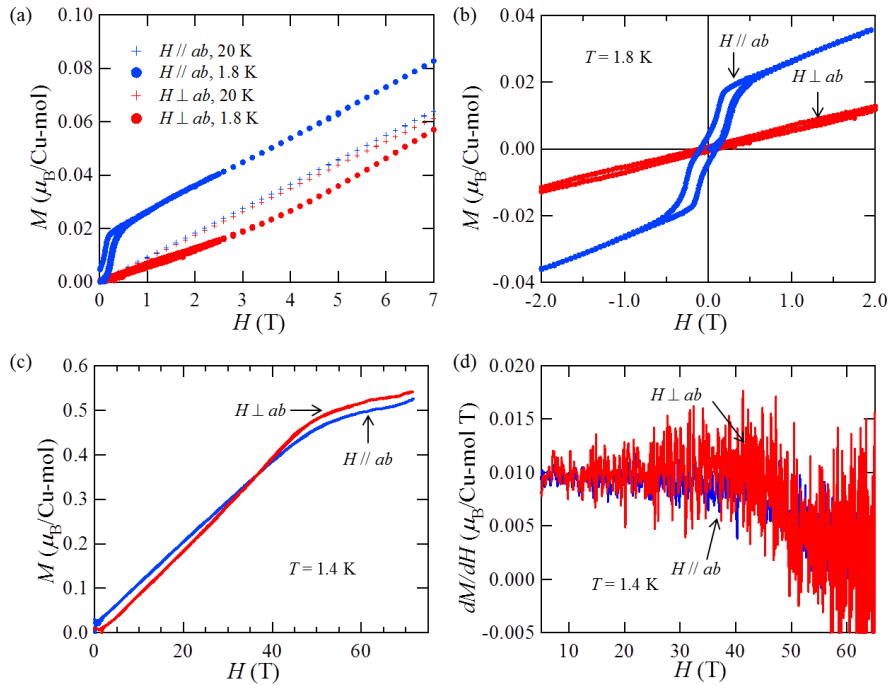


Figure 6.5. (a) Magnetization curves of vesignieite crystal at 1.8 and 20 K. (b) The magnetization curves in low fields at 1.8 K. (c) High-field magnetization curves of vesignieite at 1.4 K up to 72 T and (d) their field derivatives.

The magnetization curves are measured in $H // ab$ and $H \perp ab$ up to 72 T at 1.4 K (fig. 6.5(c)). In both of the field directions, magnetization increase monotonously up to 40 T and the slope of the magnetization curve becomes smaller at higher fields; the field derivative of the magnetization shown in the fig.6.5 (d) start to decrease there. The magnetization exceeds the 1/3 of the full moment at around 40 T. Neither the magnetization plateaus at the 1/9 and 1/3 of the full moment expected for the spin 1/2 kagome antiferromagnets nor the 2/5 plateau-like behavior observed in the powder samples are not observed in the topochemically obtained crystal samples.

6.5 Discussion

6.5.1 Magnetic structure and in-plane weak-ferromagnetic moment

First, I discuss the spin structure of vesignieite at low fields. In the magnetically ordered state, weak-ferromagnetic moment is observed only within the ab -plane. Possible origin of the weak-ferromagnetism is the DM interaction, which always exists in kagome lattice as there is no inversion center between the magnetic ions. In the regular kagome lattice, the directions of the D -vectors are restricted by the symmetry of the lattice as shown in fig. 6.6(a): there are both out-of-plane component (D_z) and the in-plane component (D_p). The D_z stabilizes the 120° order with magnetic moment within the kagome plane. Different 120° structures are stabilized depending on its sign; for $D_z > 0$ and $D_z < 0$, the 120° structures with vector chirality + and - are stabilized, respectively. The former and the latter are often called $q = 0$ and inverse triangular structures, respectively. There is an important difference between the two structures that the $q = 0$ structure preserve the 3-fold rotation symmetry, but the inverse triangular structure breaks the 3-fold rotation symmetry. On the other hand, the D_p causes the canting of the spin perpendicular to the kagome plane.

The general cases where both of the D_z and D_p are present in the classical spin kagome antiferromagnet are examined by Elhajal et al. and the expected ground state spin structures are shown in the fig. 6.6(b) [92]. In $D_z > 0$, the spin structure is always the $q = 0$ structure with the out-of-plane weak-ferromagnetic moment. In $D_z < 0$, the situation is not simple. In the case of small $D_z < 0$ and large D_p , the $q = 0$ structure with out-of-plane weak-ferromagnetic moment is selected as in the case of $D_z > 0$. If sizable $D_z < 0$ is present, the inverse triangular structure without out-of-plane component is selected.

The absence of the out-of-plane weak-ferromagnetic moment in vesignieite strongly suggests the presence of sizable $D_z < 0$, which select the inverse triangular structure without out-of-plane canting.

In the spin structure, the in-plane weak-ferromagnetic moment can appear in the presence of easy-axis magnetic anisotropy. For example, easy-axis anisotropy which acts to cant the magnetic moment toward the center of the hexagons can cause the canting of the spin as shown in the fig. 6.6(c). It should be noted that the $q = 0$ structure do not show the in-plane weak-ferromagnetic moment as long as the 3-fold rotational symmetry of the lattice is present.

The previous zero-field Cu-NMR experiments on the powder sample suggest the $q = 0$ state is realized in vesignieite [89]. The in-plane weak-ferromagnetic moment can appear in the $q = 0$ state if the kagome lattice is distorted as in the $C2/m$ model. However, it is difficult to explain the absence of the out-of-plane weak-ferromagnetic moment in the $q = 0$ structure as the non-zero D_p always causes the out-of-plane weak-ferromagnetism. Actually, the ESR experiments on the powder sample of vesignieite suggest the sizable D_p is present [90]. Re-examination of the spin structure by the NMR experiments using the topochemically obtained crystal sample, which should provide more information than the powder sample, may give the conclusive result on the spin structure of vesignieite. As far as I know, vesignieite would be the first realization of the inverse triangular structure in the quantum spin kagome magnets.

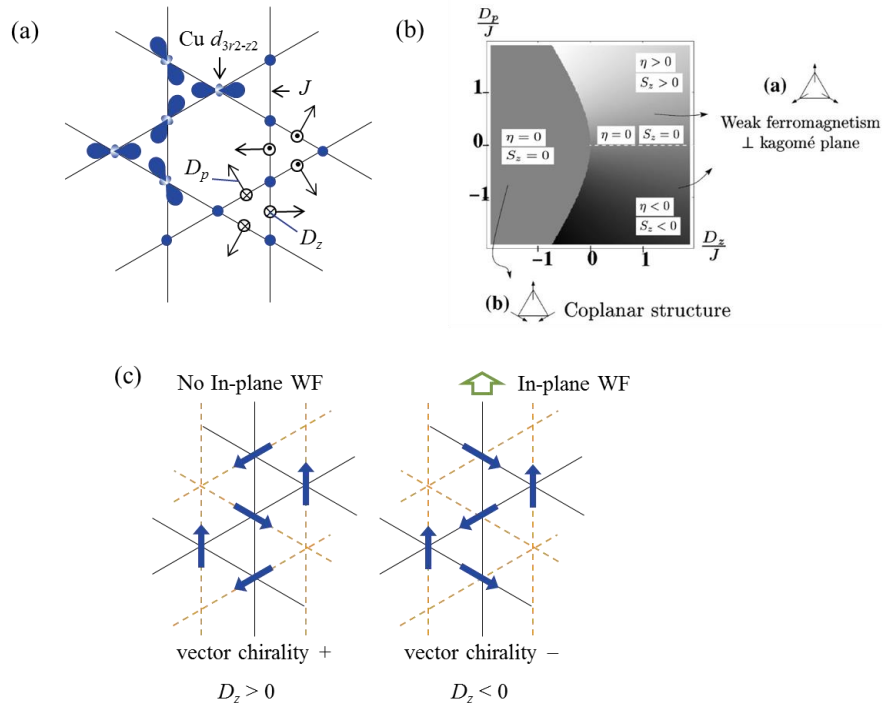


Figure 6.6. (a) Orbital arrangement and the magnetic interactions in the $R-3m$ model of vesignieite. (b) Spin structures of the classical kagome antiferromagnet stabilized in the presence of in-plane (D_p) and out-of-plane (D_z) DM interaction. (c) The 120° orders with the vector chirality + (so called

$q = 0$ structure, left) and vector chirality – (so called inverse triangular structure, right). In the former case, the spin structure has the 3-fold rotation symmetry and in-plane weak-ferromagnetism is absent. In the latter case, the spin structure breaks the 3-fold rotation symmetry and some easy-axis anisotropy can cause the in-plane weak-ferromagnetism: the anisotropy to cant the spin toward the center of the hexagons of the kagome lattice is assumed in the figure.

6.5.2 Magnetization process

Finally, I discuss the magnetization process of vesignieite. In $H // ab$, where weak-ferromagnetic moment is observed, the magnetization suddenly increases at around 0.2 T. This is understood by taking into account the inter-layer interaction. At zero magnetic field, if the magnetic moments in the next layer are coupled with weakly antiferromagnetic interaction, the net weak-ferromagnetic moment can be canceled out. At 0.2 T, the inter-layer coupling is considered to be overwhelmed by the magnetic field to generate the net weak-ferromagnetic moment.

In the magnetization curve in $H \perp ab$, a clear upturn is observed at around 5 T. This behavior is similar to the spin-flop transition, as it is not observed in another magnetic field direction. However, if the magnetic moments lie in the kagome plane due to the DM interaction, $H \perp ab$ is the magnetic field direction where spin-flop transition does not occur. Therefore, the upturn of the magnetization around 5 T is considered to be different from the spin-flop transition. A possible scenario is the gradual change of the spin structure from the canted inverse triangular structure at low fields to the canted $q = 0$ structure above 5 T (fig. 6.7). In vesignieite, the D_p , which stabilize the $q = 0$ structure with out-of-plane canting, is suggested to be relatively large in the ESR experiments [90]. The magnetization process may be understood that the D_p is large but not enough to stabilize the $q = 0$ structure at zero magnetic field and the magnetic field stabilize the canted $q = 0$ structure rather than the canted inverse triangular structure above 5 T.

At high-fields, the field derivative of the magnetization shows a clear decrease above 40 T, where the magnetization is approximately the 1/3 of the full moment; there must be a change in the spin structure there. On the analogy to the triangular lattice spin system, the stable spin structure at high fields is considered to be the canted coplanar 120° structure. The absence of the 1/9 and the 1/3 plateau phases in vesignieite suggests that the DM interactions have destroyed the plateau phases completely.

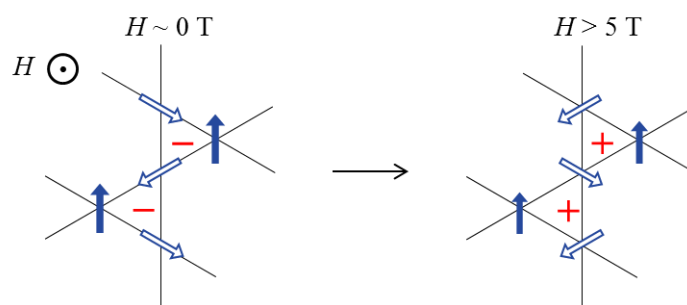


Figure 6.7. Possible spin structures of vesignieite at low magnetic fields viewed perpendicular to the kagome plane. The spins are expected to cant along the magnetic field accompanying in-plane rotation. The + and – indicate the positive and negative vector chirality.

6.6 Summary

- The quasi single crystals of vesignieite, which is almost perfect spin 1/2 kagome antiferromagnet, are successfully obtained via novel topochemical pseudomorphosis reaction of volborthite.
- The absence of out-of-plane weak-ferromagnetic moment and the presence of in-plane weak-ferromagnetic moment suggest the spin structure of vesignieite is inverse triangular structure with negative vector chirality rather than the $q = 0$ structure with positive vector chirality generated by the D_z and some magnetic anisotropy.
- At around 5 T in $H \perp ab$, the magnetization curve shows an anomaly which cannot be explained by conventional spin-flop transition. A possibility is the change of the spin structure from the canted inverse triangular structure to the canted $q = 0$ structure, which is stabilized by magnetic field and D_p .
- High field magnetization measurements revealed a magnetic anomaly at around 40 T, which must be the change of the spin structure. The 1/9 and 1/3 plateau phase are absent possibly due to the DM interaction.

Chapter 7. AMoOPO_4Cl ($A = \text{K}, \text{Rb}$): new candidates of the $S = 1/2$ J_1 - J_2 square lattice

7.1 Brief history and outline

The spin $1/2$ Heisenberg J_1 - J_2 square lattice model, where the NN interaction J_1 on the square lattice and the NNN interaction J_2 in the diagonal directions are considered (fig. 7. 1(a)), is a typical model of the frustrated magnets. The model is expected to show rich magnetic ground states depending on the sign and magnitude of J_1 and J_2 including the phases which are not fully understood [24]. In the case of $J_1 \gg J_2$, the ground state is the same with the normal square lattice model; the ferromagnetic and the Néel states are the ground state for $J_1 > 0$ and $J_1 < 0$, respectively. In the case of $J_2 \gg J_1$, the lattice is made of two interpenetrating square sub-lattices coupled by J_2 . For $J_2 > 0$ the classical ground state is the Néel states in each sub-lattices and their mutual orientation can be rotated freely. However, quantum fluctuations stabilize the spin configuration in which the spins of both sub-lattices becomes collinear (collinear antiferromagnetic state (CAF), fig. 7.1(b)) by the order-by-disorder mechanism.

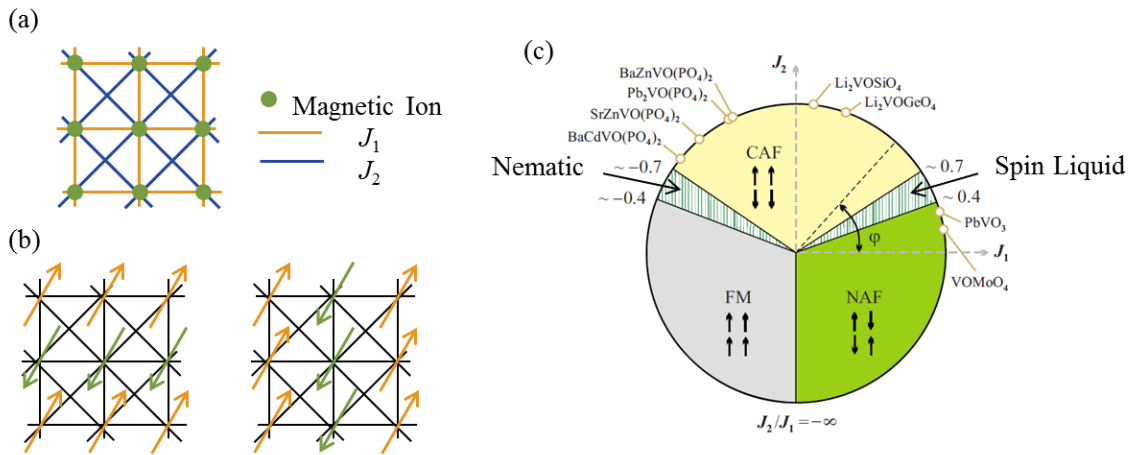


Figure 7.1. (a) The J_1 - J_2 square lattice model. (b) Two degenerate collinear antiferromagnetic states. (c) The ground state phase diagram of the J_1 - J_2 square lattice model [95]. The $J > 0$ and $J < 0$ indicate the antiferromagnetic and ferromagnetic interactions, respectively. The model compounds and their positions in the phase diagram are also shown.

The competition between J_1 and J_2 is expected to realize exotic ground states. The classical ground states are macroscopically degenerate at $|J_1| = 2J_2$ ($J_2 > 0$) and quantum fluctuation may

stabilize other states around $|J_1| = 2J_2$ depending on the sign of J_1 . For $J_1 > 0$, the ground state is expected to be a gapped spin liquid state [93]. For $J_1 < 0$, the spin nematic state, where the bound magnon pairs are generated and the order of the nematic director are formed, is expected to realize [25]. The nematic state is predicted in wide parameter range in magnetic field near magnetization saturation in $J_2 > |J_1|/2$ [94].

Although the model is extensively studied theoretically, its experimental realization is relatively rare. The model compounds are summarized in the fig. 7.1(c) by Nath et al. [95]. The J_2 is always antiferromagnetic, while the signs of J_1 and its relative magnitude to J_2 are strongly dependent on the materials. Therefore, studying new candidate materials are meaningful in search for novel magnetic phases. It should be noted that all the materials are vanadium oxide where the V^{4+} ions carry spin 1/2. I found that the known materials $AMoOPO_4Cl$ ($A = K, Rb$) [70] have the J_1 - J_2 square lattice, of which magnetic properties are not investigated so far. It is noted that the Mo^{5+} ions carry spin 1/2 in this compound: they are the first compound with 4d electron studied as a J_1 - J_2 square lattice magnet. The crystal structure is made of the layers where MoO_5Cl octahedra are connected by PO_4 tetrahedra and K^+ ions between them (fig. 7.2(a,b)). The structure can also be regarded that the layers made of MoO_5 square pyramids and PO_4 tetrahedra, which are similar to the vanadium oxides studied as the J_1 - J_2 magnets, are separated by the rock-salt type ACl layer. To clarify the magnetic properties of $AMoOPO_4Cl$ ($A = K, Rb$), I have synthesized single crystal sample of the materials and performed single crystal XRD, magnetization, and heat capacity measurements.

7.2 Synthesis

Single crystals of $AMoOPO_4Cl$ ($A = K, Rb$) were prepared by the salt flux method. MoO_3 , Mo , P_2O_5 , ACl ($A = K, Rb$), and $NaCl$ were mixed in the molar ratio of 5/3 : 1/3 : 1 : 30 : 30 and put in a Pt tube with 5 mm in diameter and 10 mm in length. As P_2O_5 is highly moisture absorbing, all the procedures were performed in the argon atmosphere glove box. The tube is sealed in an evacuated quartz tube and heated to 700°C in 7 hours and kept at the temperature for 1h, and then slowly cooled to 600°C in 50 h. The square plate shaped yellow crystals were obtained by removing the flux with pure H_2O (fig. 7.3). Unsuccessful attempts to fully substitute A-site with Tl or Cs and P-site with As were performed at 600-800 °C.

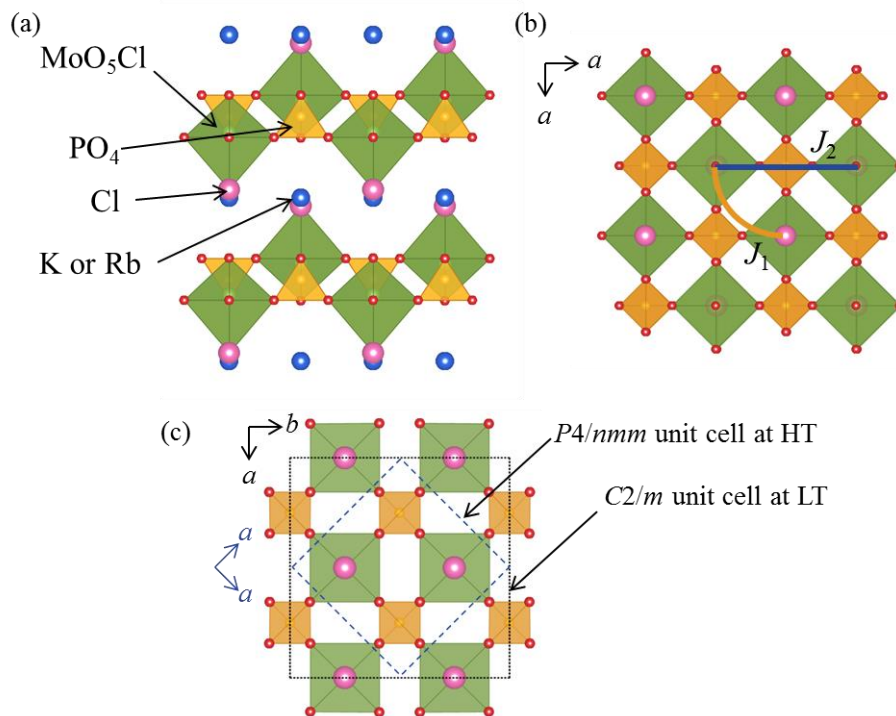


Figure 7.2. Crystal structures of AMoOPO_4Cl ($A = \text{K}, \text{Rb}$) seen from (a) a -axis and (b) c -axis. (c) Unit cells of the space group $P4/nmm$ at high temperature and $C2/m$ at low temperature of KMoOPO_4Cl .

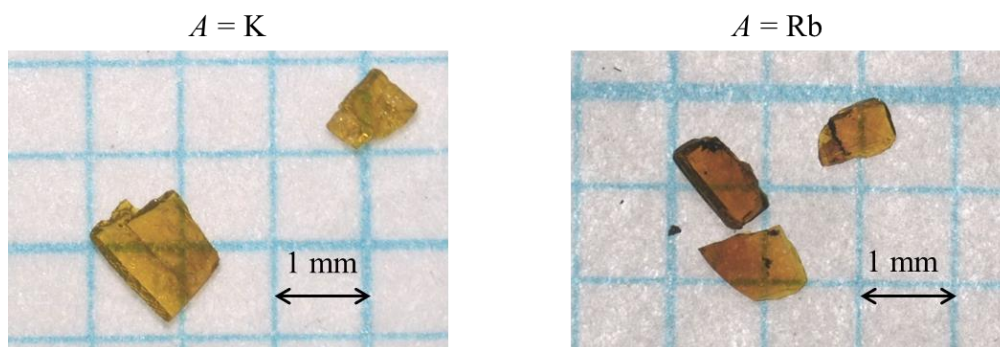


Figure 7.3. The single crystals of KMoOPO_4Cl (left) and $\text{RbMoOPO}_4\text{Cl}$ (right).

7.3 Structural analysis

The crystals of AMoOPO_4Cl ($A = \text{K}, \text{Rb}$) are investigated by the single crystal X-ray diffractometer in ISSP. The data obtained at 293 K are well refined by the structural models with the tetragonal space group $P4/nmm$ reported for both of K- and Rb- compounds (tables 7.1 and 7.2). The

results of the refinements for the K-compound is $a = 6.4362(3) \text{ \AA}$, $c = 7.2705(6) \text{ \AA}$ with $R1 = 0.0184$, $wR2 = 0.0504$, and $S = 1.352$ and for the Rb-compound is $a = 6.4586(3) \text{ \AA}$, $c = 7.4590(4) \text{ \AA}$ with $R1 = 0.0321$, $wR2 = 0.0784$, and $S = 1.336$.

A structural phase transition is found in the K-compound at around $T_s = 105 \text{ K}$; the magnetic susceptibility shows a small upturn around T_s as shown below (fig. 7.4(a)). To clarify the crystal structure below T_s , XRD measurement at 90 K is performed. The data suggests that the crystal has the monoclinic space group $C2/m$ with the unit cell of $a = 9.016(10) \text{ \AA}$, $b = 9.021(10) \text{ \AA}$, $c = 7.2468(8) \text{ \AA}$ and $\beta = 90.057(2)^\circ$ ($R1 = 0.0419$, $wR2 = 0.1550$, and $S = 1.282$). The $C2/m$ structure corresponds to the $\sqrt{2} \times \sqrt{2}$ super structure of the original $P4/nmm$ structure (fig. 7.2 (c)). The O2 site in the $P4/nmm$ structure splits into two sites O21 and O22 in the $C2/m$ structure. As a result of the structural phase transition, the NN interaction J_1 becomes two kinds at low temperatures. However, the structural changes caused by the phase transition are tiny as seen in the small difference between a and b of the unit cell and the small deviation of β from 90° . Therefore, I assume the magnitude of the two NN interactions are almost the same and analyzed the magnetic susceptibility data below assuming J_1 - J_2 square lattice model.

Table 7.1. Structural parameters of KMoOPO_4Cl at 293 K in the $P4/nmm$ model

Atom	x	y	z	U_{iso}	Occ.
K	0.75	0.25	0	0.0304(4)	1
Mo	0.75	0.75	0.40630(6)	0.01039(16)	1
P	0.75	0.25	0.5	0.0114(3)	1
Cl	0.75	0.75	0.0501(2)	0.0207(3)	1
O1	0.75	0.75	-0.3674(7)	0.0312(12)	1
O2	0.75	0.0622(3)	0.3705(3)	0.0187(5)	1

Atom	U_{11}	U_{22}	U_{33}	U_{23}	U_{13}	U_{12}
K	0.0291(5)	0.0291(5)	0.0329(8)	0	0	0
Mo	0.00803(18)	0.00803(18)	0.0151(3)	0	0	0
P	0.0074(4)	0.0074(4)	0.0195(6)	0	0	0
Cl	0.0225(5)	0.0225(5)	0.0170(6)	0	0	0
O1	0.0377(19)	0.0377(19)	0.018(2)	0	0	0
O2	0.0237(11)	0.0076(9)	0.0248(10)	-0.0019(8)	0	0

Table 7.2. Structural parameters of KMoOPO_4Cl at 90 K in the $C2/m$ model

Atom	x	y	z	U_{iso}	Occ.
K	0.5	0.25050(17)	0	0.0157(4)	1
Mo	0.74998(5)	0	0.40539(7)	0.0082(3)	1
P	0.5	0.25046(17)	0.5	0.0085(4)	1
Cl	0.74985(16)	0	0.0487(2)	0.0113(4)	1
O1	0.7495(6)	0	0.6327(8)	0.0189(11)	1
O21	0.5928(3)	0.3446(3)	0.6302(4)	0.0141(7)	1
O22	0.5917(3)	0.1561(3)	-0.6296(4)	0.0134(7)	1

Atom	U_{11}	U_{22}	U_{33}	U_{23}	U_{13}	U_{12}
K	0.0135(7)	0.0147(7)	0.0189(7)	0	0.0003(5)	0
Mo	0.0071(4)	0.0070(4)	0.0104(4)	0	0.0000(2)	0
P	0.0065(7)	0.0069(7)	0.0120(7)	0	0.0013(5)	0
Cl	0.0109(8)	0.0127(8)	0.0104(8)	0	-0.0004(5)	0
O3	0.025(3)	0.015(3)	0.017(2)	0	-0.0011(19)	0
O21	0.0121(16)	0.0154(15)	0.0149(15)	-0.0044(11)	-0.0001(11)	-0.0112(11)
O22	0.0111(15)	0.0133(15)	0.0157(15)	-0.0020(11)	0.0022(11)	0.0074(11)

Table 7.3. Structural parameters of $\text{RbMoOPO}_4\text{Cl}$ at 293 K in the $P4/nmm$ model

Atom	x	y	z	U_{iso}	Occ.
Rb	0.75	0.25	0	0.0212(4)	1
Mo	0.75	0.75	0.41070(9)	0.0064(3)	1
P	0.75	0.25	0.5	0.0069(5)	1
Cl	0.75	0.75	0.0622(3)	0.0159(5)	1
O1	0.75	0.75	-0.3669(10)	0.0218(16)	1
O2	0.75	0.0614(5)	0.3752(4)	0.0128(7)	1

Atom	U_{11}	U_{22}	U_{33}	U_{23}	U_{13}	U_{12}
Rb	0.0193(4)	0.0193(4)	0.0251(6)	0	0	0
Mo	0.0034(3)	0.0034(3)	0.0124(4)	0	0	0
P	0.0032(7)	0.0032(7)	0.0145(11)	0	0	0
Cl	0.0169(8)	0.0169(8)	0.0138(10)	0	0	0
O1	0.025(3)	0.025(3)	0.015(3)	0	0	0
O2	0.0165(17)	0.0035(14)	0.0185(14)	-0.0021(11)	0	0

7.4 Magnetic properties

The magnetic susceptibility measurements are performed using the crystals of $AMoOPO_4Cl$ ($A = K, Rb$) in magnetic fields parallel ($H // a$) and perpendicular ($H // c$) to the ab plane (fig. 7.4 (a)). The susceptibility is highly isotropic at high temperatures and shows a broad peak at 20 and 27 K in K- and Rb- compounds, respectively, which should correspond to the short range antiferromagnetic correlation. The Curie-Weiss fittings for K-compound at 120-300 K result $C = 0.348(2) \text{ cm}^3 \text{ K mol-Cu}^{-1}$, $\Theta = 26(1) \text{ K}$, and $\chi_0 = -4(1) \times 10^{-5} \text{ cm}^3 \text{ mol-Cu}^{-1}$ in $H // c$ and $C = 0.350(2) \text{ cm}^3 \text{ K mol-Cu}^{-1}$, $\Theta = 26(1) \text{ K}$, and $\chi_0 = -7(1) \times 10^{-5} \text{ cm}^3 \text{ mol-Cu}^{-1}$ in $H // ab$. For Rb-compound, similar fittings at 100-300 K result $C = 0.360(2) \text{ cm}^3 \text{ K mol-Cu}^{-1}$, $\Theta = 33(1) \text{ K}$, and $\chi_0 = -9(1) \times 10^{-5} \text{ cm}^3 \text{ mol-Cu}^{-1}$ in $H // c$ and $C = 0.362(2) \text{ cm}^3 \text{ K mol-Cu}^{-1}$, $\Theta = 32(2) \text{ K}$, and $\chi_0 = -6(1) \times 10^{-5} \text{ cm}^3 \text{ mol-Cu}^{-1}$ in $H // ab$. The Curie constants correspond to the effective magnetic moment $\mu_{\text{eff}} = 1.67 \mu_B$ for K- and $\mu_{\text{eff}} = 1.69 \mu_B$ Rb- compounds, which are quite close to the $\mu_{\text{eff}} = 1.73 \mu_B$ expected for $S = 1/2$. Therefore, these compounds can be regarded as ideal quantum spin systems. The Weiss temperatures suggest the antiferromagnetic interactions are dominant in both of the compounds.

At 6 K and 8 K in K- and Rb- compounds, respectively, anomaly is observed in the magnetic susceptibilities. In $H // c$, an upturn of the susceptibility is observed, while a small decrease is observed in $H // ab$. This anomaly should indicate an antiferromagnetic order with magnetic moment within the ab -plane. To extract more information from the magnetic susceptibility data, the fittings by using the high-temperature series expansion for the for the spin $1/2 J_1$ - J_2 square lattice model are performed [96]. The best fittings were obtained with $J_1 = -2 \text{ K}$, $J_2 = 19 \text{ K}$ for K-compound and $J_1 = -1 \text{ K}$, $J_2 = 29 \text{ K}$ for Rb-compound. These results indicate that the antiferromagnetic J_2 is dominant and J_1 is weakly ferromagnetic. The magnetic order is expected to be a collinear antiferromagnetic order with $M // ab$.

The heat capacity measurements are performed in zero magnetic field and magnetic fields perpendicular to the ab plane up to 9 T. At zero magnetic field, the heat capacity shows tiny kink at around 6 K and 8 K for K- and Rb- compounds, respectively, indicating that the entropy released with the magnetic transition is quite small. As increasing the magnetic field, on the other hand, a clear peak appears and the transition temperature increases. The appearance of the peak might indicate the change of the nature of the magnetic transition. Contrary to the naive expectation that the antiferromagnetic order is suppressed by the magnetic field, the transition temperatures are largely enhanced; the increase of the transition temperature at 9 T corresponds to the 20% of the transition temperature at zero field. The enhancement of the transition temperature is also observed

in the magnetic susceptibility measurements (figs. 7. 5(c) and (d)). The temperature of the minimum of the magnetic susceptibility observed in $H // c$ increases as the magnetic field is increased. It should be noted that the minimum is present slightly higher temperature of the peak temperature of C/T .

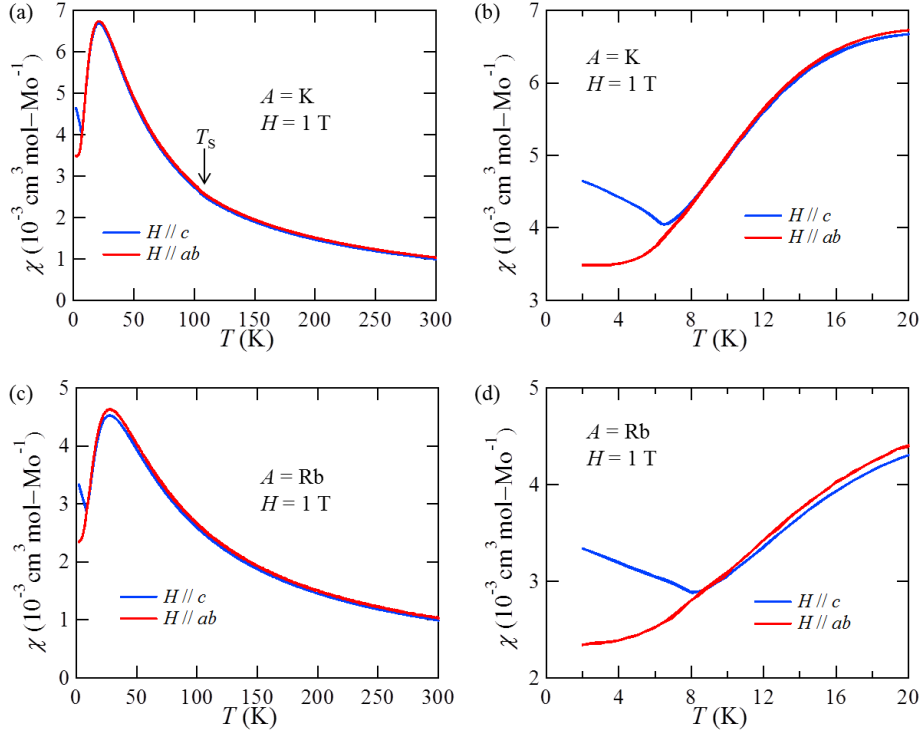


Figure 7.4. Magnetic susceptibility of the (a,b) KMoOPO_4Cl and (c,d) $\text{RbMoOPO}_4\text{Cl}$ in the magnetic field of 1 T.

7.5 Discussion

The phase diagram obtained from the magnetic susceptibility and heat capacity measurements are shown in fig. 7.6. In AMoOPO_4Cl ($A = \text{K, Rb}$), the feature of the Heisenberg spin systems with small easy plane anisotropy predicted in the numerical calculation for the square lattice system is detected in the magnetic susceptibility measurements; the magnetic susceptibility shows a minimum slightly above the transition temperature [97]. In the magnetic field, the spin fluctuation parallel to the magnetic field becomes smaller and enhances the effective easy-plane anisotropy. Therefore, the increase of the transition temperature in magnetic field is likely caused by the enhanced effective easy-plane anisotropy by the magnetic field, which would lead to the development of magnetic

correlation at higher temperatures. The similar XY-spin like behavior is also reported in square lattice antiferromagnets $\text{Sr}_2\text{CuO}_2\text{Cl}_2$ [98], $[\text{Cu}(\text{pyz})_2(\text{pyO})_2](\text{PF}_6)_2$ [99], and $\text{Cu}(\text{pz})_2(\text{ClO}_4)_2$ [100] and J_1 - J_2 square lattice magnet $\text{Pb}_2\text{VO}(\text{PO}_4)_2$ [101].

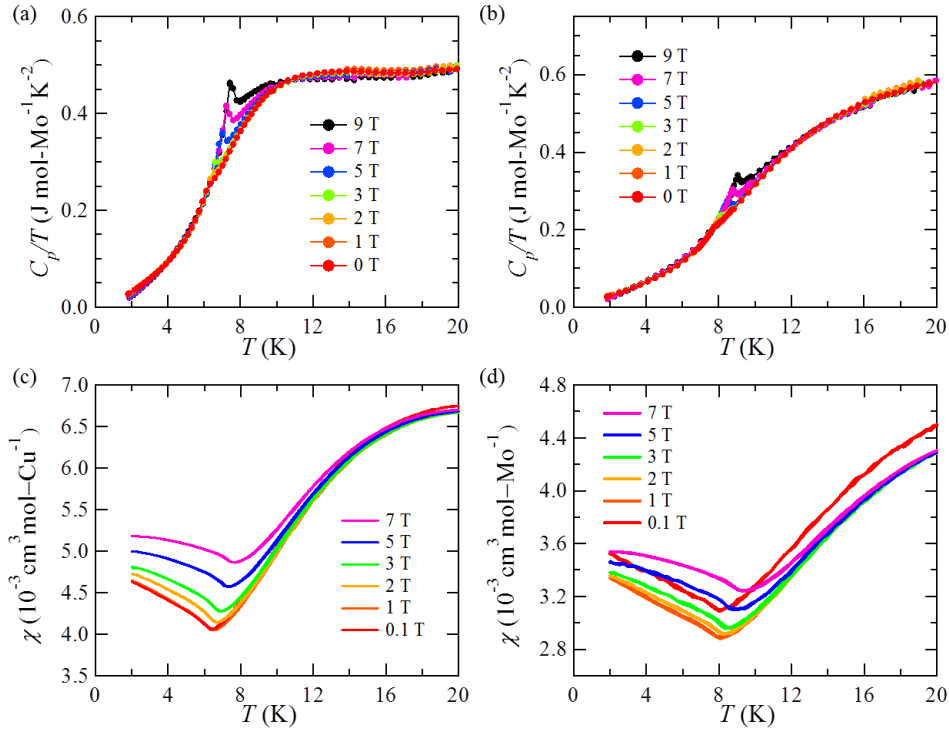


Figure 7.5. Heat capacities of (a) KMoOPO_4Cl and (b) $\text{RbMoOPO}_4\text{Cl}$ in the magnetic field of 0-9 T. Magnetic susceptibilities of (c) KMoOPO_4Cl and (d) $\text{RbMoOPO}_4\text{Cl}$ in the magnetic field of 0.1-7 T.

The unique character of AMoOPO_4Cl ($A = \text{K}, \text{Rb}$) is the much larger J_2 compared to J_1 . The J_2 is larger than those in the vanadium analogues which typically have $J_2 < 10$ K although the J_1 has the similar magnitude. Due to the condition $J_2 \gg |J_1|$, there are two interpenetrating ideal spin 1/2 square lattice antiferromagnets with J_2 , which are weakly coupled by ferromagnetic J_1 . The peculiar magnetic field dependences of the heat capacity might be related to this unique situation. Moreover, the ratio $|J_2/J_1|$ turned out to be very sensitive to the lattice constants; 9.5 and 29 in K- and Rb-compounds, respectively. Further compressing the system by chemical or physical pressure would make the system more frustrated and lead to the finding of novel magnetic phases.

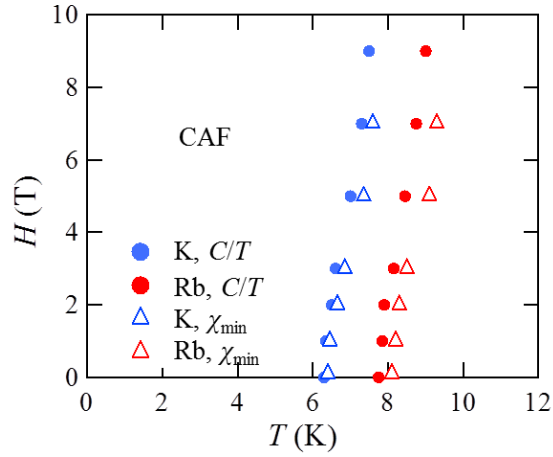


Figure 7.6. Magnetic phase diagram of AMoOPO_4Cl ($A = \text{K, Rb}$).

7.6 Summary

- AMoOPO_4Cl ($A = \text{K, Rb}$) are the new spin $1/2$ J_1 - J_2 square lattice systems with strongly antiferromagnetic J_2 and weakly ferromagnetic J_1 .
- The unique situation where two interpenetrating ideal spin $1/2$ square lattices with large antiferromagnetic intralayer coupling J_2 are very weakly coupled by J_1 is realized.

Overall summary

I summarize achievements in the thesis and state the perspective for the future studies.

I have succeeded in the synthesis of large and high-quality single crystals of volborthite $\text{Cu}_3\text{V}_2\text{O}_7(\text{OH})_2 \cdot 2\text{H}_2\text{O}$ and pure polycrystalline sample of engelhauptite $\text{KCu}_3\text{V}_2\text{O}_7(\text{OH})_2\text{Cl}$ by the hydrothermal method for the first time. Crystal structures of synthetic volborthite and engelhauptite are clarified to find novel crystal structures with various orbital patterns and a structural phase transition between them (orbital flipping transition). As a result of structural analyses, cooperative order and disorder of Jahn-Teller distortion of CuO_6 octahedra, tilting of V_2O_7 tetrahedral pillars, and arrangement of intercalants are found. Moreover, I have demonstrated the topochemical pseudomorphosis reactions of volborthite into engelhauptite and vesignieite $\text{BaCu}_3\text{V}_2\text{O}_8(\text{OH})_2$ under hydrothermal condition. Utilizing topochemical pseudomorphosis reaction would accelerate the material exploitation in the field of frustrated magnetism as well as other field of material science.

The H - T phase diagram of volborthite with distorted kagome lattice is obtained by the magnetic properties measurements on the single crystal sample. The $1/3$ plateau and the novel phase just below the plateau phase (phase N) are discovered. The phase N has steep change of magnetization linearly to the magnetic field and large magnetic entropy. I propose the realization of the spin nematic state in the phase N as a result of competing ferromagnetic and antiferromagnetic interactions. By studying the magnetic properties of engelhauptite, which has closely related crystal structure to volborthite, clues to understand their complex magnetization processes and information on their appropriate spin models are obtained.

Moreover, I have studied the magnetic properties of almost perfect kagome compound vesignieite using the topochemically obtained quasi single crystals. Based on the results of magnetic anisotropy measurements and structural considerations, I propose that the 120° spin structure with the negative vector chirality, which would be the first realization in the quantum spin kagome antiferromagnets, is stabilized by the DM interaction at low magnetic fields. At high magnetic fields, theoretically predicted magnetization plateaus were not present and are considered to be destabilized by the DM interactions.

Further studies to clarify the nature of phase N of volborthite are necessary and there is a chance of observing unconventional magnetic properties related to the spin nematic states. Moreover, studying the couplings between the unique magnetic orders found in kagome copper minerals and other physical properties would be a challenging future work. On the other hand, to realize the spin liquids and magnetization plateau phases predicted in the ideal spin $1/2$ kagome antiferromagnet, evading

the DM interaction, of which magnitude is roughly proportional to the deviation of the g -value from 2, is crucial, but is considered to be difficult in copper based compounds. Discoveries of non-copper kagome materials are necessary. The d^1 compounds with V^{4+} and Mo^{5+} etc. in a square pyramidal coordination are worth exploiting as they could realize the ideal spin 1/2 systems.

In summary, I have studied frustrated magnets mainly kagome copper minerals by synthesizing high-quality crystals in order to find novel magnetic phases or magnetic orders related to the magnetic frustration. Actually, magnetic field induced phase transitions and novel magnetic phases in volborthite are discovered and information on the vector chirality in the magnetic order of vesignieite is obtained. Especially interesting is the novel magnetic phase of volborthite that is considered to be the spin nematic phase. Further studies on the discovered magnetic phases and new target materials presented in this work would show the new directions of the experimental study of frustrated magnetism. Moreover, various orbital patterns and the orbital flipping transition discovered in volborthite and engelhauptite have expanded the richness of the crystal chemistry of copper minerals: obtained structure-property relationship would contribute to the future material exploitation in the field of magnetism.

References

- [1] 上田和夫, “磁性入門”, 裳華房 (2011).
- [2] 久保健, 田中秀数, “磁性 I”, 朝倉書店 (2008).
- [3] C. Lacroix, P. Mendels, and F. Mila, “Introduction to Frustrated Magnetism: Materials, Experiments, Theory”, Springer (2011).
- [4] B. Bernu, C. Lhuillier, and L. Pierre, *Phys. Rev. Lett.* 69, 2590 (1992).
- [5] L. Capriotti, A. E. Trumper, and S. Sorella, *Phys. Rev. Lett.* 82, 3899 (1999).
- [6] S. Yan, D. A. Huse, and S. R. White, *Science* 332, 1173 (2011).
- [7] S. Depenbrock, I. P. McCulloch, and U. Schollwock, *Phys. Rev. Lett.* 109, 067201 (2012).
- [8] H-C. Jiang, Z. Wang, and L. Balents, *Nat. Phys.* 8, 902 (2012).
- [9] Y. Iqbal, F. Becca, S. Sorella, and D. Poilblanc, *Phys. Rev. B* 87, 060405 (2013).
- [10] R. R.P. Singh and D. A. Huse, *Phys. Rev. B* 76, 180407 (2007).
- [11] L. Balents, *Nature* 464, 199 (2010).
- [12] K. Hida, *J. Phys. Soc. Jpn.* 70, 3673 (2001).
- [13] S. Nishimoto, N. Shibata, and C. Hotta, *Nat. Commun.* 4, 2287 (2013).
- [14] S. Capponi, O. Derzhko, A. Honecker, A. M. Läuchli, and J. Richter, *Phys. Rev. B* 88, 144416 (2013).
- [15] T. Picot, M. Ziegler, R. Orus, and D. Poilblanc, arXiv:1508.07189 (2015).
- [16] M. P. Shores, E. A. Nytko, B. M. Bartlett, and D. G. Nocera, *J. Am. Chem. Soc.* 127, 13462 (2005).
- [17] J. S. Helton, K. Matan, M. P. Shores, E. A. Nytko, B. M. Bartlett, Y. Yoshida, Y. Takano, A. Suslov, Y. Qiu, J.-H. Chung, D. G. Nocera, and Y. S. Lee, *Phys. Rev. Lett.* 98, 107204 (2007).
- [18] P. Mendels, F. Bert, M. A. de Vries, A. Olariu, A. Harrison, F. Duc, J. C. Trombe, J. S. Lord, A. Amato, and C. Baines, *Phys. Rev. Lett.* 98, 077204 (2007).
- [19] T. H. Han, J. S. Helton, S. Chu, D. G. Nocera, J. A. Rodriguez-Rivera, C. Broholm, and Y. S. Lee, *Nature* 492, 406 (2012).
- [20] T. H. Han, R. Chisnell, C. J. Bonnoit, D. E. Freedman, V. S. Zapf, N. Harrison, D. G. Nocera, Y. Takano, and Y. S. Lee, arXiv:1402.2693 (2014).
- [21] R. R. P. Singh, *Phys. Rev. Lett.* 104, 177203 (2010).
- [22] H. Kawamura, K. Watanabe, and T. Shimokawa, *J. Phys. Soc. Jpn.* 83, 103704 (2014)
- [23] M. Fu, T. Imai, T. H. Han, Y. S. Lee, *Science* 350, 655 (2015).
- [24] N. Shannon, B. Schmidt, K. Penc, P. Thalmeier, *Eur. Phys. J. B* 38, 599 (2004).

- [25] N. Shannon, T. Momoi, and P. Sindzingre, *Phys. Rev. Lett.* 96, 027213 (2006).
- [26] T. Hikihara, L. Kecke, T. Momoi, and A. Furusaki, *Phys. Rev. B* 78, 144404 (2008).
- [27] H. T. Ueda, and T. Momoi, *Phys. Rev. B* 87, 144417 (2013).
- [28] J. Sudan, A. Lüscher, and A. M. Läuchli, *Phys. Rev. B* 80, 140402 (2009).
- [29] M. Enderle, C. Mukherjee, B. Fåk, R. K. Kremer, J. M. Broto, H. Rosner, S. L. Drechsler, J. Richter, J. Malek, and A. Prokofiev, *Europhys. Lett.* 70, 237 (2005).
- [30] L. E. Svistov, T. Fujita, H. Yamaguchi, S. Kimura, K. Omura, A. Prokofiev, A. I. Smirnov, Z. Honda, and M. Hagiwara, *JETP Lett.* 93, 21 (2011).
- [31] N. Büttgen, K. Nawa, T. Fujita, M. Hagiwara, P. Kuhns, A. Prokofiev, A. P. Reyes, L. E. Svistov, K. Yoshimura, and M. Takigawa, *Phys. Rev. B* 90, 134401 (2014).
- [32] Y. Mizuno, T. Tohyama, S. Maekawa, T. Osafune, N. Motoyama, H. Eisaki, and S. Uchida, *Phys. Rev. B* 57, 5326 (1998).
- [33] D. G. Nocera, B. M. Bartlett, D. Grohol, D. Papoutsakis, and M. P. Shores, *Chem. Eur. J.* 10, 3850 (2004).
- [34] S. K. Pati, and C. N. R. Rao, *Chem. Commun.*, 39, 4683 (2008).
- [35] T. H. Han, J. Singleton, and J. A. Schlueter, *Phys. Rev. Lett.* 113, 227203 (2014).
- [36] T. M. McQueen, T. H. Han, D. E. Freedman, P. W. Stephens, Y. S. Lee, and D. G. Nocera, *J. Solid State Chem.* 184 3319 (2011).
- [37] B. Fåk, E. Kermarrec, L. Messio, B. Bernu, C. Lhuillier, F. Bert, P. Mendels, B. Koteswararao, F. Bouquet, J. Ollivier, A. D. Hillier, A. Amato, R. H. Colman, and A. S. Wills, *Phys. Rev. Lett.* 109, 037208 (2012).
- [38] D. Boldrin, B. Fåk, M. Enderle, S. Bieri, J. Ollivier, S. Rols, P. Manuel, and A. S. Wills, *Phys. Rev. B* 91, 220408(R) (2015).
- [39] W. Sun, Y. X. Huang, Y. Pan, J. X. Mi, J. X., *Phys. Chem. Miner.*, 1 (2015).
- [40] E. A. Nytko, M. P. Shores, J. S. Helton, and D. G. Nocera, *Inorg. Chem.* 48, 7782 (2009).
- [41] P. Elliott, J. Brugger, and T. Caradoc-Devies, *Mineral. Mag.* 74, 39 (2010).
- [42] M. Fujihala, X. G. Zheng, H. Morodomi, T. Kawae, A. Matsuo, K. Kindo, and I. Watanabe, *Phys. Rev. B* 89, 100401(R) (2014).
- [43] R. Basso, A. Palenzona, and L. Zefiro, *Neues Jahrb. Miner. Monatsh.* 9, 385 (1988).
- [44] Z. Hiroi, M. Hanawa, N. Kobayashi, M. Nohara, H. Takagi, Y. Kato, and M. Takigawa, *J. Phys. Soc. Jpn.* 70, 3377 (2001).

- [45] I. V. Pekov, O. I. Siidra, N. V. Chukanov, V. O. Yapaskurt, S. N. Britvin, S. V. Krivovichev, W. Schüller, and B. Ternes, *Mineral. Mag.* 77, 2695 (2013).
- [46] M. Zhesheng, H. Ruilin, and Z. Xiaoling, *Acta Geologica Sinica* 4, 145 (1991).
- [47] Y. Okamoto, H. Yoshida, and Z. Hiroi, *J. Phys. Soc. Jpn.* 78, 3377 (2009).
- [48] D. Boldrin, and A. S. Wills, *J. Mater. Chem. C* 3, 4308 (2015).
- [49] S. Ghose, and C. Wan, *Acta Cryst.* B35, 819 (1979).
- [50] H. Effenberger, *Z. Kristallogr.* 188, 43 (1989).
- [51] G. J. Nilsen, Y. Okamoto, H. Ishikawa, V. Simonet, C. V. Colin, A. Cano, L. C. Chapon, T. Hansen, H. Mutka, and Z. Hiroi, *Phys. Rev. B* 89, 140412(R) (2014).
- [52] M. Fujihala, X. G. Zheng, Y. Oohara, H. Morodomi, T. Kawae, Akira Matsuo, and Koichi Kindo, *Phys. Rev. B* 85, 012402 (2012).
- [53] U. Hålenius, F. Hatert, M. Pasero, and S. J. Mills, *Mineral. Mag.* 79, 247 (2015).
- [54] T. Dordevic, and L. Karanovic, *Acta Cryst.* C69, 114 (2013).
- [55] D. E. Freedman, R. Chisnell, T. M. McQueen, Y. S. Lee, C. Payen, and D. G. Nocera, *Chem. Commun.* 48, 64 (2012).
- [56] X. Turrillas, C. Laviron, H. Vincent, J. Pannetier, and J. C. Joubert, *J. Solid State Chem.* 67, 297 (1987).
- [57] T. Söhnel, P. Böttcher, W. Reichelt, and F. e. Wagner, *Cheminform*, 29 (1998).
- [58] N. Henry, L. Burylo-Dhuime, F. Abraham, O. Mentré, *Solid State Science* 4, 1023 (2002).
- [59] S. Hara, H. Sato, and Y. Narumi, *J. Phys. Soc. Jpn.* 81, 073707 (2012).
- [60] M. S. Williams, J. P. West, and S. J. Hwu, *Chem. Mater.* 26, 1502 (2014).
- [61] U. Englich, C. Frommen, and W. Massa, *J. Alloy. Compd.* 246, 155 (1997).
- [62] M. Müller, and B. G. Müller, *Z. Anorg. Allg. Chem.* 621, 993 (1995).
- [63] F. H. Aidoudi, D. W. Aldous, R. J. Goff, A. M. Z. Slawin, J. P. Attfield, R. E. Morris, and P. Lightfoot, *Nat. Chem.* 3, 801 (2011).
- [64] J. Darriet, M. Ducau, M. Feist, A. Treassaud, and P. Hagenmuller, *J. Solid State Chem.* 98, 379 (1992).
- [65] L. Jahnberg, *Mater. Res. Bull.* 16, 513 (1981).
- [66] B. Willenberg, M. Schäpers, K. C. Rule, S. Süllow, M. Reehuis, H. Ryll, B. Klemke, K. Kiefer, W. Schottenhamel, B. Büchner, B. Ouladdiaf, M. Uhlarz, R. Beyer, J. Wosnitza, and A. U. B. Wolter, *Phys. Rev. Lett.* 108, 117202 (2012).
- [67] M. Hase, H. Kuroe, K. Ozawa, O. Suzuki, H. Kitazawa, G. Kido, and T. Sekine, *Phys. Rev. B* 70, 104426 (2004).

- [68] M. Pregelj, A. Zorko, O. Zaharko, H. Nojiri, H. Berger, L. C. Chapon, and D. Arçon, *Nat. Commun.* 6, 7255 (2015).
- [69] R. Melzi, P. Carretta, A. Lascialfari, M. Mambrini, M. Troyer, P. Millet, and F. Mila, *Phys. Rev. Lett.* 85, 1318 (2000).
- [70] M.M. Borel, A. Leclaire, J. Chardon, J. Provost, and B. Raveau, *J. Solid State Chem.* 137, 214 (1998).
- [71] F. Izumi, and K. Momma, *Solid State Phenomena* 130, 15 (2007).
- [72] G. M. Sheldrick, *Acta Cryst. C* 71, 3 (2015).
- [73] M. A. Lafontaine, A. L. Bail, G. Férey, *J. Solid State Chem.* 85, 220 (1990).
- [74] A. A. Kashaev, I. V. Rozhdestvenskaya, I. I. Bannova, A. N. Sapozhnikov, and O. D. Glebova, *J. Struct. Chem.* 49, 708 (2008).
- [75] H. Yoshida, J. Yamaura, M. Isobe, Y. Okamoto, G. J. Nilsen, and Z. Hiroi, *Nat. Commun.* 3, 860 (2012).
- [76] P. Y. Zavalij, F. Zhang, and M. S. Whittingham, *Acta Cryst.*, C53, 1738 (1997).
- [77] M. Yoshida, M. Takigawa, H. Yoshida, Y. Okamoto, and Z. Hiroi, *Phys. Rev. Lett.* 103, 077207 (2009).
- [78] H. Yoshida, Y. Okamoto, T. Tayama, T. Sakakibara, M. Tokunaga, A. Matsuo, Y. Narumi, K. Kindo, M. Yoshida, M. Takigawa, and Z. Hiroi, *J. Phys. Soc. Jpn.* 78, 043704 (2009).
- [79] M. Yoshida, M. Takigawa, H. Yoshida, Y. Okamoto, and Z. Hiroi, *Phys. Rev. B* 84, 020410 (2011).
- [80] M. Yoshida, M. Takigawa, S. Krämer, S. Mukhopadhyay, M. Horvatić, C. Berthier, H. Yoshida, Y. Okamoto, and Z. Hiroi, *J. Phys. Soc. Jpn.* 81, 024703 (2012).
- [81] Y. Okamoto, M. Tokunaga, H. Yoshida, A. Matsuo, K. Kindo, and Z. Hiroi, *Phys. Rev. B* 83, 180407 (2011).
- [82] F. Bert, D. Bono, P. Mendels, F. Ladieu, F. Duc, J.-C. Trombe, and P. Millet, *Phys. Rev. Lett.* 95, 087203 (2005).
- [83] H Ohta, W. Zhang, S. Okubo, M. Tomoo, M. Fujisawa, H. Yoshida, Y. Okamoto, and Z. Hiroi, *J. Phys.: Conf. Ser.* 145, 012010 (2009).
- [84] T. Sakakibara, H. Mitamura, T. Tayama, and H. Amitsuka, *Sakakibara, Jpn. J. appl. Phys.* 33, 5067 (1994).
- [85] O. Janson, J. Richter, P. Sindzingre, and H. Rosner, *Phys. Rev. B* 82, 104434 (2010).

- [86] O. Janson, S. Furukawa, T. Momoi, P. Sindzingre, J. Richter, K. Held, arXiv:1509.07333 (2015).
- [87] A. P. Schnyder, O. A. Starykh, and L. Balents, Phys. Rev. B 78, 174420 (2008).
- [88] H. Yoshida, Y. Michiue, E. Takayama-Muromachi, and M. Isobe, J. Mater. Chem. 22, 18793 (2012).
- [89] M. Yoshida, Y. Okamoto, M. Takigawa, and Z. Hiroi, J. Phys. Soc. Jpn. 82, 013702 (2013).
- [90] A. Zorko, F. Bert, A. Ozarowski, J. van Tol, D. Boldrin, A. S. Wills, and P. Mendels, Phys. Rev. B 88, 144419 (2013).
- [91] N. Elstner and A. P. Young, Phys. Rev. B 50, 6871 (1994).
- [92] M. Elhajal, B. Canals, and C. Lacroix, Phys. Rev. B 66, 014422 (2002).
- [93] H. C. Jiang, H. Yao, and L. Balents, Phys. Rev. B 86, 024424 (2012).
- [94] H. T. Ueda, J. Phys. Soc. Jpn. 84, 023601 (2015).
- [95] R. Nath, A. A. Tsirlin, H. Rosner, and C. Geibel, Phys. Rev. B 78, 064422 (2008).
- [96] H. Rosner, R. R. P. Singh, W. H. Zheng, J. Oitmaa, and W. E. Pickett, Phys. Rev. B 67, 014416 (2003).
- [97] A. Cuccoli, T. Roscilde, R. Vaia, and P. Verrucchi, Phys. Rev. Lett. 90, 167205 (2003).
- [98] A. Cuccoli, T. Roscilde, R. Vaia, and P. Verrucchi, Phys. Rev. B 68, 060402(R) (2003).
- [99] N. Tsyrlin, F. Xiao, A. Schneidewind, P. Link, H. M. Rønnow, J. Gavilano, C. P. Landee, M. M. Turnbull, and M. Kenzelmann, Phys. Rev. B 81, 134409 (2010).
- [100] Y. Kohama, M. Jaime, O. E. Ayala-Valenzuela, R. D. McDonald, E. D. Mun, J. F. Corbey, and J. L. Manson, Phys. Rev. B 84, 184402 (2011).
- [101] T. Förster, F. A. Garcia, T. Gruner, E. E. Kaul, B. Schmidt, C. Geibel, and J. Sichelschmidt, Phys. Rev. B 87, 180401(R) (2013).
- [102] B. D. Piazza, M. Mourigal, N. B. Christensen, G. J. Nilsen, P. Tregenna-Piggott, T. G. Perring, M. Enderle, D. F. McMorrow, D. A. Ivanov, and H. M. Rønnow, Nat. Phys. 11, 62 (2015).

Publication List

- [P1] “One-Third Magnetization Plateau with a Preceding Novel Phase in Volborthite”, H. Ishikawa, M. Yoshida, K. Nawa, M. Jeong, S. Krämer, M. Horvatić, C. Berthier, M. Takigawa, M. Akaki, A. Miyake, M. Tokunaga, K. Kindo, J. Yamaura, Y. Okamoto, and Z. Hiroi, Physical Review Letters 114, 227202 (2015).
- [P2] “A novel crystal polymorph of volborthite, $\text{Cu}_3\text{V}_2\text{O}_7(\text{OH})_2 \cdot 2\text{H}_2\text{O}$ ”, H. Ishikawa, J. Yamaura, Y. Okamoto, H. Yoshida, G. J. Nilsen and Z. Hiroi, Acta Crystallographica Section C: Crystal Structure Communications 68, i41 (2012).
- [P3] “ $\text{Na}_2\text{MoO}_{2-d}\text{F}_{4+d}$ – a perovskite with a unique combination of atomic orderings and octahedral tilts”, H. Ishikawa, I. Munaò, B. E. Bode, Z. Hiroi, and P. Lightfoot, Chemical Communications 51, 15469 (2015).
- [P4] “Kagome-Triangular Lattice Antiferromagnet $\text{NaBa}_2\text{Mn}_3\text{F}_{11}$ ”, H. Ishikawa, T. Okubo, Y. Okamoto and Z. Hiroi, Journal of the Physical Society of Japan 83, 043703 (2014).
- [P5] “Magnetic Properties of the Spin-1/2 Deformed Kagome Antiferromagnet Edwardsite”, H. Ishikawa, Y. Okamoto and Z. Hiroi, Journal of the Physical Society of Japan 82, 063710 (2013).

Acknowledgement

I would like to thank very many people especially in the group and ISSP in finishing the thesis.

I am grateful to Prof. Zenji Hiroi for supervising throughout the thesis work, giving me plenty of freedom of research, chances of collaborating with many groups, and opportunities of presenting research results.

I was supported by very kind and skillful staffs in the group. I thank Prof. Yoshihiko Okamoto for teaching me the solid state chemistry and material exploitation in frustrated magnets. I thank Prof. Junichi Yamaura for teaching me elaborate synthetic techniques and XRD experiments. I thank Dr. Takeshi Yajima for teaching me XRD experiments and the real inorganic chemistry. I thank Dr. Daigorou Hirai for stimulating discussions. I thank Dr. Kazuhiro Nawa for teaching me the essence of quantum spin systems and various experimental techniques. I thank Dr. Gøran Jan Nilsen for showing the very good example of active and international scientist. I thank Dr. Yui Ishii for teaching me experimental techniques.

I am also grateful to the people in MDCL in ISSP. Prof. Yutaka Ueda, Dr. Masahiko Isobe, Dr. Toru Yamauchi, and Prof. Kenya Ohgushi gave us fruitful comments in the group seminar and I could learn a lot about solid state chemistry and physics from their interesting presentations. I thank Dr. Daisuke Hamane for helping electron microscope experiments and gave us deep knowledge of earth science and mineralogy. I thank Dr. Masayoshi Koike for helping the ICP-AES experiments. I thank Dr. Tsuneo Kitazawa and Dr. Rieko Ishii in their help about the facilities of synthetic laboratory.

Quite fortunately, I got chances of collaborating with many professional scientists mainly in ISSP. I appreciate Prof. Masashi Takigawa, Dr. Makoto Yoshida, and Ms. Nanako Nakamura for the NMR experiments and fruitful discussions. I am grateful to Prof. Masashi Tokunaga, Prof. Koichi Kindo, Prof. Shojiro Takeyama, Dr. Atsushi Miyake, Dr. Yoshimitsu Kohama, Dr. Mitsuru Akaki, and Mr. Tomohiro Yamashita for giving us many chances of physical properties measurements in world's best high magnetic field facilities. I am grateful to Prof. Minoru Yamashita and Mr. Daiki Watanabe for their thermal Hall-effect measurements of volborthite. I am grateful to Prof. Hiroshi Kageyama and Dr. Takeshi Yajima for giving me a chance to use their group's PPMS for the heat capacity measurements. I am grateful to Prof. Takatsugu Masuda and Mr. Shohei Hayashida for neutron experiments of $\text{NaBa}_2\text{Mn}_3\text{F}_{11}$. I appreciate Dr. Tsuyoshi Okubo for stimulating discussion about physics of kagome spin systems. I am grateful to Dr. Hiroyuki Yoshida for his kind advices on the hydrothermal synthesis.

I am grateful to Prof. Masashi Takigawa, Prof. Takahisa Arima, Prof. Hirokazu Tsunetsugu, and Prof. Yoshiaki Sugimoto for examining my doctoral qualification and giving me fruitful advices.

I am grateful to Prof. Kazushi Kanoda for his very kind supervision in the MERIT fellowship program.

I am grateful to Prof. Phillip Lightfoot for giving me a precious opportunity of staying in his group in the University of St. Andrews. I thank Dr. Cameron Black and Dr. Irene Munao for supporting my stay in Scotland and teaching me the fun of exploratory synthesis.

I am grateful to Prof. Hidenori Takagi, Prof. Minoru Nohara, and Prof. Simon Clarke for giving me exciting opportunities of making the seminar in their groups.

I am grateful to Ms. Yoshida, Ms. Nakashita, and Ms. Suzuki for helping me various procedures in the laboratory and in research travels. I thank unique group members for supporting my life in laboratory. I enjoyed talking, joining various laboratory events, and collaborating with Mr. Onosaka, Mr. Sato, Mr. Nakazono, Mr. Nagashima, Mr. Hirose, Mr. Ishii, Mr. Matsubayashi, Mr. Okuma, Mr. Tosu, Mr. Tanaka, and Mr. Shimazu. I was stimulated by their presence and helped a lot.

Finally, I am grateful to my family for their warm support.

Hajime Ishikawa